To the University of Wyoming:

The members of the Committee approve the dissertation of Soudeh Kamali presented on July 27, 2021.

Dr. Dimitri J. Mavriplis, Chairperson

Dr. Frederico C. Furtado, Outside Member

Dr. Michael K. Stoellinger

Dr. Ray S. Fertig III

Dr. William K. Anderson, External Examiner

APPROVED:

Dr. Carl Frick, Head, Department of Mechanical Engineering.

Dr. Cameron H. G. Wright, Dean, College of Engineering and Applied Sciences.

Kamali, Soudeh., Development of a High-Fidelity Aero-Thermo-Elastic Analysis and Design Capability , Ph.D., Department of Mechanical Engineering, August, 2021.

The design and optimization of most advanced engineering systems requires multi-disciplinary, high-fidelity simulation in order to accurately capture the physics. For instance, coupled aero-thermo-elastic simulation and sensitivity analysis is required for the precise design and optimization of high-speed vehicles. Since high-fidelity simulations can be computationally costly, methods of design optimization that can minimize this cost are very desirable. Gradient-based optimization using sensitivities obtained through the adjoint method is an efficient approach for systems requiring high-fidelity simulations with large number of design parameters. Therefore, the focus of this research has been on multi-disciplinary analysis and design using the adjoint method. An aero-thermo-elastic analysis and design platform is developed using the in-house flow solver NSU3D and structural solver AStrO. The coupled aero-thermo-elastic analysis capability and adjoint-based sensitivities are validated through multiple applications. In addition, the in-house aero-thermo-elastic simulation capability is applied to design and optimization problems.

DEVELOPMENT OF A HIGH-FIDELITY AERO-THERMO-ELASTIC ANALYSIS AND DESIGN CAPABILITY

By
Soudeh Kamali

A dissertation submitted to the Department of Mechanical Engineering
and the University of Wyoming
in partial fulfillment of the requirements
for the degree of

DOCTOR OF PHILOSOPY
in
MECHANICAL ENGINEERING

Laramie, Wyoming
August 2021

To the spirit of adventure and to those who have supported me in my adventures!

In particular: Maman Alam, Bagher, Manijeh, Somayeh, and Reid.

ACKNOWLEDGEMENTS

My PhD journey has been full of unexpected twists and turns. I had always wondered if ultimately when looking back, I would appreciate this challenging journey. I have met many wonderful people along the way, who have helped me in one way or another. I would like to take this chance to thank them.

My sincere gratitude to my advisor, Professor Dimitri Mavriplis, who gave me a challenging but fascinating project to work on. At first, having no background in mechanical engineering, I found it daunting that I was working on such a physics involved project. However, now I see that this was a great fit for me exactly for that reason. This project created the opportunity to learn so much. Dr. Mavrplis has provided indispensable guidance throughout the numerous difficulties in navigating this research. His devotion to excellence in the pursuit of science has forever shifted my perspective and appreciation of what it means to be a practicing scientist.

This research would not have been possible without the support and advice of my other committee members. I would like to start by thanking Dr. Ray Fertig III for helping me get a better understanding of structural analysis. He always had his door open to me and either had the answer to my problems or provided me with a source to get it from. Next, I would like to thank Dr. Michael Karl Stoellinger for his support, advice and inputs throughout my time at the University of Wyoming (UW). Whenever I had to come to the office over the weekends, it was a great source of motivation to see him also in his office working. Finally, I would like to thank Dr. Frederico Furtado. I have appreciated his optimism, enthusiasm and support. He has always made me think that I am working on something worthwhile and meaningful.

I am very appreciative of the other researchers and students in our group who have helped me tremendously and whom I have learned so many valuable lessons from. In particular Evan Anderson, Zhi Yang, Sung Hwan Yoon, Andrew Kirby, Donya Ramezanian, and Emmett Padway. Each one of them has helped me become a better researcher and has made this experience more memorable.

I was first introduced to CFD by the faculty and staff in the SimCenter at the University of Tennessee at Chattanooga. I will forever remember the friendships I made at the SimCenter, both with faculty and fellow students. The SimCenter was a unique educational environment, and I am glad that I was part of it, even for a short time. First and foremost, I am grateful to the head of the department, Dr. Timothy Swafford, without whom, this journey would never have begun. I still remember the many emails we corresponded when I first applied to the SimCenter. He took a chance on me and I will always be grateful for that. Next, I would like to thank Dr. William Kyle Anderson who was my initial PhD advisor. I wrote my first CFD solver in his class. I don't think he knew how green I was in that first class and how excited I was when I

finally got my first 2-D Euler solver working. I found his patience with his students and dedication to his work inspiring. I am also appreciative of his help and support in transferring to UW. It was through his help along with Dr. Li Wang, and Dr. James Newman II that I found the courage to make this change in my career path. Dr. Anderson has also been on my PhD committee and I have appreciated all his feedback on my work. In a sense he has been with me from the beginning of my PhD studies and I have learned so much from him in the many roles that he has played in my studies.

Working on a PhD project has many highs and lows. You need a support group to get you through it. I have had many wonderful and supportive friends who have helped me through this process. Alma Cemerlic helped me keep my sanity during the final year in Chattanooga. Donya Ramezanian, Esther Pinheiro, and Saeideh Esmailie made my time in Laramie exciting and memorable. I never expected to have so many wonderful adventures in a small town in Wyoming.

Finally, a big thank you to my family back in Iran and here in the US. Their tremendous support, unconditional love, and personal sacrifices throughout the years is the main reason that I was able to complete this work. Special thanks to my father Bagher who nurtured in me a spirit of adventure and a love for education, my mother Manijeh who has always believed in me even when I did not, my sister Somayeh for her encouragement and positive energy, and my partner Reid for loving me even when I was not at my best.

<div align="right">Soudeh Kamali</div>

Laramie, Wyoming
July 2021

TABLE OF CONTENTS

LIST OF FIGURES

xi

LIST OF TABLES

xiv

1 INTRODUCTION

Over the last couple of decades, the aviation industry has grown strongly. This has mostly been due to the broader economic growth, increase in tourism, regulatory reform and greater efficiency in the industry. There has also been an increase in the concern of communities related to the environmental impact of aircraft such as the noise and gas emissions [1]. Researchers around the world are trying to develop technologies that will make air travel more efficient, sustainable and safe. For example, in the report "European Aeronautics: a vision for 2020", the European commission has specified as its main goals a 50% reduction of the noise and CO_2 for the aviation industry [2]. Also, NASA's Aeronautics Research Mission Directorate in 2017 produced a strategic implementation plan to address three major trends: growth in demand for high-speed mobility, affordability, and sustainability in energy use. The plan's vision is to transform aviation in the next 25 years. All these facts show the necessity for rapid development in this area [3].

At the same time, numerical analysis has become an important tool in the development of modern aircraft. The use of computational fluid dynamics (CFD) has become more widespread during the last couple of decades, resulting in significant changes to the aerospace design process. Through the use of supercomputers and advanced numerical methods, various aspects of an aerospace vehicle can now be numerically modeled. Simulation capabilities have reduced the ground-based and in-flight testing requirements and have provided added physical insight, which enables optimized design at lower cost and risk [1, 4, 5].

The use of computational analysis allows engineers to go through a fast evaluation of many design alternatives. Historically, in the aeronautics industry, design optimization has often been done manually. Engineers and designers used their experience and intuition to find a better solution to a problem [6]. Prior to 1960, the primary tool used for aircraft development was the wind tunnel. Various shapes would be tested and modified based on pressure measurements, force measurements, and visualization techniques. However, today computational simulations are widely used in the design of the modern aircraft. This has become possible through a combination of profound improvements in numerical algorithms and rapid developments in the speed and memory of available computers [7].

1.1 Background and Motivation

Most practical engineering problems in the aerospace industry involve interactions between various disciplines. The computational design of such problems must account for the coupling between the different disciplines. This coupling allows for each model to provide complementary information to the other, and therefore, eliminates many assumptions [8]. An important example of this type of problem is fluid-structure interaction. In recent years, the development of supercomputers has made simulation of coupled fluid-structure interactions possible. However, in many engineering designs it is not sufficient to only account for the interaction of the fluid forces and structural deformations; heat transfer also has a significant role in these applications [9, 10].

Flows are often in contact with materials that experience heat transfer. Whenever there is a temperature gradient between a fluid and the solid in contact with it, heat transfer will take place, which will change the flow properties and result in thermal stresses on the solid structure. If this is not accounted for during the design process, it can lead to inaccuracy and even catastrophic failures [11, 12]. Hypersonic vehicles, for example, go through a wide range of flow conditions with large gradients of velocity and temperature close to their surface [13]. One of the major design concerns at these hypersonic velocities is high rates of heat transfer experienced by the vehicle [14]. Therefore, it is essential to account for the effect of temperature in order to obtain accurate numerical designs [11, 12].

In summary, the success of an aircraft design relies on the precise calculation of all the following: Aerodynamic loads (aerodynamic pressure and viscous forces), aero-thermal effects (surface heating rate and inner temperature distributions), and structural loads (structural deformation and stresses) [8, 15, 16]. Since the overall performance of an aeronautical system is governed in many cases by these coupling effects, the study of aero-thermo-elastic analysis and design optimization is of great importance [17].

Generally, when approaching a multi-disciplinary simulation, there are two options available: strong (monolithic) and weak (partitioned) coupling. In the first case, the flow, elasticity and heat transfer equations are treated as one single system of equations and solved at once using a single numerical framework. In the second case, the solution of each discipline is obtained from independent codes and then coupled together by exchanging boundary conditions at the interface between the domains [18, 19]. The strong coupling approach is usually more stable; however, it suffers from the inability to use already available and well-tested solvers. On the other hand, the weak coupling approach is able to use existing, well-developed and tested codes for each discipline. This approach does however have its own disadvantages. These are: the problem of numerical stability and the difficulty of transferring data between the individual disciplinary codes [20, 21].

1.1.1 Aero-Thermo-Elastic Simulations for Hypersonic Flows

Aero-thermo-elastic interaction can be seen in numerous engineering applications. One example of this application in the aerospace industry is the design of hypersonic vehicles. The harsh aero-thermal environment that these vehicles operate in impacts their aero-thermo-structural performance significantly. Multi-disciplinary interactions take place in these vehicles with strong coupling between the flow field, structural heat transfer, and structural response [22]. Hence, the design of reliable and efficient lightweight structures and thermal protection systems for hypersonic vehicles depends on: the accurate prediction of aerodynamic loads, aero-thermal loads, structural temperatures and their gradients, and structural deformations and stresses [15, 22-24].

The cost of experimental research is quite high for hypersonic flight design due to the technical issues associated with hypersonic wind tunnel testing. Routine ground testing is not possible and actual experimental data at high Mach numbers is difficult to obtain. Therefore, numerical simulation plays an important role in the design process [14, 24]. When dealing with these types of problems, in order to have accurate results, interdisciplinary coupling is generally necessary. A separate simulation from the computational fluid dynamics (CFD) code or the computational structural dynamics (CSD) code often cannot provide a good prediction of the heat and load transfer.

During the late 1950's and early 1960's, hypersonic research was very active. This research was instrumental in the design of the X-15 and the space shuttle. Yet, this early research was followed by periods of inactivity due to unattainable technology requirements necessary for the design of these vehicles. Early work on the simulation of fully coupled fluid-structure-thermal interaction problems has been reported by Thornton et al [25-27], where a study of the aero-thermo-elastic interactions of an aerodynamically heated panel was done using the finite-element method. This was followed by the work of Lohner et al [28] in studying nose-cone and deforming panel problems using a coupled platform. For a comprehensive review of aero-elastic and aero-thermo-elastic analysis of hypersonic vehicles refer to the work done by McNamara and Friedmann in reference [29]. Recently, a significant amount of work has appeared focusing on aero-thermal, aero-elastic, and aero-thermo-elastic codes for hypersonic flows [5, 13, 23, 30-34]. However, despite decades of research, this field is far from mature and more study is needed to understand all of the physics involved and to refine high-fidelity aero-thermo-elastic analysis and design.

1.1.2 Multi-Disciplinary Design and Optimization

The central goals of most aerodynamic design are: 1) to produce a shape that is structurally feasible, 2) to have sufficient space for the payload, 3) to achieve a good aerodynamic performance, and 4) to handle the conditions it is exposed to [35]. With that in mind, the design process for a high-speed aeronautical system is still a big challenge today. This is due to the

fact that, to have an accurate design process, we must account for fluid, structure and thermal coupling effects [17]. Hence, a successful aircraft design requires a multi-disciplinary trade-off between many factors such as: aerodynamic efficiency, structural weight, heat dissipation, stability and control, and the volume required to contain fuel and payload. Therefore, an optimum multi-disciplinary design is only reached after cycling between the different disciplines involved [8].

Multi-Disciplinary Optimization (MDO) can be defined as the design method in which the interaction between multiple disciplines is taken into account while producing an optimal solution. Here, the designer is able to change the system performance in more than just one discipline. The interdisciplinary coupling presents additional challenges beyond those encountered in a single-discipline optimization. There is an increase in the computational work as well as complexity of the code which comes from implementing the necessary coupling.

Significant research has been done on the application of MDO to aircraft design. The survey paper by Sobieszczanski-Sobieski and Haftka [36] provides a great overview of the work done in this area. Some of the earliest efforts in MDO can be seen in the works of Schmit [37] and Haftka [38-41]. Most of this work extended from their experience in structural optimization to include other disciplines. Later, in 1988 Grossman et al. [6] performed an investigation using a combination of lifting-line aerodynamics with finite-element beam models in aero-structural optimization. Though they used low-fidelity methods, their work did demonstrate the advantage of multi-disciplinary optimization in comparison to examining each discipline individually [42]. Even though in the beginning most MDO studies used low-fidelity models, as computing platforms become faster, the use of high-fidelity models for analysis and optimization has become more common. This was seen in the work of Giunta [4] and Maute et al. [10], where aero-structural sensitivities are calculated using high-fidelity models.

The current trends in aerodynamic design require high-fidelity multi-disciplinary optimization. Today, we can see the availability of multiple codes that can run multi-disciplinary design cases. Martins et al. performed aero-structural design optimization [43, 44]. Mani et al. [45, 46], Mavriplis et al. [47, 48], and Zhang et al. [49] presented results from aero-structural code for unsteady design/optimization. Fabiano et al. [20] show results for a loosely coupled aero-acoustic solver with design capabilities. Anderson et al. [42, 50] and Kamali et al. [30], developed a loosely coupled thermo-elastic, and aero-thermo-elastic analysis and optimization tool [51].

There are two main techniques for solving numerical design optimization problems: gradient-based methods and global search methods [6]. Gradient-based optimization methods are more popular within the field of aerodynamics. This is because of the lower number of analysis runs or function evaluations required for these methods in comparison to global search techniques [48]. Among gradient-based optimization methods, the adjoint approach has the advantage of computing cost function gradients at a cost independent of the number of design

variables [52]. This characteristic makes the adjoint method appealing for large, high-fidelity multi-disciplinary design problems, and that is the motivation for the current work.

1.2 Objectives

The objective of this work is to develop and validate a coupled aero-thermo-elastic analysis and design capability which:

- Uses high-fidelity models for each discipline.
- Uses a weak coupling approach to couple the fluid and structural solvers in order to take advantage of the already available and well tested in-house solvers.
- Performs transient three-dimensional analysis.
- Performs tangent and adjoint sensitivity analysis for optimization purposes.

In order to achieve the above objectives, the project was divided in two parts: the analysis part and the optimization part. The steps required for the completion of each part are as follows:

1) Analysis
    - Further develop the implementation and validation of the in-house thermal analysis capability.
    - Further develop the implementation and validation of the in-house thermo-elastic analysis capability.
    - Develop and validate the aero-thermo-elastic analysis capability using in-house solvers.

2) Design Optimization
    - Further develop the implementation and validation of the thermo-elastic sensitivities.
    - Demonstrate standalone static and transient thermo-elastic optimization.
    - Develop and validate the aero-thermo-elastic tangent and adjoint sensitivities.
    - Demonstrate aero-thermo-elastic optimization.

1.3 Dissertation Outline

The outline of this dissertation is summarized as follows:

Chapter 2 – Coupled Aero-Thermo-Elastic Analysis: A brief overview of coupled multi-disciplinary analysis is given. This is followed by a description of the aero-thermo-elastic analysis implementation developed in this dissertation.

Chapter 3 - Analysis Results: First the thermal and thermo-elastic analysis capabilities of the structural solver are validated. Next, results are presented for the aero-thermo-elastic analysis capability developed in this work.

Chapter 4 - Coupled Aero-Thermo-Elastic Design Optimization: A brief overview of multi-disciplinary sensitivity analysis and optimization is given. This is followed by the description of the coupled thermo-elastic and aero-thermo-elastic sensitivity analysis formulation implemented and used.

Chapter 5 - Sensitivity Analysis and Optimization Results: Validation of the adjoint sensitivities for the thermo-elastic and aero-thermo-elastic sensitivity analysis is provided. This is followed by results from thermo-elastic and aero-thermo-elastic optimization examples using the validated adjoint sensitivities.

Chapter 6 - Conclusions and Future work: Conclusions of the work are drawn, and future directions are outlined.

2 COUPLED AERO-THERMO-ELASTIC ANALYSIS

In this chapter, we first look at some of the main challenges in aero-thermo-elastic analysis and best practices to deal with them. Then we move on to describing the aero-thermo-elastic analysis capability developed in this work.

2.1 Aero-Thermo-Elastic Coupling Challenges

A fundamental issue in multi-physics analysis is how to integrate the different physics together. For aero-thermo-elastic analysis, the problem can be thought of as having two spatial domains and three physical disciplines. The two domains are: the fluid and solid domains. The three disciplines are: the fluid, thermal, and structural dynamics. When coupling different physics together, there are two options available: strong (monolithic) and weak (partitioned) coupling. In the first case, the different disciplines are treated as one single system of equations and solved at once. In the second case, the solutions for each discipline are obtained from independent codes and then coupled together.

One of the disadvantages of strong coupling is that the matrix for the full system may end up being ill conditioned. For example, in the case of the aero-thermo-elastic coupling this happens due to the fluid and solid having different stiffness characteristics and they usually require different discretizations. Another major disadvantage of the strong coupling method is that it requires the re-writing of the code for each of the disciplines in order to account for the coupling. Furthermore, for large problems, strong coupling can become overly complex to maintain. On the other hand, weak coupling allows the reuse of existing and well validated fluid and structural solvers, introducing only small changes. Here, it is only required to transfer information at the interfaces of the disciplines, leading to non-invasive coupling. This allows us to use the best solution strategy for each discipline. Because of these advantages, this approach is suitable for larger and more complex problems. However, weak coupling does have its own disadvantages too, one is the problem of numerical stability and the other is the difficulty of transferring information between the two codes [21]. Although, even with these problems, weak coupling is very attractive due to significant computational saving and implementation simplicity [53, 54].

Disciplinary code-coupling can be very challenging in practice because of three main differences between fluid and solid models, which is due to the large differences between the two media.

- Time-scale difference - The time scales of flow and solid are generally very different.

- Space-scale difference – Commonly the surface meshes are mis-matching and different discretization methods are used on the fluid and the structure side.

- CPU difference - The discrepancy between the memory requirements and execution time between the fluid and solid solver.

Specific coupling treatments are needed to handle these differences [12, 55]. The above mentioned challenges that arise from the difference between the disciplines are seen in both strong coupling as well as weak coupling of aero-thermo-elastic platforms.

Another one of the most important issues in the fluid-structure Interaction (FSI) problems is the stability property. The stability limitations are important because instability could end up showing itself only after a large amount of computational time has passed. Knowing this in advance would save a lot of time and effort [56]. There are many options available for the interface interaction between a solid and a fluid domain. Each option has a different effect on the convergence and stability of the system. The challenge of dealing with the interface and its effect on stability is more prominent in the weak coupling approach. In the following, each of the challenges mentioned above will be looked at in more details.

2.1.1 Difference in Time-Scale

The physical time scale of the fluid and the solid is very different. Hence, one of the most fundamental challenges in computational modeling of aero-thermo-elastic problems is the difference in the time scales between the fluid, thermal and structural disciplines. For example, in a gas turbine a blade submitted to the flow from a combustion chamber has a thermal characteristic time scale in the orders of a few seconds while the flow characteristic time scale is less than $1ms$. Due to this difference in time scale, the frequency of data exchange between the codes is very important for precision and stability reasons. This also indicates that the solid domain controls the convergence of the aero-thermo-elastic problem [57]. The fluid and structural physics operate at significantly smaller time scales than the thermal evolution.

The weak coupling method has the advantage of allowing flexibility in the usage of the time integration scheme and time step-size for each physics solver. Each physics model can have a time step smaller than the coupling time step, but the data transfer only happens at the coupling time step. This increases the global computational efficiency and the convergence property of the coupled system. It allows us to use the optimal time step size for each individual physics model without the need to use the smallest one for all the physical domains, which is the case in the strong coupling method [58]. This is illustrated in Figure 2-1.

Since the characteristic time scale of the fluid solver is much smaller than the solid solver, if we were to perform a solid calculation each time the fluid solver went through a time step, it would be a waste of CPU time since the changes in the solid happens at much larger time steps

[59, 60]. Hence, the transient may be negligible on the fluid side. This can be used to avoid time integration and reduce computational expense of the fluid solver using a steady-state flow assumption. This means an instantaneous boundary conditions from the other solvers is used to compute fluid loads with a time history of the flow [53]. Much previous work has assumed a static fluid problem, a quasi-static structural problem, and a transient thermal problem in order to solve this time-scale discontinuity and also to save on computational expenses [16, 53].
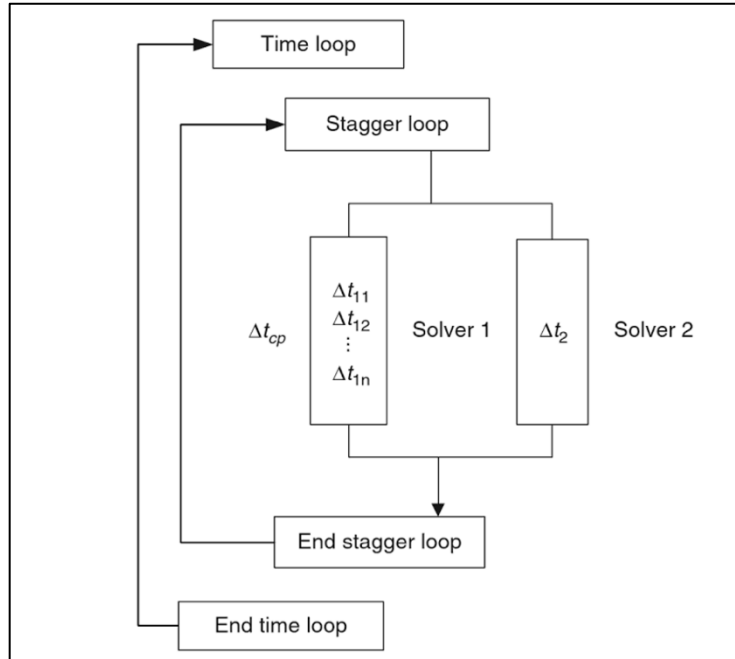
Figure 2-1: Sub-cycling algorithm [58]

2.1.2   Difference in Space-Scale

The discontinuity in the space-scale also represents another challenge in aero-thermo-elastic simulations. Commonly the finite-element model is used in the solid subdomain whereas the finite-volume method is adopted in the fluid subdomain. In addition, in most of these simulations the surface meshes at the interface are non-matching [19]. This is needed for capturing the physics accurately at a reasonable cost on both the fluid and the solid domains [61]. For example, the flow solver usually requires a finer mesh at the boundaries in order to solve for the large velocity gradients present and to be able to capture shock waves and boundary layers. On the other hand, the structure solver requires a finer grid distribution near areas of high curvature [62, 63], but in general employs a coarser grid distribution. The use of different types of elements used by different solvers can also cause mesh mis-match at the interface [18]. An example of fluid and structure meshes with a non-matching interface can be seen in Figure 2-2.

9

During the data transfer, the solution is interpolated from the fluid mesh to the structure mesh and then later from the structure mesh to the fluid mesh. In such applications the data transfer needs to be as numerically accurate and as physically conservative as possible. When dealing with applications that involve repeated data transfer, achieving both accuracy and conservation is important because errors accumulate over iterations [19]. This will be discussed in more details later in this chapter.
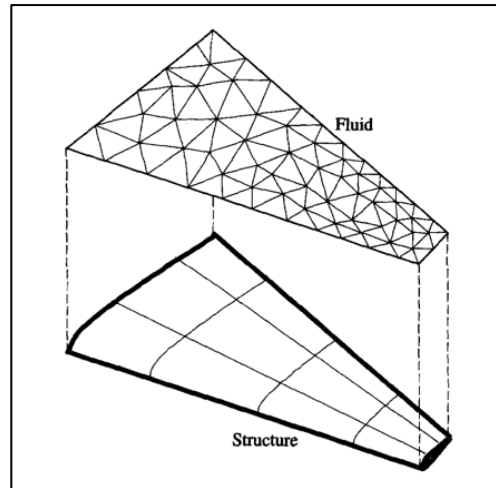
Figure 2-2 Fluid and structure meshes with non-matching interface [64].

2.1.3 Difference in CPU Requirements

There are two options available when running a coupled problem on a parallel machine. The first option is called the Sequential Coupling Strategy (SCS) or the Gauss-Seidel iteration method. In this case the codes run sequentially, and each solver uses all the available processors. In this mode each physics solver always gets the most recent interface loads from the other physics models. The second option is the Parallel Machine Strategy (PCS) or the Jacobi iteration method. In the PCS mode both solvers run together using information from the previous Jacobi iteration. In this case the two solvers must share the number of available processors [57, 58]. These two options are illustrated in Figure 2-3. Based on the literature the Gauss-Seidel iteration method or the SCS method normally has better convergence behavior than the PCS or Jacobi iteration [57, 58]. One thing to be noted here is that in the Gauss-Seidel iteration method, the simulation order can affect the convergence behavior. It is good practice to choose the solution-driven physics model and the one with a good initial guess as the starting physics [58].
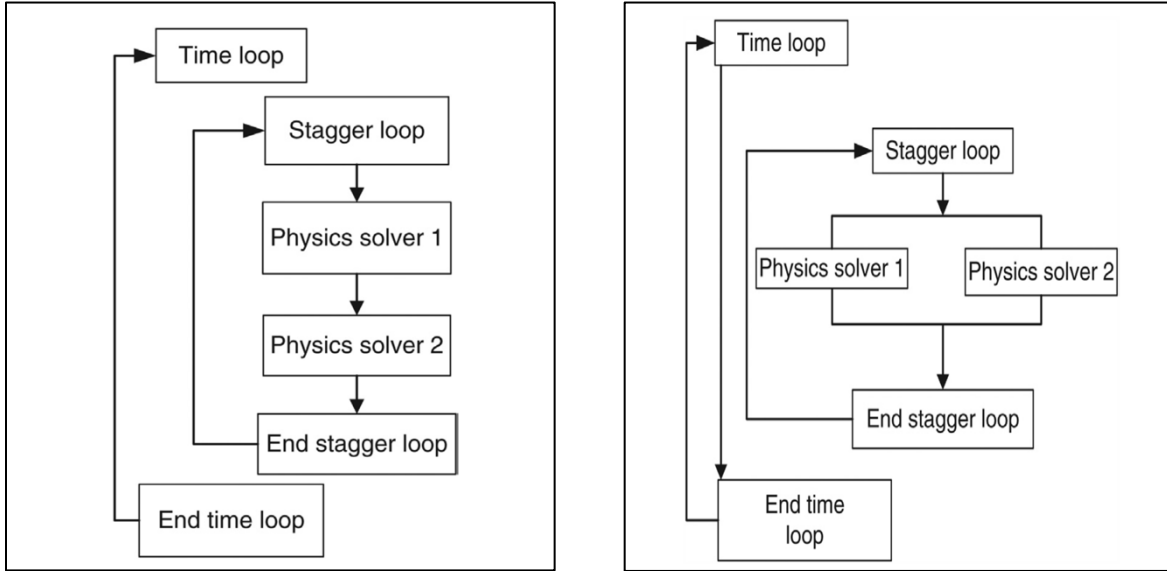
Figure 2-3: Gauss-Seidel iteration (left) and Jacobi iteration (Right) [58].

2.1.4   Dealing with the Interface for the Weak Coupling Approach

When talking about the interface, we are referring to an arbitrary surface, which separates the fluid and solid domains. As mentioned previously, usually there are different discretization methods used in the solid and fluid domain. Generally, multi-physics simulations require an accurate and conservative scheme to transfer the physical data across non-matching discrete meshes. By choosing the correct interface condition, most of the problems in the fluid-solid coupling can be avoided [12]. Below we look more closely at how the choice in the data transfer and boundary conditions effects the stability in FSI problems.

2.1.4.1   *Boundary Condition at the Interface*

For aero-thermo-elastic coupling, the weak coupling method uses an iterative approach to converge to the same temperature and heat flux at the boundaries of the fluid and solid domain. Likewise, it checks to see if the values for the aerodynamic loads on the fluid side and the displacements generated by the structure solver in response to these aerodynamic loads have converged.

It is clear that for the structural boundary conditions, the aerodynamic loads need to be transferred from the fluid mesh to the structure mesh, and the structural deformations from the structure mesh to the fluid mesh. However, the exchange of the thermal boundary conditions can be done in one of two ways. The first method imposes the wall temperature distribution on the fluid side and the heat flux distribution on the solid side. This loop is repeated until convergence is reached, which is when the temperature and heat flux become continuous

11

between the two domains. In the literature this method is known as the flux forward temperature back (FFTB) method or the Dirichlet-Neumann boundary condition [62, 63]. Another available method is to impose the heat flux to the fluid and the resulting wall temperature to the solid domain. This method was successfully used by Heidmann et al [65] and is called the temperature forward flux back (TFFB) method or the Neumann-Dirichlet boundary condition. The advantage of this method is that the temperature is given to the solid model, which is a more natural boundary condition for that domain. However, this method is not very robust and shows stability problems as proven by Giles [62, 63, 66]. Figure 2-4 shows the transfer of data at the boundary for the FSI problem for the FFTB method proven to be the most robust and stable method for thermal boundary conditions used in aero-thermal problems.

Giles [66] studied the stability for the aero-thermal or conjugate heat transfer boundary condition in 1-D, where Finite-difference (FD) was used to discretize both domains. He was able to show that to achieve numerical stability we need to transfer the temperature to the fluid domain (Dirichlet condition) and the heat flux to the solid domain (Neumann condition). The stability analysis was conducted using the Godunov and Ryabenkii method [55, 56, 67]. However, FSI problems typically are not based on FD discretizations. They usually use finite-volume/Finite-element (FV/FE) methods for the fluid and structure domains, respectively. It was Roux and Garaud [68], who studied the behavior of interface conditions in a steady fluid-solid thermal coupling, in a more general fashion than Giles. They first proved that in general a Dirichlet condition must be imposed on the domain with lower conductivity, which is the fluid domain. They also showed this to be true for the case of using finite-volume/finite-element discretization.
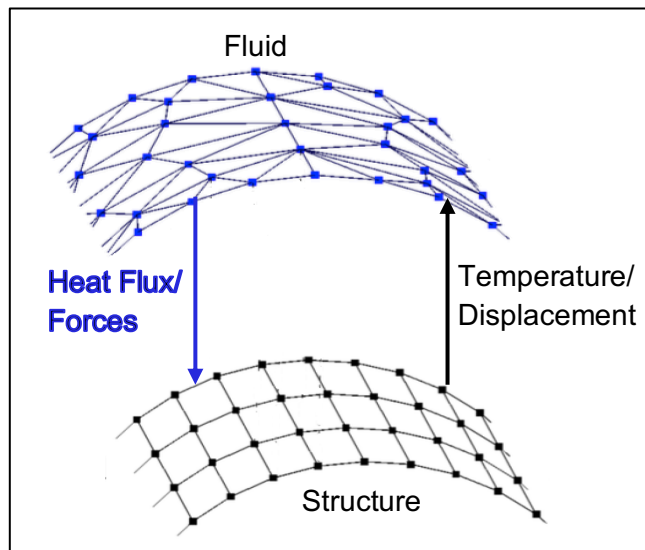
Figure 2-4: Fluid-Structure Interface Boundary Conditions.

2.1.4.2 *Data Transfer at the Interface*

The interfacing methods used to solve FSI problems can be categorized as non-conservative or conservative schemes. As the name suggests in the case of the non-conservative schemes, for example, the work done by the fluid traction transferred to the solid, or the heat flux transferred from the fluid to the structure is not conserved. In such cases in order to have reasonable results we require finer meshes for both the fluid and the solid domains [69]. Many non-conservative interpolation-based schemes have been used often for FSI applications for simplicity. However, conservative schemes are found to be crucial for the repeated data transfer of large spatial gradients (e.g., shocks) and the stability of the weakly coupled solvers [61, 70]. It can be concluded that high-fidelity coupled fluid-structure simulations require accurate and conservative data transfer of boundary conditions [61].

Conservative load transfer schemes which are generally used for non-matching interfaces can be put in two categories: node-projection and common-refinement schemes [70]. In the following pages we will look more closely at each of these schemes.

2.1.4.2.1 The Node-Projection Scheme

The main idea in this scheme is that for a given point on the fluid mesh, a host element on the structure gird is identified, and then the fluid node is projected onto the structure mesh and finally the solution is interpolated [21]. The steps can be summarized as follows:

1) Find the nearest element on the structure mesh and project the surface fluid mesh point on to this element.
2) Interpolate/inject the solution from the fluid point to its projection on the structure mesh.
3) Transfer the load coming from the fluid side to the structure element using the shape functions in the structure element.

The first step is the most time consuming part, which requires a proximity search, in which we find the closest point on the structure mesh surface elements from the fluid point. This is done using a normal projection of the fluid point onto the closest exposed structural element surface face [71].

Hence, the load vector r_{sj} on the structure surface node j becomes [18, 69, 70]:

$$r_{sj} = \sum_{i=1}^{m_f} N_s^j(x^i) r_{fi} \tag{2-1}$$

where x^i denotes the location of node i of the fluid interface mesh, m_f is the number of surface fluid nodes, N_s^j is the solid element shape functions, and r_{fi} is the load vector on the fluid surface nod i.

Although the Node-projection scheme is conservative, it often lacks accuracy in transferring loads across non-matching meshes. This scheme generally creates local errors for non-matching

meshes. In addition, the error in this scheme does not disappear with the refinement of the meshes, which can result in non-convergence while performing grid refinement [18, 69, 70].

2.1.4.2.2 The Common-Refinement Scheme

A common-refinement overlay mesh is a surface mesh composed of elements that partition the elements of both the fluid and solid meshes at the same time. In simpler terms, it is the intersections of the elements of the two domains [19, 61]. This intersection creates sub-elements as shown in Figure 2-5 for the $3D$ case.
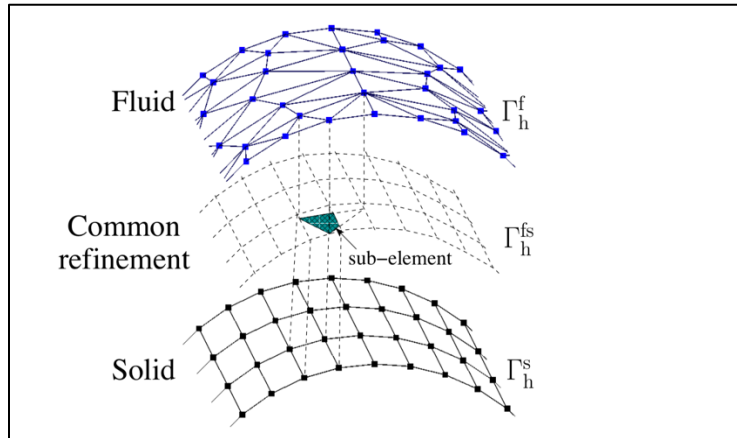
Figure 2-5: Schematic of common-refinement based projection scheme for load transfer in $3D$; where shaded area denotes one surface sub-element [61].

This method was first proposed by Jiao et al. [72], to resolve the accuracy problem of the previous conservative data transfer schemes. It allows for an accurate integration of a function that depends on the shape functions of two meshes with different resolutions. The common-refinement overlay mesh is created in such a way that both the source and target functions are continuous in each of the sub-elements. This scheme is important for stable, accurate and conservative FSI computations. Despite its benefits, the common-refinement method has been avoided by many scientists and engineers. The reason for this is its complexity in three-dimensional implementation and in parallelizing the algorithm [19, 61]. A detailed algorithm for this method is described in Reference [72] and the description of a detailed implementation of this method in $3D$ is given in reference [61].

2.2 Aero-Thermo-Elastic Analysis Capability Implementation

In this work it was decided to couple the disciplines through a weak coupling approach. This decision was made because it allows us to take advantage of the already available and tested high-fidelity flow solver and structural solver developed in-house for multi-disciplinary modeling. In the rest of this section, we look at the different components of the numerical set

up used in this work to run an aero-thermo-elastic analysis simulation: the flow solver, the structural solver (elasticity and thermal equation), fluid-structure interaction (FSI) module, and the mesh deformation capability.

2.2.1 Flow Solver

The flow solver used in this study is the "Navier-Stokes Unstructured 3D" (NSU3D) code, which is a Reynolds-averaged Navier-Stokes (RANS) solver for unstructured grids [73]. It is a vertex-centered finite-volume solver, which is second-order accurate in both time and space. This flow solver uses a line-implicit agglomeration multigrid algorithm, which can be used either as a non-linear solver, or a linear solver within an approximate Newton method, or as a pre-conditioner for GMRES for driving the non-linear steady-state residual to zero [74]. For time-dependent problems, all the above-mentioned solvers can be used in a dual-time stepping approach for solving the non-linear problem, which arises at each time step [47]. NSU3D has been widely validated for both steady-state and time-dependent flow problems, having been used in numerous simulations and participations in events such as the Drag Prediction Workshop, the High-Lift Prediction Workshop, and the Aero-Elastic Prediction Workshop series [75-78]. In recent years, NSU3D has been extended for use in coupled aero-elastic calculations [47, 48, 50]. In this work we describe the extension of this code to coupled aero-thermal and aero-thermo-elastic calculations [5, 30]. Detailed explanation of this solver can be found in previously available references [73, 79, 80]. As such, only a concise description of the formulations will be given here.

The flow solver is based on the conservative form of the Navier-Stokes equations. These may be written as:

$$\frac{\partial u(x,t)}{\partial t} + \nabla . F(u) = 0 \qquad (2\text{-}2)$$

For moving mesh problems, the above formulation is written in arbitrary Lagrangian-Eulerian (ALE) form, as:

$$\frac{\partial Vu}{\partial t} + \int_{B(t)}[F(u) - \dot{x}u].ndB = 0 \qquad (2\text{-}3)$$

where V refers to the volume of the control volume bounded by a control surface $B(t)$, $\dot{x}$ is the vector of mesh face or edge velocities, and n is the unit normal of the face or edge. Vector u denotes the state vector of conserved variables, and the flux vector F contains both inviscid and viscous fluxes. The equations are closed with the perfect gas equation of state for cases presented in this work [48, 79].

The time derivative term is discretized using a second-order accurate backward difference formula (BDF2) scheme, leading to the implicit system of equations at each time step given as:

15

$$\frac{3}{2\Delta t}V^n u^n - \frac{2}{\Delta t}V^{n-1}u^{n-1} + \frac{1}{2\Delta t}V^{n-2}u^{n-2} + S^n(u^n, x^n, \dot{x}^n) = 0 \qquad (2\text{-}4)$$

where $V^n = V(x^n)$ represents the mesh control volumes and $S^n(u^n, x^n, \dot{x}^n)$ represents the spatial discretization terms at the nth time step.

The functional dependence of the implicit system to be solved at each time step can be written in residual form as:

$$R^n(u^n, u^{n-1}, u^{n-2}, x^n, x^{n-1}, x^{n-2}) = 0, \qquad n = ,2,3,\dots,N \qquad (2\text{-}5)$$

where the initial conditions are given by u^0 and x^0, and noting that a BDF1 time discretization is used for the first time step. At each time step, the implicit residual is solved using a line-implicit solver with agglomeration multigrid. Although, in this work the flow solver solves a steady-state problem at each coupling time step. Therefore, the steady-state form of Eq.(2-5) is solved on the fluid side, which is shown in Eq.(2-6) below:

$$R^n(u^n, x^n) = 0 \qquad (2\text{-}6)$$

It should also be mentioned that for the cases presented in this work the fluxes are calculated using the Roe scheme [81]. It should also be mentioned that the flow medium is considered as perfect gas in NSU3D.

Considerable effort has been spent in previous work for implementing and verifying the discrete adjoint approach for computing fluid sensitivities within the NSU3D unstructured mesh RANS CFD solver. Exact sensitivities can be calculated for both steady-state and time-dependent problems in the NSU3D framework using the adjoint and tangent methods [45, 47, 80].

2.2.2 Structural Solver

The structural solver used in this study is a finite-element solver named AStrO (Adjoint-based Structural Optimizer), which was developed in-house. AStrO has been introduced in previous work [5, 30, 42, 47, 48, 50] and supports both linear and nonlinear finite-element modeling of three-dimensional structures [50]. AStrO also supports finite-element modeling of the thermo-elastic behavior of structures. AStrO can run static or dynamic analysis of either the heat transfer problem, or the elasticity problem, or the two coupled disciplines [42]. The motivation for constructing an in-house structural solver to enable tight coupling as well as for calculating sensitivities for coupled CFD and computational thermal and structural dynamics (CTSD) problems using the adjoint method [48] .

AStrO is compatible with existing commercial structural analysis software tools such as Abaqus [82]. It contains an interface that can process model input files generated by Abaqus [47]. Dynamic systems are modeled with implicit second-order accurate time integration by the

Hilber-Hughes-Taylor "alpha" method [83]. The discretized equations for the elasticity problem are derived from the widely used virtual work formulation [83]. The temperature distribution due to heat conduction through a structure is governed by the Poisson equation, which is discretized in a similar manner as the equations of elasticity. In the following paragraphs we take a closer look at AStrO's governing equations.

The transient elasticity equation solved in AStrO is given as:

$$\nabla \cdot \sigma - \xi \frac{du}{dt} - \rho \frac{d^2u}{dt^2} + f = 0 \tag{2-7}$$

where f represents the applied body forces, u is the vector of displacements, σ is the stress tensor, and ξ is the damping coefficient.

The principle of virtual work [84] applied to the equations of elasticity for a deformable elastic body subject to applied body forces and surface tractions, as well as damping forces proportional to velocity, can be expressed mathematically as:

$$\int_\Omega (\sigma \cdot \delta\epsilon)d\Omega + \int_\Omega \xi(\dot{u} \cdot \delta u)d\Omega + \int_\Omega \rho(\ddot{u} \cdot \delta u)d\Omega - \int_\Omega (f \cdot \delta u)d\Omega - \int_S (t \cdot \delta u)dS = 0 \tag{2-8}$$

In the above $u, \dot{u}, \ddot{u}$ are the vector displacement, velocity, and acceleration at a point in a structure, σ and ϵ are the stress and strain in second-order tensor form, ξ is the damping coefficient, ρ is the mass density, f is the applied body force per unit volume, t is the applied surface traction per unit area on the structure. The final term is the integral of traction over the surface area of the structure, while all other terms are volume integrals over the body of the structure. The δ operator indicates a variation on the function to its right, meaning the above must hold for any variation of the displacement field u [42, 50]. The virtual displacement, δu, is a function of space throughout the body, and $\delta\epsilon$ is the variation of strain corresponding to that virtual displacement.

The equation of motion for dynamic elastic bodies derived from the principle of virtual work discretized using the finite-element method is:

$$\int_\Omega \sigma_i \frac{\partial \epsilon_i}{\partial U_j}d\Omega + \int_\Omega \xi\dot{u}_i N_{ij}d\Omega + \int_\Omega \rho\ddot{u}_i N_{ij}d\Omega - \int_\Omega f_i N_{ij}d\Omega - \int_S t_i N_{ij}dS = 0 \tag{2-9}$$

where N_{ij} is a matrix of basis functions and U_j is a vector of nodal solution parameters, or degrees of freedom. The matrix equivalent of Eq. (2-9) is then obtained as shown in Eq. (2-10):

$$[K]U + [C]\dot{U} + [M]\ddot{U} = F \tag{2-10}$$

where $[K]$ is the stiffness matrix, $[M]$ is the mass matrix, $[C]$ is the viscous damping matrix, F is the vector of forces, U is the vector of nodal values displacements, $\dot{U}$ vector of nodal values of velocities, and $\ddot{U}$ vector of nodal values of acceleration.

The transient heat equation solved in AStrO is given as:

$$\rho c \frac{\partial T}{\partial t} + \nabla \cdot (k \nabla T) - Q = 0 \tag{2-11}$$

where, Q is the rate of internal heat generation per unit volume, k is the thermal conductivity, c is the specific heat capacity, ρ the density, and T is the temperature.

The variational form for temperature distribution due to heat conduction in a structure can be developed in a similar fashion as the equations of elasticity:

$$-\int_{\Omega} \left(q \cdot \delta(\nabla T) \right) d\Omega + \int_{\Omega} \rho C_p \dot{T} \delta T d\Omega - \int_{\Omega} Q \delta T d\Omega + \int_{S} (q \cdot n) \delta T dS = 0 \tag{2-12}$$

The discretized governing equations for heat conduction in structures derived from the variational form using the finite-element method is:

$$-\int_{\Omega} q_i \frac{\partial N_j}{\partial x_i} d\Omega + \int_{\Omega} \rho C_p \dot{T} N_j d\Omega - \int_{\Omega} Q N_j d\Omega + \int_{S} q_i n_i N_j dS = 0 \tag{2-13}$$

where n_i is the normal vector, q_i is the surface heat flux, and N_j the basis function. The matrix equivalent is then obtained as shown in Eq. (2-14):

$$[K_{therm}] T + [M_{therm}] \dot{T} = F_{therm} \tag{2-14}$$

where the vector T is the nodal values of temperature, $[K_{therm}]$ is the global thermal conductivity matrix, $[M_{therm}]$ is the thermal mass matrix, and F_{therm} is the vector of internal heat generation sources.

AStrO is capable of modeling the coupled thermo-elastic responses in structures. However, there are several simplifying assumptions made. The first assumption is that thermal material properties such as conductivity and specific heat capacity have no significant dependence on strain. Furthermore, the heat generated by deformation is assumed to be negligible. In other words, the deformation has a one-way dependence on the temperature distribution. These assumptions are acceptable, since the cases to be considered are expected to have small values of strain and within the elastic regime, selected materials will have low internal damping characteristics, and deformation rates will not produce significant heat through phenomena such as viscoelasticity [42].

Under these assumptions, in any given analysis, the temperature distribution of a structure can be obtained first, followed by the deformation solution based on the temperature results in addition to applied loads. To account for the dependence of deformation on the temperature distribution, an adjustment to the definition of total strain is required. Any point in the structure that is subject to a combination of applied stress and change in temperature will exhibit a measure of strain for each of those contributors. Hence, the total strain can be expressed as:

$$\epsilon_{kl}^{total} = \epsilon_{kl}^{stress} + \epsilon_{kl}^{therm} \tag{2-15}$$

In the governing equations of elasticity based on the principle of virtual work, stress at a point under the assumption of linear elasticity can be expressed as:

$$\sigma_{ij} = C_{ijkl}\epsilon_{kl} \tag{2-16}$$

where C_{ijkl} is the stiffness matrix of the local material. However, ϵ_{kl} in Eq. (2-16) must only be the strain due to the applied stress. Therefore, in the presence of thermal expansions, we have:

$$\sigma_{ij} = C_{ijkl}\epsilon_{kl}^{stress} = C_{ijkl}\left(\epsilon_{kl}^{total} - \epsilon_{kl}^{therm}\right) \tag{2-17}$$

Fundamentals of continuum equilibrium mandate that the stress and strain matrices be symmetric, so that $\sigma_{ij} = \sigma_{ji}$ and $\epsilon_{kl} = \epsilon_{lk}$. Hence, they can be expressed more concisely as one-dimensional vectors, adopting a single subscript index for normal stresses and strains. Both the second order tensor and first order vector forms express the same linear elastic relationship between stress and strain. However, for the former a given component of the stiffness matrix is denoted with four subscript indices corresponding to the second order indices for stress and strain. For the latter, the stiffness matrix is denoted with two subscript indices. By re-writing Eq. (2-17) above in terms of strain in one-dimensional vector form, we arrive at:

$$C_{ik}\left(\frac{\partial \epsilon_k^{total}}{\partial x_j} - \alpha\frac{\partial T}{\partial x_j}\right) = 0 \tag{2-18}$$

The strain due to thermal expansion is assumed to be linearly related to temperature, such that the change in temperature from some reference temperature T^{ref} multiplied by a vector of thermal expansion coefficients α gives the resulting thermal strain to be:

$$\epsilon_k^{therm} = (T - T^{ref})\alpha_k = \Delta T\alpha_k \tag{2-19}$$

If the stress in Eq. (2-9) is expressed using Eq. (2-18) and Eq. (2-19), then the governing equations for the elastic response taking into account the change in temperature, becomes:

$$\int_\Omega C_{ik}\big(\epsilon_k^{total} - \Delta T \alpha_k\big)\frac{\partial \epsilon_i}{\partial U_j}d\Omega + \int_\Omega \xi \dot{u}_i\, N_{ij}d\Omega$$

$$+ \int_\Omega \rho \ddot{u}_i N_{ij}d\Omega - \int_\Omega f_i N_{ij}d\Omega - \int_S t_i N_{ij}dS = 0 \quad (2\text{-}20)$$

Separating out the contribution of the thermal expansion from the stress term gives:

$$\int_\Omega C_{ik}\epsilon_k^{total}\frac{\partial \epsilon_i}{\partial U_j}d\Omega + \int_\Omega \xi \dot{u}_i\, N_{ij}d\Omega + \int_\Omega \rho \ddot{u}_i N_{ij}d\Omega$$

$$- \int_\Omega f_i N_{ij}d\Omega - \int_S t_i N_{ij}dS - \int_\Omega C_{ik}\Delta T \alpha_k \frac{\partial \epsilon_i}{\partial U_j}d\Omega = 0 \quad (2\text{-}21)$$

Since the temperature solution is pre-computed, the effect of thermal expansion shows up as part of the load in the elasticity equations (or the final three terms in Eq. (2-21) above). Equation (2-21) is the augmented form of the governing equations for thermoelastic modeling. AStrO's thermal and thermo-elastic analysis capabilities have been validated in references [42] and [5].

AStrO has the capability of calculating exact sensitivities using the adjoint method [50]. AStrO also offers an on-board optimizer using the steepest-descent line search algorithm with backtracking [85]. This function is convenient for simple problems and for trouble shooting, since it does not require linking with external packages. This optimizer was used for all the thermo-elastic optimization results presented in this work. Alternatively, more sophisticated optimizers can be linked to AStrO for more complex optimization problems [42].

2.2.3 Fluid-Structure Interaction (FSI)

Proper data transfer between different disciplines is one of the most important factors in multi-disciplinary analysis and design. Correct modeling of aero-thermo-elastic problems requires an accurate coupling of the fluid and structure codes. Although in these problems the geometry is shared, the models most often have dissimilar meshes. Moreover, boundary data from one domain must be available on the other domain [71]. The weak coupling method uses an iterative approach to converge the temperature and heat flux distributions at the boundaries of the fluid and structure domains. The computation alternates between the fluid and structure domains with exchange of the above-mentioned boundary conditions [62, 63]. In weak coupled codes, the CFD and CTSD codes are alternatively called from a master program. This master program is also in charge of transferring data between the codes on the CFD/CTSD interface.

In order to control the stability and convergence in these problems, the choice of the boundary condition is very important. In the literature, the continuity of temperature and heat flux at the interface is mainly implemented by imposing the wall temperature distribution

computed from the CTSD solution on the fluid side and the heat flux distribution computed from the CFD solution on the structure side. This method is known as the flux forward temperature back (FFTB) method or the Dirichlet-Neumann boundary condition. As explained previously, many researchers have shown that the use of this type of boundary condition is the key to achieving numerical stability and having robust convergence [62, 63, 66, 86].

An FSI module had previously been created in-house and used for aero-elastic analysis and design problems [47, 48]. This model has been used to transfer the aerodynamic forces from the fluid solver to the structure solver, and in return pass the calculated displacements to the fluid surface mesh [47]. In this work, this module which uses a node-projection method was updated so that it can also transfer temperature and heat flux between the fluid and structure meshes. When dealing with the aero-thermo-elastic analysis, we need to exchange the aerodynamic forces and heat fluxes from the fluid domain to the structure domain, and in return send the temperatures and displacements from the structure mesh to the fluid mesh. The effects of the temperature on the structure are dealt with internally in the structure code as explained in the previous section.

In practice the FSI computes the heat fluxes and the aerodynamic forces at each CFD surface mesh point. These values are then projected onto the finite-element basis functions where they are assembled in the form of heat fluxes and forces on the finite-element nodal locations. Conversely, once the structural temperature and displacement solutions have been computed, they are transferred back to the surface CFD mesh in a similar manner [48]. This transfer of data between the two meshes can be summarized with the following equations:

$$\begin{cases} Q_{CTSD} = [P]Q_{CFD} \\ T_{CFD} = [P]^T T_{CTSD} \end{cases} \tag{2-22}$$

$$\begin{cases} F_{CTSD} = [P]F_{CFD} \\ U_{CFD} = [P]^T U_{CTSD} \end{cases} \tag{2-23}$$

where [P] represents the transfer matrix which projects pointwise CFD surface heat fluxes and forces onto the individual structure mesh surface points. The transpose of the matrix is used to obtain the CFD surface temperatures and displacements from the structure mesh [47]. The interpolation patterns which define the [P] matrix are computed by locating the perpendicular projection of each point of the surface CFD mesh on the structure model elements [48]. This is done through a fast parallel search technique, which is based on the minimum distance search [87] in order to locate the closest enclosing face on the exposed surface of the structure mesh for each surface point on the fluid mesh. The final transfer corresponds to a piecewise linear interpolation of the aerodynamic loads, heat fluxes, displacements, and temperature between the two meshes. Hence, matrix P is a matrix of piecewise linear interpolation coefficients.

The in-house developed FSI is capable of working with non-matching fluid and structure meshes with different element types and mesh resolution. Moreover, the FSI has the ability to handle fluid and structure models that have non-matching outer-mold line (OML) geometries [47]. Additionally, the FSI formulation is discretely conservative for the transfer of forces and heat fluxes from the fluid to the structure and satisfies the principle of conservation of virtual work for the transfer of displacements from the structure to the fluid domains [64].

2.2.4 Heat Flux Factor

A heat flux factor is used in NSU3D to convert the computed one-dimensional heat flux to a dimensional value used by AStrO. In NSU3D the non-dimensional heat flux is computed as:

$$q^* = \frac{\gamma}{\gamma-1}\frac{1}{Pr}\mu^*\frac{\partial R^*T^*}{\partial x^*} \tag{2-24}$$

where γ is the ratio of specific heats, Pr is the Prandtl number defined as $Pr = \frac{K}{C_p\mu}$, where k is the heat conductivity and R is the gas constant, and the superscripts denote non-dimensional values. These non-dimensional values are defined as:

$$\begin{cases} \mu^* = \frac{\mu}{\mu_\infty} \\ T^* = \frac{T}{T_\infty} \\ x^* = \frac{x}{L} \\ R^* = \frac{R}{R_\infty} \end{cases} \tag{2-25}$$

Using $R = C_p - C_v$ we obtain:

$$q^* = k\frac{\partial T}{\partial x}\frac{L}{R_\infty T_\infty \mu_\infty} \tag{2-26}$$

Noting that the actual dimensional heat flux is given by $q_{dimensional} = k\frac{\partial T}{\partial x}$ we obtain:

$$q_{dimensional} = q^*\frac{R_\infty T_\infty \mu_\infty}{L} \tag{2-27}$$

and using the definition of the Reynolds number: $Re = \frac{\rho_\infty U_\infty L}{\mu_\infty}$ we obtain:

$$q_{dimensional} = q^*\frac{\rho_\infty R_\infty T_\infty U_\infty}{Re} \tag{2-28}$$

which can also be written as:

$$q_{dimensional} = q^* \frac{P_\infty U_\infty}{Re} \qquad (2\text{-}29)$$

A new heat flux factor must be calculated using the above equation for each specific case study based on the flow conditions.

2.2.5 Mesh Deformation

When dealing with aero-thermo-elastic problems, we require a mesh deformation capability in order to account for the displacements computed by the structural solver in response to the aerodynamic and thermal loads. When running time-dependent problems, we may also have prescribed surface deflections at certain times, such as when simulating prescribed motion of a control surface. Hence, the CFD solver must be modified to take into account the additional dynamics introduced due to the mesh motion, and the fluid equations must be written in the ALE framework [53, 88]. NSU3D employs a discretization that respects the Geometric Conservation Law (GCL) [89] to ensure the flow solver maintains its accuracy and stability in the presence of arbitrary mesh motion. Significant work has been done in the past on the development of a robust and efficient mesh deformation technique [90, 91]. This approach is based on the linear elasticity model and the mesh deformation equations are discretized using a second-order accurate continuous Galerkin finite-element approach [47]. The equations for the mesh deformation are solved using the same line-implicit multigrid algorithm used for solving the flow equations [77].

2.2.6 General Solution Procedure

In this section, a summary of the general solution procedure for the aero-thermo-elastic analysis platform developed in this work is given. As you can see in Figure 2-6, a Gauss-Seidel iteration method is used to couple the fluid, structural, and thermal solvers together. As mentioned earlier this method is proven to have better convergence behavior in comparison to the Jacobi iteration method [57, 58].

The transfer of information for the aero-thermo-elastic analysis process is summarized in Figure 2-7. The flux forward temperature back (FFTB) method or the Dirichlet-Neumann boundary condition is used for the transfer of the thermal boundary conditions. This choice was made since in the literature many researchers have shown that the use of this type of boundary condition is the key to achieving numerical stability and having robust convergence [62, 63]. At each coupling time step a steady-state fluid problem is solved followed by a transient structural and thermal problem. This approach was taken in order to reduce overall computational expense and is justified by the disparity in time scales between the fluid and structural problems [16, 53]. Also, a node-projection scheme is used for the data transfer. This decision was made since we already had an in-house FSI module implemented using the node-projection method for aero-elastic analysis. Updating this module for the transfer of heat fluxes and temperature was the logical next step. As explained in the previous section, a heat flux

23

factor is used in NSU3D to convert the computed one-dimensional heat flux to a dimensional value used by AStrO. This heat flux factor is dependent on the free-stream conditions of the problem.
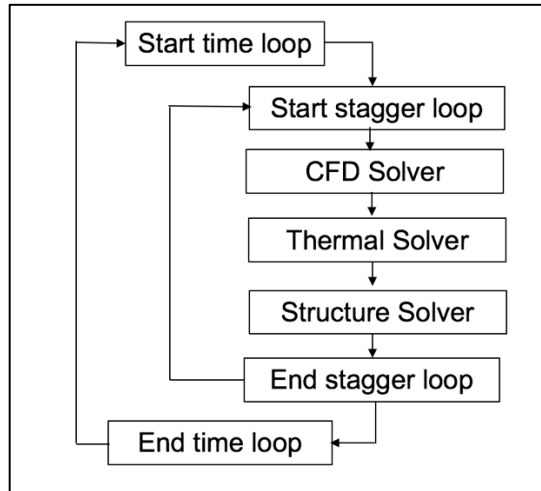
Figure 2-6: Gauss-Seidel iteration method used for the coupled aero-thermo-elastic analysis platform.
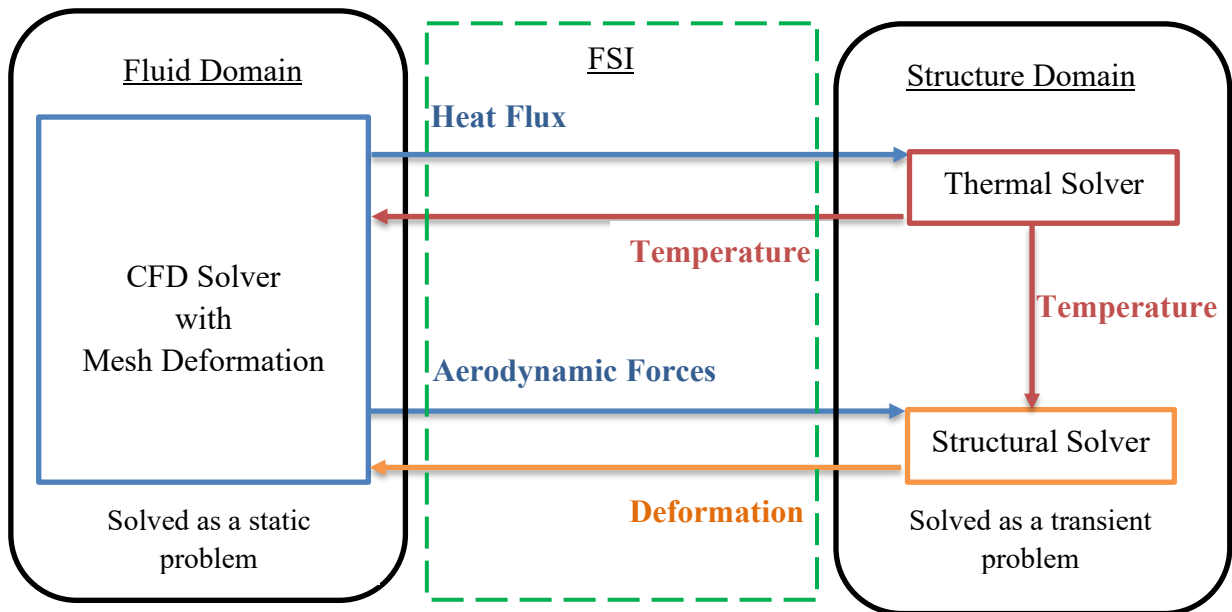
Figure 2-7: Transfer of information for the coupled aero-thermo-elastic analysis platform.

The aero-thermo-elastic problem consists of multiple coupled sets of equations namely, the mesh deformation equation, the flow equations, the thermal equations, the elasticity equations, and the fluid-structure interface transfer equations. The system of equations to be solved can be written in non-linear residual form, as:

$$R_x(u_x, x_{surf}) = 0 \tag{2-30}$$

$$R_F(u_F, u_x, T_{surf}) = 0 \tag{2-31}$$

$$G_S(F_B(u_F, u_x)) = 0 \tag{2-32}$$

$$G_T(H_B(u_F, u_x)) = 0 \tag{2-33}$$

$$R_S(u_S, u_T, F_B(u_F, u_x)) = 0 \tag{2-34}$$

$$R_T(u_T, H_B(u_F, u_x)) = 0 \tag{2-35}$$

$$G'_S(x_{surf}, u_S) = 0 \tag{2-36}$$

$$G'_T(T_{surf}, u_T) = 0 \tag{2-37}$$

where R_x, R_F, R_S, R_T, represent the residual of the mesh deformation, fluid, elastic, and thermal analysis problem respectively. Note that the mesh motion residual depends also on the surface deflections x_{surf} introduced by the structural domain. Moreover, the fluid residual has a dependence on the surface temperatures T_{surf} coming from the structural domain. In the above equations, variables G_S, G'_S, G_T, G'_T represent the residuals of the FSI equations for aero-elastic and aero-thermal data transfer respectively. The solution of the coupled aero-thermo-elastic problem consists of performing multiple coupling integrations on each discipline using the latest available values from the other disciplines.

On the first coupling iteration, $x^c_{surf} = 0$ (superscript c denotes the coupling iteration index) and the solution of the mesh deformation equation is trivial, although non-zero values of x_{surf} are produced at subsequent coupling iterations as the structure deflects in response to the aerodynamic loads and changes in temperature. From a disciplinary point of view, the flow solver produces updated values of u_F and u_x, which are used to compute $F_B(u_F, u_x)$ pointwise surface forces, and $H_B(u_F, u_x)$ pointwise surface heat fluxes. These surface forces and heat fluxes are inputs to the FSI module which returns surface displacements x_{surf}, and surface temperatures T_{surf}. These new surface displacements are then fed back into the mesh deformation equations. The new surface temperatures are also used in the fluid equations. Then

the entire procedure is repeated until convergence is obtained for the coupled aero-thermo-elastic problem.

2.3 Summary

In this chapter, we first looked at the challenges faced in multi-disciplinary analysis problems, in particular, aero-thermo-elastic analysis. Next, a review of the literature was done in order to find the best ways to deal with each of these challenges. Finally, a description of the aero-thermo-elastic analysis platform developed in this work was provided.

3 ANALYSIS RESULTS

This chapter presents validation and results for the computational framework used and developed in this work. As mentioned before, the flow solver NSU3D and AStrO's elasticity capability have been validated in many previous works [47, 48, 50, 74-78]. In addition, the coupled aero-elastic analysis capabilities of NSU3D and AStrO have been demonstrated in past work [42, 47, 48, 50]. In this work a more thorough validation was done on the thermal and thermo-elastic analysis capabilities of AStrO. These verifications were required before moving on to the aero-thermo-elastic coupling. In the final part of this chapter, results are presented for the aero-thermo-elastic analysis capability developed in this work.

3.1 Structural Solver Validation

In this section, first validation results are presented for AStrO's heat conduction solution capability. This is followed by validation results for AStrO's thermo-elastic capability.

3.1.1 Thermal Analysis Capability Validation

In the following, a description of the tests used to validate the heat conduction capability of AStrO is presented. The temperature solutions calculated by AStrO are compared against analytical solutions. We have taken into account transient cases involving one-dimensional and two-dimensional heat conduction were considered. In this study, the same validation problems presented in reference [13] are used. The following results were first published in reference [5].

To validate AStrO's thermal analysis capability, canonical heat conduction problems are used. The transient heat equation is Eq. (3-1), which was previously presented in Chapter 2. For the cases in this section the volumetric heat source Q is assumed to be zero.

$$\rho c \frac{\partial T}{\partial t} + \nabla \cdot (k \nabla T) = 0 \tag{3-1}$$

Four different transient cases have been taken into account for this validation study. For the first three cases, the geometry used is a three-dimensional cube with a length of $0.01m$ in the x-, y-, and z-directions. The mesh used for the cube has 9,261 nodes and 8,000 linear hexahedral elements. For the last transient case, a quarter cylinder geometry is considered. The quarter cylinder mesh has 14,535 nodes and 12,800 linear hexahedral elements. In the following, each case is presented in more details and the computational temperature solutions are compared with the analytical solutions. Please refer to Table 3-1 for all the material properties in the cases discussed in the coming pages.

Table 3-1 Material properties and details of the geometry for the transient heat conduction cases [13].

Property	Value
Initial temperature (T_0)	300 K
Length of bar (l)	0.01 m
Thermal conductivity (k)	10 W/(m.K)
Density (ρ)	8000 kg/m³
Specific heat capacity (C)	500 J/(kg.K)
Thermal diffusivity (α)	2.5 ×10⁻⁶ (m²/s)
Heat transfer coefficient (H)	1000 W/(m².K)

3.1.1.1 *Transient Heat Conduction with Dirichlet Boundary Condition and Constant Thermal Properties in a Cube*

For this first case, a heat conduction problem in one dimension with constant thermal properties is considered. A Dirichlet boundary condition is applied at $x = 0.01m$ with a fixed uniform temperature of $T_D = 500K$. The analytical solution is obtained from Eq. (3-2) [13, 92].

$$\frac{T(x,t) - T_0}{T_D - T_0} = 1 - \frac{4}{\pi} \sum_{n=0}^{\infty} \frac{(-1)^n}{2n+1} \exp\left(\frac{-(2n+1)^2\pi^2}{4} \cdot \frac{at}{l^2}\right) \cos\left(\frac{(2n+1)\pi}{2} \cdot \frac{x}{l}\right) \tag{3-2}$$

Figure 3-1 shows a comparison of the temperature solution for both the analytical and computational methods at different time instances for different x locations in the cube. As can be seen the computational results agree well with the analytical solution.
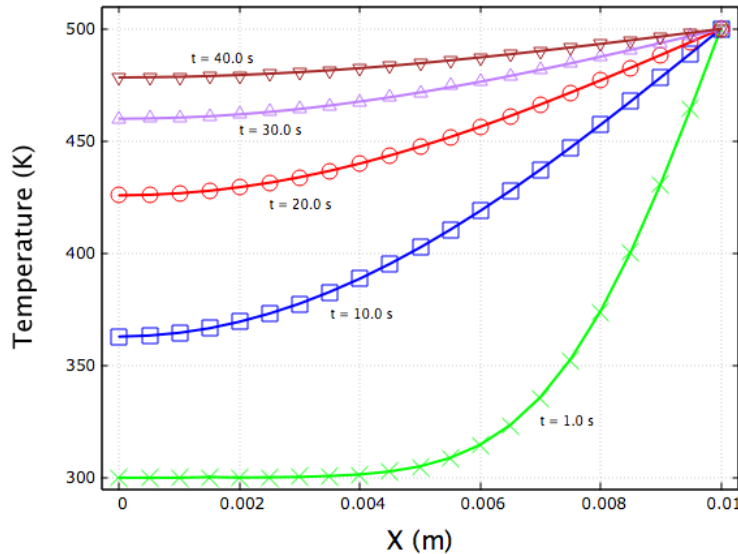
Figure 3-1 Comparison of the temperature distribution from AStrO with analytical solution for the case of transient heat conduction with Dirichlet boundary condition and constant thermal properties, in a cube.

3.1.1.2 *Transient Heat Conduction with Neumann Boundary Condition and Constant Thermal Properties in a Cube*

In this second case, instead of applying a Dirichlet boundary condition to one side of the cube as was done in the previous case, a Neumann boundary condition was applied. A constant heat flux of $q_b = 7.5 \times 10^5 \ W/m^2$ is applied at $x = 0.01m$. Again, constant thermal properties are assumed. The computational solution is compared with the analytical solution obtained from Eq. (3-3) [13, 93].

$$\frac{T(x,t) - T_0}{q_b l/k} = \frac{at}{l^2} + \frac{1}{3} - \frac{x}{l} + \frac{1}{2}\left(\frac{x}{l}\right)^2 - \frac{2}{\pi^2}\sum_{n=1}^{\infty}\frac{1}{n^2}\exp\left(-n^2\pi^2\frac{at}{l^2}\right)\cos\left(n\pi\frac{x}{l}\right) \qquad (3\text{-}3)$$

The computational results for the temperature distribution along the length of the cube at $t = 4s$ are shown in Figure 3-2 and Figure 3-3.
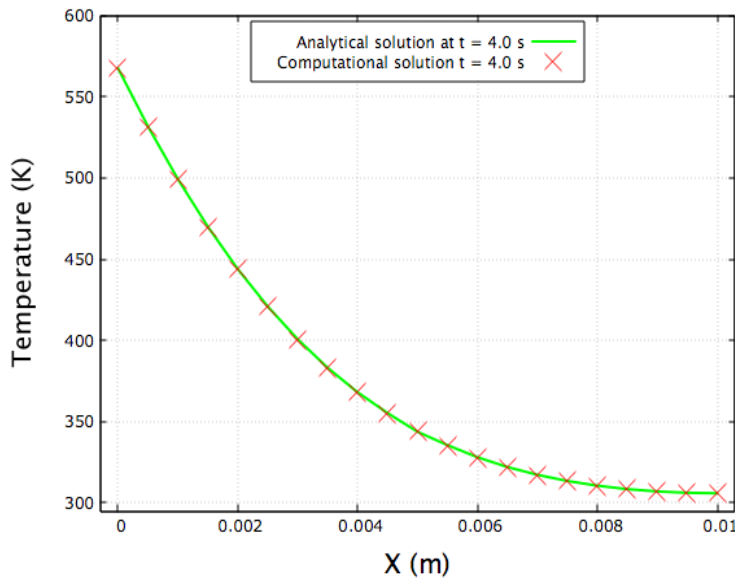
Figure 3-2 Comparison of the temperature distribution from AStrO with analytical solution for the case of transient heat conduction with Neumann boundary condition and constant thermal properties, in a cube at $t = 4s$.
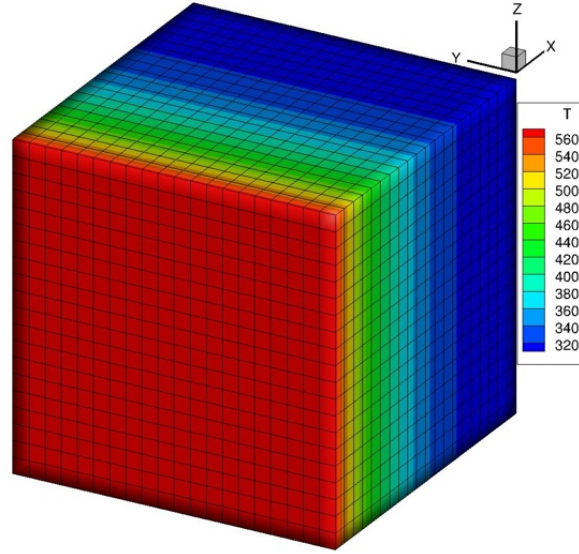
Figure 3-3 Temperature distribution from AStrO for the case of transient heat conduction with Neumann boundary condition and constant thermal properties, in a cube at $t = 4s$.

3.1.1.3 *Transient Heat Conduction with Neumann Boundary Condition and Variable Thermal Properties in a Cube*

Here, the same problem as the previous section is taken into account, however, now variable thermal properties are assumed: $\kappa = k\ (T)$ and $c = C\ (T)$. Hence, the problem is still a one-dimensional heat conduction problem in a three-dimensional cube with a Neumann boundary condition at $x = 0.01m$. However, the values of κ, c, and α all change with changes in temperature as shown in Eq. (3-4) , Eq. (3-5) and Eq. (3-6) respectively:

$$k(T) = k_1 + \frac{k_2 - k_1}{T_2 - T_1}(T - T_1) \tag{3-4}$$

$$C(T) = C_1 + \frac{C_2 - C_1}{T_2 - T_1}(T - T_1) \tag{3-5}$$

$$\alpha = \frac{k_1}{\rho C_1} = \frac{k_2}{\rho C_2} = \frac{k(T)}{\rho C(T)} \tag{3-6}$$

The analytical solution for this specific problem is obtained through the use of Eq. (3-7) [13, 94].

$$\frac{\theta(x,t) - \theta_0}{q_b l/k} = \frac{at}{l^2} + \frac{1}{3} - \frac{x}{l} + \frac{1}{2}(\frac{x}{l})^2 - \frac{2}{\pi^2}\sum_{n=1}^{\infty}\frac{1}{n^2}\exp\left(-n^2\pi^2\frac{at}{l^2}\right)\cos\left(n\pi\frac{x}{l}\right) \tag{3-7}$$

where:

$$\theta_0 = (T_0 - T_1) + \frac{k_2 - k_1}{T_2 - T_1}\frac{1}{2k_1}(T_0 - T_1)^2 \,, \theta = (T - T_1) + \frac{k_2 - k_1}{T_2 - T_1}\frac{1}{2k_1}(T - T_1)^2 \qquad (3\text{-}8)$$

The values of the thermal properties used in this problem can be found in   Four different transient cases have been taken into account for this validation study. For the first three cases, the geometry used is a three-dimensional cube with a length of 0.01m in the *x*-, *y*-, and *z*-*directions*. The mesh used for the cube has 9,261 nodes and 8,000 linear hexahedral elements. For the last transient case, a quarter cylinder geometry is considered. The quarter cylinder mesh has 14,535 nodes and 12,800 linear hexahedral elements. In the following, each case is presented in more details and the computational temperature solutions are compared with the analytical solutions. Please refer to Table 3-1 for all the material properties in the cases discussed in the coming pages.

Table 3-1 presented previously and Table 3-2 shown here.

Table 3-2 Variable thermal properties for the cube [13].

$T\,(K)$	$K\,(w/m.K)$	$C\,(J/kg.K)$
$T_1 = 300$	$K_1 = 10$	$C_1 = 500$
$T_2 = 1300$	$K_2 = 100$	$C_2 = 5000$

Figure 3-4 provides a comparison of the analytical and computational temperature solution along the length of the cube at $t = 4s$. As can be seen the numerical solution follows the analytical solution very closely. The temperature distribution as calculated by AStrO is shown in Figure 3-5.
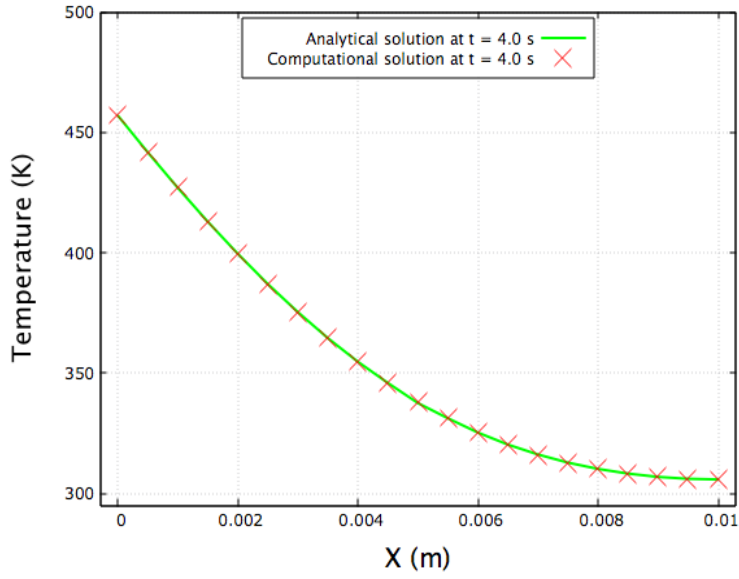
Figure 3-4 Comparison of the temperature distribution from AStrO with analytical solution for the case of transient heat conduction with Neumann boundary condition and variable thermal properties in a cube.
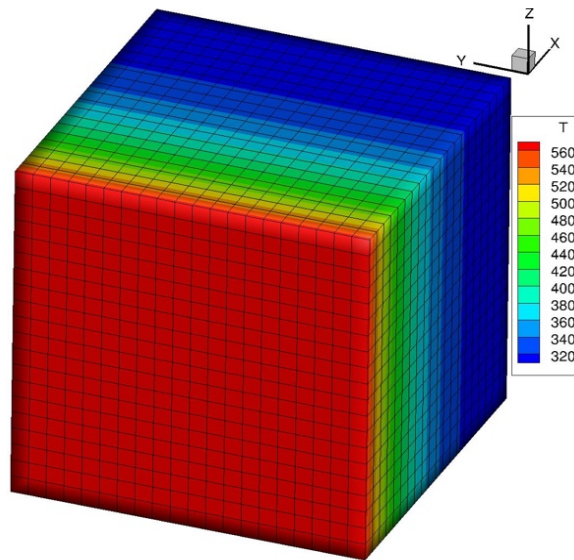
Figure 3-5 Temperature distribution from AStrO for the case of transient heat conduction with Neumann boundary condition and variable thermal properties, in a cube at $t = 4s$.

32

3.1.1.4 *Transient Heat Conduction with Prefect Gas Convection on a Cylinder*

In the previous sections one-dimensional heat conduction problems were looked at. However, In this section, a heat conduction problem in two-dimensions is considered. Here, heat conduction in a quarter cylinder is studied. A Neumann boundary condition is prescribed by perfect gas convection at the locations where the radius of the cylinder is $r_0 = 0.01m$. This case has a variable heat flux applied and this value is updated by the wall temperature through Eq. (3-9) as:

$$q_b = -H(T_r - T_W) \tag{3-9}$$

where H is the heat transfer coefficient, T_W is the wall temperature, and T_r is the reference temperature which for this problem is taken as $T_r = 1300K$. As mentioned before, T_W is not constant and changes with time, and hence so does the value of q_b.

Assuming constant thermal properties in this case, the analytical solution is given by Eq. (3-10) [13, 95].

$$\frac{T(r,t)-T_r}{T_0-T_r} = \sum_{n=1}^{\infty} k_n J_0 \left(b_n \frac{r}{r_0} \right) exp\left(-b_n^2 Fo\right) \tag{3-10}$$

where:

$$k_n = \frac{2Bi}{(b_n^2+Bi^2)J_0(b_n)} \quad, \quad Bi = \frac{Hr_0}{k} \quad, \quad Fo = \frac{at}{r_0^2} \tag{3-11}$$

In the previous equations, the characteristic values b_n are the roots of the equation:

$$b_n J_1(b_n) = Bi J_0(b_n) \tag{3-12}$$

J_0 and J_1 are the Bessel functions of the first kind. In the above equation Bi and Fo are the Biot and Fourier numbers.

Figure 3-6 and Figure 3-7 show the temperature distribution along the radius of the cylinder at $t = 5s$. The numerical solution from AStrO is shown to compare well with the analytical solution in Figure 3-6.
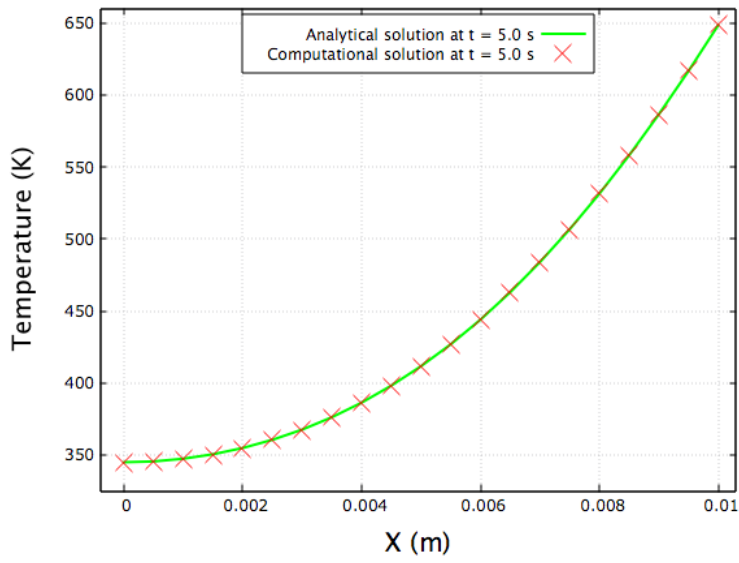
Figure 3-6 Comparison of the temperature distribution from AStrO with analytical solution for the case of transient heat conduction with perfect gas convection on a quarter cylinder at $t = 5s$.
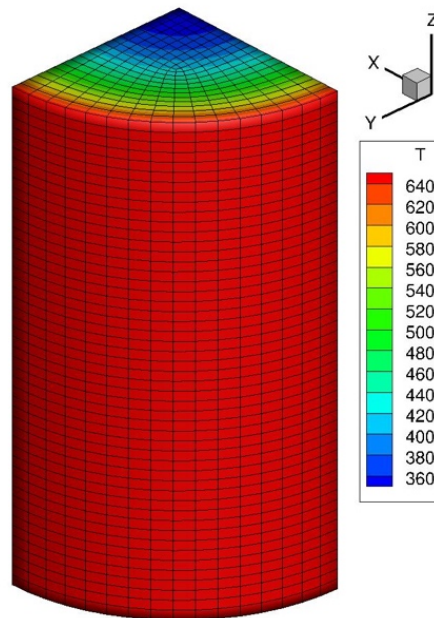
Figure 3-7 Temperature distribution from AStrO for the case of transient heat conduction with perfect gas convection on a quarter cylinder at $t = 5s$. Temperature distribution from AStrO for the case of transient heat conduction with perfect gas convection on a quarter cylinder.

3.1.2 Thermo-Elastic Analysis Capability Validation

This section provides a demonstration of the coupled thermo-elastic modeling capability of AStrO. A heated panel case is taken into account and simulation results are validated against available analytical solutions. These results were first published in reference [5].

3.1.2.1 *Thermo-Elastic Study of a Hated Panel*

A study was done on a heated panel in order to validate AStrO's thermo-elastic analysis capability. We consider the case of a thin panel subjected to aerodynamic heating. This test case was first studied in reference [27] to test an aero-thermo-elastic analysis problem. However, a simplified analytical solution to this problem was given in reference [26] which can also be used to verify the thermo-elastic numerical solution at the early time steps.

3.1.2.1.1 Description of the Heated Panel Computational Set-Up

A schematic of the computational model and boundary conditions for this problem is shown in Figure 3-8. The panel is supported by immovable supports on the left and right edges of the bottom surface. The bottom surface of the panel is insulated, while the faces on the right and left side of the panel have a constant temperature equal to the initial temperature of 530*R*. A uniform heat flux is applied to the top surface of the panel. Under these thermal and structural boundary conditions, the panel deforms into a convex shape [25-27].
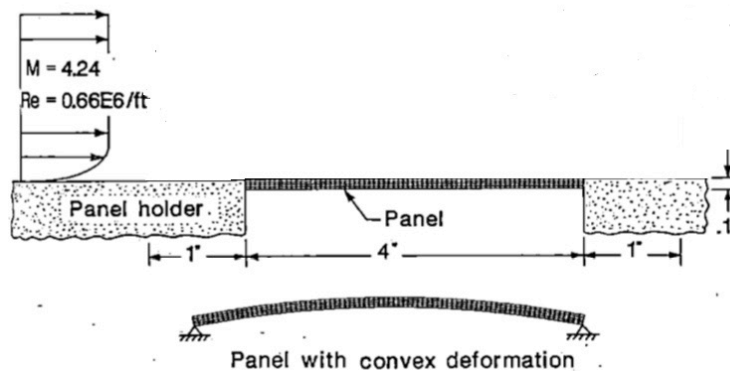
Figure 3-8   Coupled thermal/structural model and boundary conditions for a heated panel reproduced from reference [35].

The test panel is 4*in* long, has a thickness of 0.1*in*, and a width of 0.5*in*. It is made from AM-350 stainless steel. The properties for the panel are tabulated in Table 3-3 [26].

Table 3-3 Panel material properties [26].

Property	Value
Density (ρ)	0.282 *lbm/in³*
Thermal Conductivity (k)	0.12864 ×10⁻³ *BTU/(s.in.R)*
Specific heat capacity (C)	0.11162 *BTU/(lbm.R)*
Thermal expansion (α)	0.62643×10⁻⁵ *1/R*
Modulus of elasticity (E)	0.35346×10⁸ *lbf/in²*
Poisson's ration (v)	0.25 (dimensionless)

3.1.2.1.2 Analytical Solution for the Heated Panel

In this section we present the approximate equations used to obtain the analytical solution for the studied aerodynamically heated panel case as presented in reference [26]. Since we are studying the solution at early times, the heating rate across the panel is nearly uniform, and can be approximated by the following equation [26]:

$$\dot{q}(t) = 0.026 - 0.0001t \; \left(\frac{BTU}{in^2.s}\right) \tag{3-13}$$

Equation (3-13) is used as a thermal boundary condition in order to mimic the aerodynamic heating for the thermo-elastic validation.

At early times, panel temperatures may be estimated by assuming:

1) that energy losses at panel supports are negligible,
2) that radiation energy losses are negligible as a result of low panel temperature,
3) that no panel thickness temperature gradient is permissible for the thin stainless-steel panel.

With these assumptions in mind the average panel temperature can be calculated through the following equation [26]:

$$T_a(t) = \frac{1}{\rho ch} \cdot (0.026t - 0.00005t^2) + T_0 \tag{3-14}$$

where T_0 is the initial panel temperature.

The panel's structural response at early times can be approximated using the beam-column theory. In this theory we assume that deformations are small, shear effects are neglected, and, for cylindrical bending, the beam's flexural rigidity is $D = Eh^3/12(1 - v^2)$, where E is the modulus of elasticity, v is the Poisson's ratio, and h is the panel thickness. Hence, the panel deflection is approximated with the following [26]:

$$v(x) = (^h/_2)(\cos \lambda x/2 - 1) \tag{3-15}$$

where $\lambda = \sqrt{P/D}$, and the axial constraint force P is computed from [26]:

$$\frac{Pl}{hE} + \frac{h^2}{2}\lambda \tan\left(\frac{\lambda l}{2}\right) + \frac{h^2}{8}\frac{P}{D} \times \frac{l}{2} - \frac{sin\lambda l}{2\lambda}/cos^2\frac{\lambda l}{2} - \alpha\Delta Tl = 0 \qquad (3\text{-}16)$$

where $\Delta T = T_a - T_0$, α is the thermal expansion, and l is the length of the panel.

The panel stresses according to beam-column theory are:

$$\sigma_x = -\frac{P}{h} + \frac{6P}{h^2}\frac{\cos(\lambda x)}{\cos(l/2)}y \qquad (3\text{-}17)$$

In the following section we will use the analytical results from Eq. (3-14), Eq. (3-15) and Eq. (3-17) to validate the numerical results from AStrO for the heated panel case.

3.1.2.1.3 Numerical Results for the Thermo-Elastic Analysis of the Heated Panel

In this section, we present the numerical results for the thermo-elastic analysis of the heated panel problem described above. The panel deformations were computed three times at 10s intervals for a test duration of 30s. Two meshes have been used in this study. The coarse mesh has 3,216 nodes, and 1,995 hexahedral elements. The fine mesh has 15,960 nodes and 11,925 hexahedral elements. The results for the temperature, maximum deformations and stresses are shown in Table 3-4, Table 3-5, and

Table 3-6, respectively. The time step used for the coupled thermo-elastic analysis was 0.01s. Hence, 3000 time steps were required to heat the panel for 30s. The computed results are very close to the analytical solutions. The computed results are not exactly the same as the analytical solutions because as explained earlier, the analytical equations themselves involve various assumptions. The computed results from reference [26] also have small variation with respect to the analytical solutions.

Contours of the displacements in the x- and y-directions for the coarse mesh are shown in Figure 3-9 and Figure 3-10. The contours clearly show the convex deformations in the panel.

Table 3-4 Panel temperature solution T (l/2, t) in Rankine.

Time(s)	Computational solution		Analytical solution
	Coarse mesh	Fine mesh	
10	610.997	610.996	606.22
20	688.8299	688.8289	685.31
30	763.4818	763.395	767.28

Table 3-5 Panel deformation v (l/2, t) in inches.

Time(s)	Computational solution		Analytical solution
	Coarse mesh	Fine mesh	
10	0.0138	0.0136	0.0127
20	0.0262	0.0259	0.0234
30	0.0374	0.0370	0.0336

Table 3-6 Panel stresses σ_x (l/2,-h/2, t) in ksi.

Time(s)	Computational solution		Analytical solution
	Coarse mesh	Fine mesh	
10	- 12.223	- 13.588	- 13.2
20	- 23.136	- 25.721	- 24.0
30	- 33.060	- 35.064	- 34.3
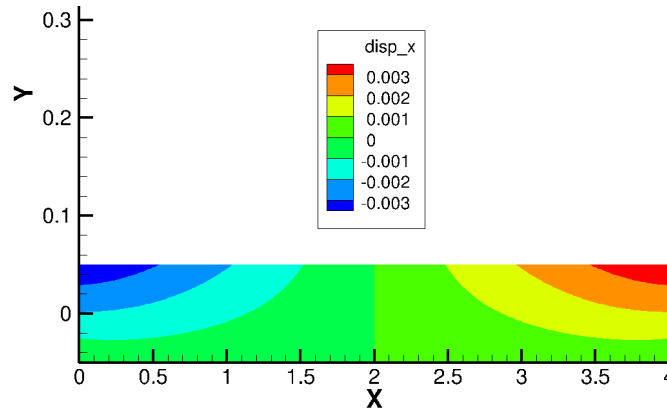
Figure 3-9   Contour of the panel displacement in the *x*-direction at *t* = 30*s* as calculated by AStrO.
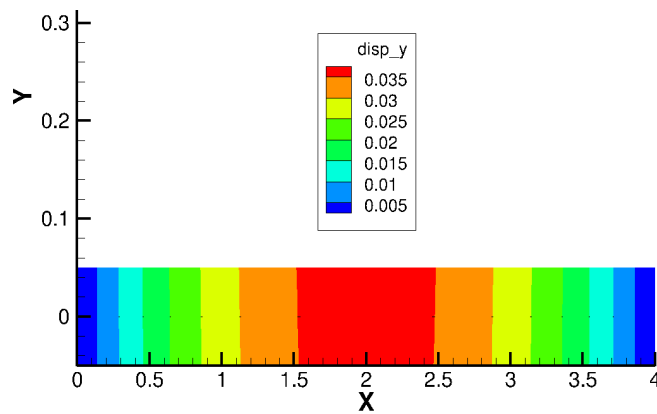
Figure 3-10   Contour of the panel displacement in the *y*- direction at *t* = 30*s* as calculated by AStrO.

3.2 Aero-Thermo-Elastic Analysis Results

In the previous sections of this dissertation, we showed validation results for the thermal and thermo-elastic capabilities of AStrO. Now, we can move on to presenting results for the aero-thermal and aero-thermo-elastic analysis capability.

When an aircraft operates at high speeds, its aero-elastic behavior will be affected by aerodynamic heating and vice versa. Therefore, we look at two applications of hypersonic flows: hypersonic flow over a cylindrical leading edge, and an aerodynamically heated panel.

3.2.1 Hypersonic Flow Over a Cylindrical Leading Edge

Leading edges of hypersonic vehicles experience intense stagnation point pressures and heating rates. These severe temperature levels and gradients can pose significant design challenges [15]. Hence, it is of great importance to study the aero-thermo-elastic analysis of hypersonic flow over leading edges. For these reasons, we study the fluid-thermal-structural behavior of an aerodynamically heated cylindrical leading edge. The coupled analysis is applied to a three-dimensional cylinder as was studied experimentally in reference [96]. These experimental results have been used frequently in the past for validation of aero-thermal and aero-thermo-elastic coupling approaches [15, 16, 23, 97].

In the following, we first look at an overview of the wind tunnel experiment. Next, a brief description of the fluid and structure meshes used in this numerical study is given. Finally, we present numerical results for the predicted pressure, wall heating-rates, temperature distribution, and stresses. These results are compared with experimental data [96] and results from previous computational work [15, 16, 23, 97] for validation.

3.2.1.1 *An Overview of Wind Tunnel Experiment for Flow Over a Cylindrical Leading Edge*

The solution for Mach 6.47 flow over a cylinder is used to demonstrate and validate the integrated flow-thermal-structural analysis approach. A schematic of the experiment performed in 1987 by Allan Wieting [96] in the NASA Langley 8-foot High Temperature Tunnel is shown in Figure 3-11. The initial free-stream flow parameters are summarized in Table 3-7. The length, diameter, and thickness of the cylinder used are: $0.1143m$, $0.0762m$, and $0.0127m$, respectively. The material properties of stainless steel 321 used for the cylinder are shown in Table 3-8. Approximately fifty pressure taps, and coaxial thermocouples were placed circumferentially along the cylinder surface to allow the accurate measurement of the aerodynamic pressure and heating rate distributions. More details regarding the experimental configuration, flow conditions and results can be found in reference [96].

Table 3-7 Initial free-stream conditions for the flow [96].

Free-stream conditions	Value
Free-stream Mach number (Ma_∞)	6.47 (dimensionless)
Wall temperature (T_w)	294.4 K
Free-stream Reynolds number (Re_∞)	1.312×10^6 $1/m$
Free-stream temperature (T_∞)	241.5 K
Free-stream velocity (U_∞)	2015.43 m/s
Free-stream pressure (P_∞)	648.1 Pa
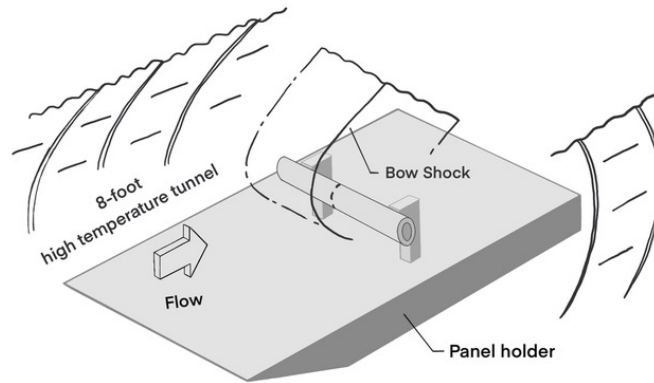
Figure 3-11   Experimental configuration for flow over a cylinder in the 8-Foot High Temperature Tunnel reproduced from reference [15].

Table 3-8 Material properties of 321 stainless steel at 400K [23].

Property	Value
Density (ρ)	8030 kg/m^3
Thermal Conductivity (k)	16.24 $W/(m.K)$
Specific heat capacity (C)	502.48 $J/(kg.K)$
Thermal expansion (α)	0.0000166 $1/K$
Modulus of elasticity (E)	2×10^{11} Pa
Poisson's ration (v)	0.3 (dimensionless)

3.2.1.2   *Description of Grids Used for the Numerical Simulation for Flow Over a Cylindrical Leading Edge*

For this study, two sets of meshes were created for both the fluid and the structure domains: a coarse and a fine mesh. Description of these fluid and structure meshes are provided in Table 3-9 and Table 3-10, respectively. The coarse fluid and structure mesh used are shown next to each other in Figure 3-12. Since the location of the shock was known from the experimental data, we have refined the fluid mesh close to the location of the shock to allow for a more

accurate shock resolution. The grid spacing in the normal direction at the wall of the cylinder was determined in order to achieve a y^+ value less than one in the coarse mesh.

The fluid meshes are finer on the interface than the structure meshes, as is usually the case for these types of problems. However, the FSI module used in this work is able to handle this non-matching interface.
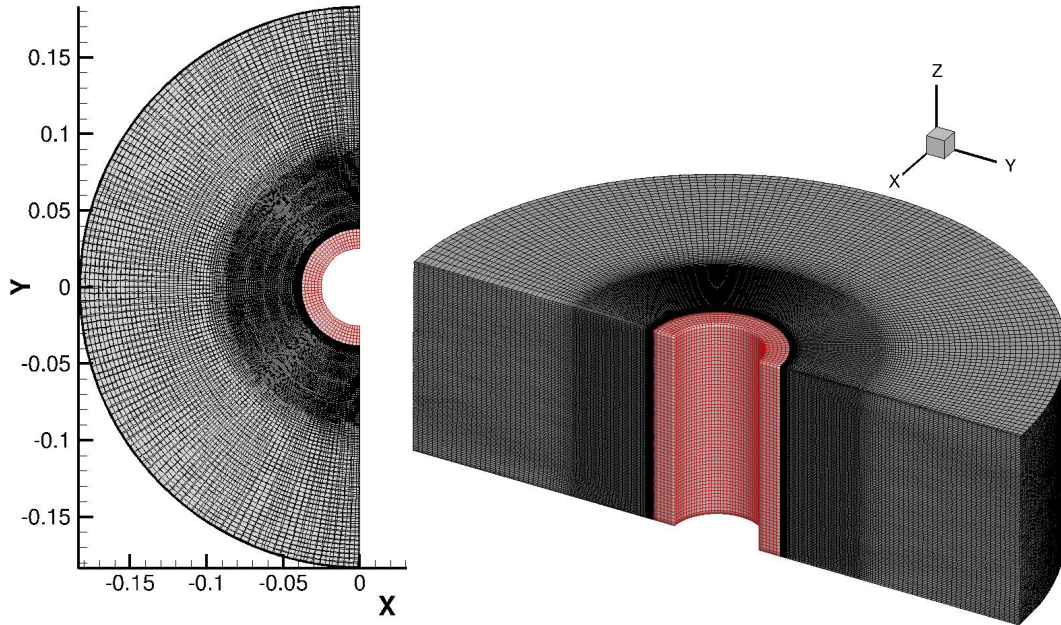
Figure 3-12 Fluid and structure coarse meshes for the aero-thermo-elastic analysis problem of hypersonic flow over a leading cylindrical edge (fluid mesh in black and structure mesh in red). Table 3-9 Details of the two fluid meshes used in the aero-thermo-elastic analysis for flow over a cylinder.

Fluid Mesh	Number of nodes	Number of elements	Type of elements	Wall spacing
Fluid coarse mesh	2,462,400	4,814,740	Prism	10^{-6}
Fluid fine mesh	19,763,866	39,084,360	Prism	6×10^{-7}

Table 3-10 Details of the two structure meshes used in the aero-thermo-elastic analysis for flow over a cylinder.

Structure Mesh	Number of nodes	Number of elements	Type of elements
Structure coarse mesh	20,706	17,100	Hexahedral
Structure fine mesh	133,055	120,384	Hexahedral

3.2.1.3 Summary of Applied Numerical Boundary Conditions for Flow Over a Cylindrical Leading Edge

The boundary conditions applied to the coupled problem are summarized in Figure 3-13. The inner surface of the cylindrical shell is prescribed an isothermal boundary condition of 294.4K, since the experimental time is very short. On the outer surfaces of the cylinder (fluid/structure interface), a heat flux is applied on the structure side, and temperature boundary condition supplied from the structural solver is applied on the fluid side. Since we are simulating only half of the cylinder, an insulated thermal boundary condition is applied at boundary 5 in Figure 3-13.

For the elastic boundary conditions, we assume that the cylinder is supported rigidly by stands at the leeward side near the tip (boundary 5 in Figure 3-13). Consequently, the structure can have displacements in the y- and z-directions but not in the x-direction.
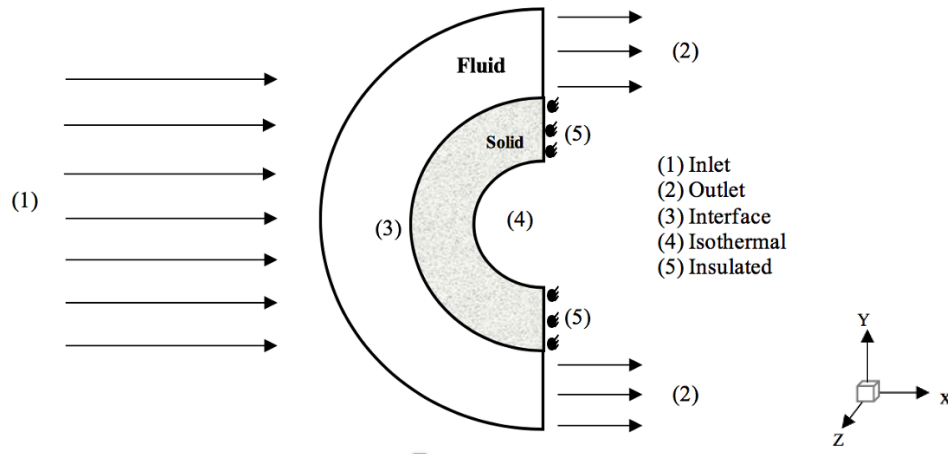
Figure 3-13 Applied boundary conditions for the aero-thermo-elastic problem of hypersonic flow over a leading cylindrical edge.

3.2.1.4 Validation of CFD Solver for High Speed Flows

In this section, the main goal is to show that the flow solver is able to capture the physics in the flow-field correctly for high speed flows. The flow solution for pressure obtained from the fine mesh is shown in Figure 3-14. The flow-field is characterized by the bow shock that stands off the cylindrical leading edge. The predicted location of the shockwave is at x = - 0.0545m, the predicted temperature and pressure behind the shockwave are approximately 2300K, and 35000Pa respectively, which all compare well with the previous work [15, 16, 23, 97].

The pressure and temperature distributions along the centerline of the upstream flow domains for the fine mesh are shown in Figure 3-15 and Figure 3-16. The freestream temperature increases suddenly from 241.5K to about 2300K across the shock and then drops sharply again to the wall temperature 294.4K due to the isothermal boundary condition used.

This steep temperature gradient which occurs in a very thin thermal boundary layer, produces a high stagnation point heating rate.
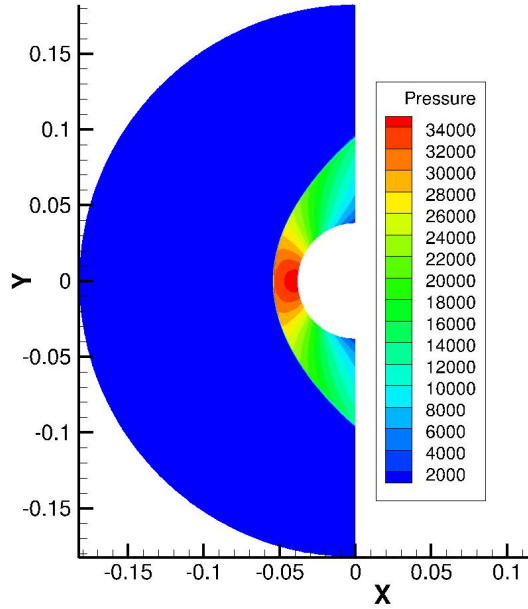
Figure 3-14 Pressure contours in the flow field of a cylinder subjected to Mach 6.47 from the uncoupled simulations for the fine mesh.
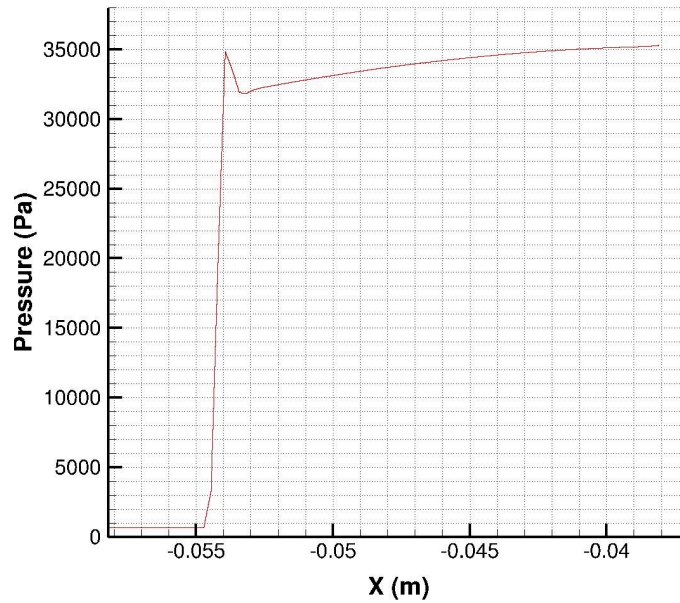
Figure 3-15 Fluid pressure distribution along the centerline of a cylinder subjected to Mach 6.47 from the uncoupled simulations for the fine mesh.

43
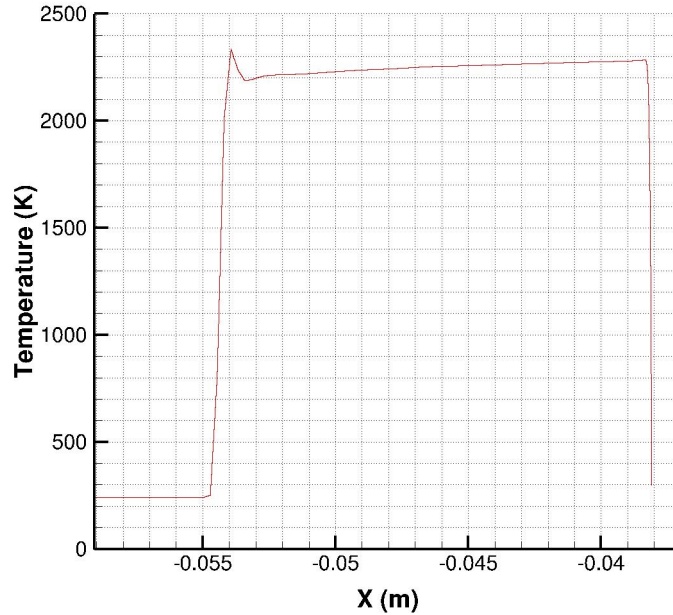
Figure 3-16   Fluid Temperature distribution along the centerline of a cylinder subjected to Mach 6.47 from the uncoupled simulations for the fine mesh.

Figure 3-18 shows the comparison between the computed aerodynamic loads for the uncoupled case along the cylinder surface and the experimental data. In previous work the values in this plot were normalized with respect to the stagnation point pressure value. Hence, in we have presented the predicted and experimental pressures normalized by their respective stagnation point values P_0, which are shown in Table 3-11. This figure shows a good agreement between the computed aerodynamic pressure distribution from both the fine and coarse meshes with the experimental data. In Table 3-11, we also have the theoretical (perfect gas) value for the stagnation pressure computed using the normal shock relations. The computed stagnation point pressure solution is very close to the theoretical value calculated as the computational results assume a perfect gas. The results are almost identical for the coarse and fine mesh. The difference between the predicted and experimental stagnation-point pressure is within 7%. This holds for both the fine and coarse mesh.

Table 3-11 Comparison of the computed stagnation point parameters with experimental data for the cylinder subjected to Mach 6.47 for the uncoupled simulations.

Stagnation point parameters	Computational-CFD only		Experimental	Theoretical (perfect gas)
	Coarse mesh	Fine mesh		
Pressure (P₀)	34,995.83 Pa	3,5147.66 Pa	37921.2 Pa	3,5231.16 Pa
Heating rate (q₀)	471.68 KW/m²	469.66 KW/m²	670 KW/m²	
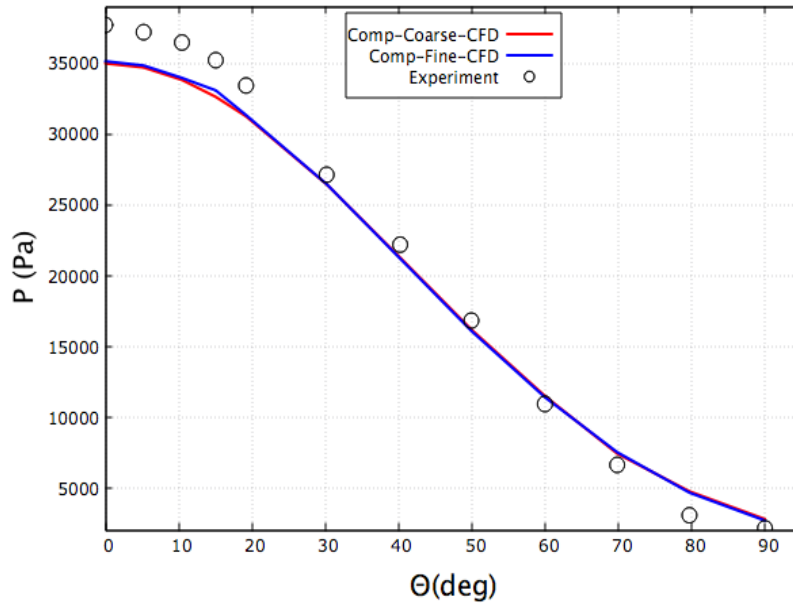
Figure 3-17 Comparison of simulated surface pressure distributions with experimental data for the cylinder subjected to Mach 6.47 from the uncoupled simulations for the course and fine meshes.
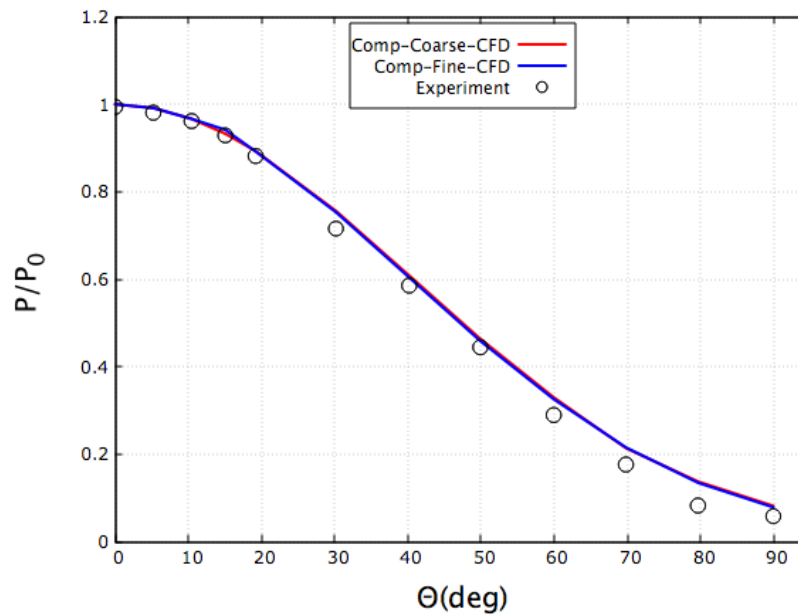
Figure 3-18 Comparison of simulated surface pressure distributions with experimental data for the cylinder subjected to Mach 6.47 from the uncoupled simulations for the course and fine meshes normalized by the respective stagnation point pressure value.

The main challenge in the fluid analysis is the prediction of the aerodynamic heating rates. This is due to the large temperature gradients which occur in the very thin thermal boundary layer near the cylinder wall. In previous work the heat rates were normalized with respect to the stagnation point heating rate value, and hence we have done the same here. The predicted heating rate distribution for the uncoupled case are shown in Figure 3-19. The normalized heating rates compare well with the experimental results as shown in Figure 3-19. The predicted heating rate for the coarse and fine meshes are normalized by their respective stagnation point values q_0, as shown in Table 3-12. The stagnation point heating rate changes by less than 0.4% between the coarse and fine grids and compares well with the previously computed results from references [15] and [23]. However, as with the results from previous studies, the predicted heating rate is lower than the experimental values as shown in Table 3-11, which is also the case for the Fay-Riddell and viscous shock layer solutions shown in Table 3-12.

Table 3-12 Stagnation point heating rate from previous work for the cylinder subjected to Mach 6.47 for the uncoupled simulations.

	Fay-Riddell solution [23, 98]	*Viscous shock-layer solution [23, 99]*	*Computational results from reference [15]*	*Computational results from reference [23]*	*Current work-fine mesh*
Stagnation point heating rate (q_0)	482.6 KW/m^2	470.1 KW/m^2	482.6 KW/m^2	485.5 KW/m^2	469.66 KW/m^2
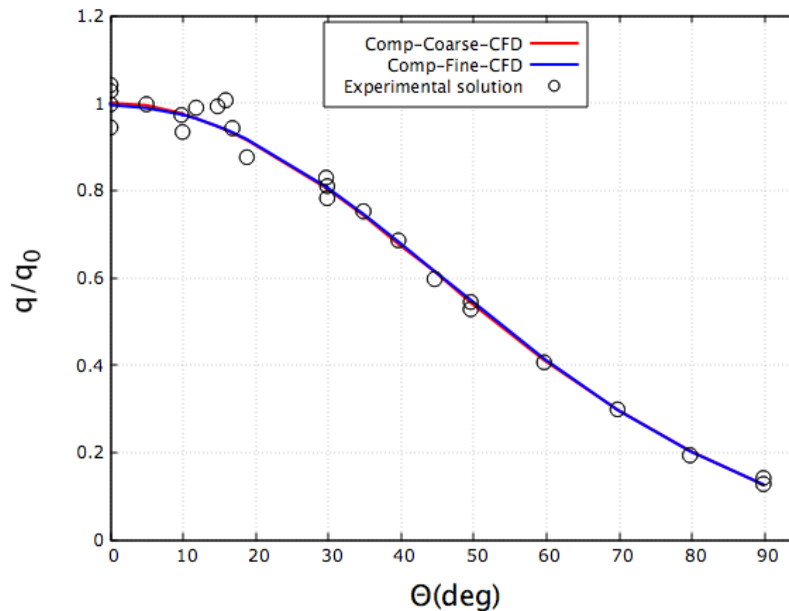
Figure 3-19 Comparison of simulated surface heating rate distributions with experimental data for the cylinder subjected to Mach 6.47 from the uncoupled simulations for the course and fine meshes.

From these results it can be observed that our solutions are in good agreement with previous CFD work. The difference between the predicted and the experimental heating rate has not yet been resolved by us or others in the past. Since the total enthalpy of the experimental flow is relatively low, real gas effects can be expected to play a minor role. Furthermore, any real gas effects would tend to reduce the observed heating rate and thus the lower computational heating rate values are likely not due to real gas effects.

3.2.1.5 *Coupled Analysis Results*

In this section, we present solutions for the coupled aerodynamic and aero-thermal loads on the cylinder. Following previous work, we assume that the flow field reaches equilibrium instantaneously compared to the thermal response of the cylinder. Hence, the coupled problem is solved in a lagged transient manner, where the flow problem is considered a steady-state problem at every time interval. The time step for the thermal solver is taken as 0.1*s*. Thus, it takes 20 coupling cycles between the fluid and structure solvers to reach the transient solution at t = 2*s*. At each coupling time step a static fluid problem is solved followed by a transient structural and thermal problem.

The simulations were performed on the Cheyenne supercomputer at NCAR-Wyoming Supercomputing Center (NWSC). The computational cost of the coupled analysis problem for the cylinder cases with the coarse mesh presented in this work is approximately 48 minutes of wall-clock time on 240 cores. The computational cost of the coupled analysis problem for the cylinder cases with the fine mesh is approximately 140 minutes of wall-clock time on 720 cores. For the cylinder problems the flow is converged up to more than three orders of magnitude, and the structure problem up to machine precision (since it uses a direct method).

By taking the aero-thermal coupling into account, the aerodynamic heating rate decreases over time as the surface temperature of the cylinder increases. The stagnation point heating rate decreases in both the coarse and the fine mesh, from t = 0s to t = 2s. These values are presented in Table 3-13. The drop in the stagnation point heating rate with time is clear in Figure 3-20. The predicted heating rate for the coarse and fine meshes are normalized by their respective stagnation point values q_0, which is the initial heating rate presented in Table 3-12 and Table 3-13.

Table 3-13 Comparison of the computed stagnation point parameters for the cylinder subjected to Mach 6.47 from the coupled analysis at t = 0s and t =2s.

Stagnation point parameters	*Computational-coupled at t = 0s*		*Computational-coupled at t = 2s*	
	Coarse mesh	*Fine mesh*	*Coarse mesh*	*Fine mesh*
Pressure (P$_0$)	34,995.83 *Pa*	35,147.66 *Pa*	34,997.69 *Pa*	35,147.81 *Pa*
Heating rate (q$_0$)	471.68 *KW/m²*	469.66 *KW/m²*	444.07 *KW/m²*	438.52 *KW/m²*
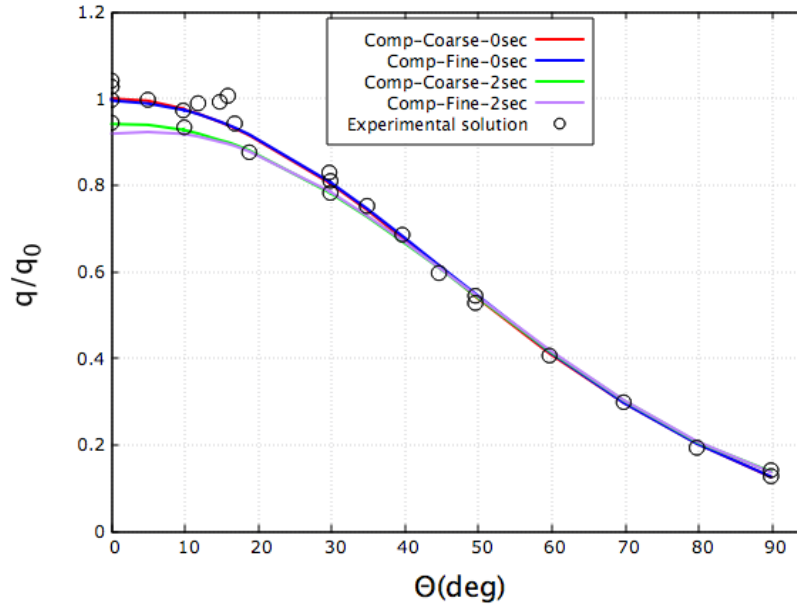
Figure 3-20 Comparison of the simulated surface heating rate distributions with experimental data for the cylinder   subjected to Mach 6.47 from the coupled analysis at t = 0*s* and t = 2*s*.

Figure 3-21 shows the evolution of the temperature at the fluid/structure interface for t = 0, 2, 4, 6*s*. It can be seen that the cylinder surface temperature gradually increases with time. This rise in surface temperature creates an overall decrease in the heating rate. Figure 3-22 shows the evolution of the heating rate distribution as the cylinder temperature rises at t = 0, 2, 4, 6*s*. It can be concluded that the coupled aero-thermal analysis is necessary, otherwise the heating-rate would be overestimated, which in turn may impact the structural design requirements.

The cylinder temperature contours from the fine mesh at t = 2*s* are shown in Figure 3-23. This figure shows a maximum temperature of about 385*K* at the stagnation point, which matches well with the result from reference [15] at 2*s*. The circumferential thermal stress distribution on the cylinder as computed by AStrO are shown in Figure 3-24. These results agree well with the results presented in reference [15]. The maximum stress occurs on the outer surface of the cylinder near the stagnation point and has a value of -198*MPa*. This is due to the high temperature gradients taking place in this region. For this case the deformation and stress are mainly the results of the thermal loads and the effect of the aerodynamic loads can be ignored due to the relatively low dynamic pressure in the experimental setup. The deformation of the cylinder within the profile is negligible compared with the cylinder diameter, because of the relatively low temperature change inside the structure. Hence, the coupling in this problem is primarily between the fluid and thermal solver.

48
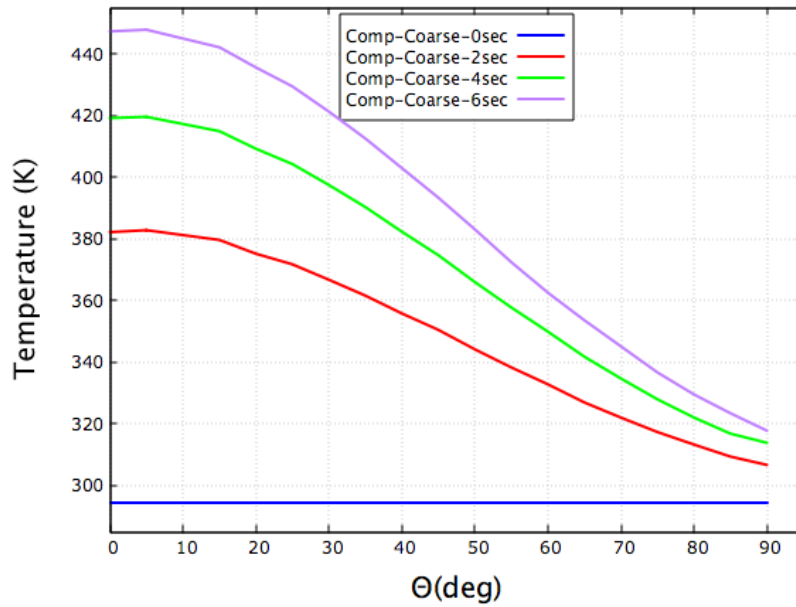
Figure 3-21 Time evolution of the surface temperature distributions for t = 0, 2, 4, 6*s* for the cylinder subjected to Mach 6.47 from the coupled analysis for the coarse mesh.
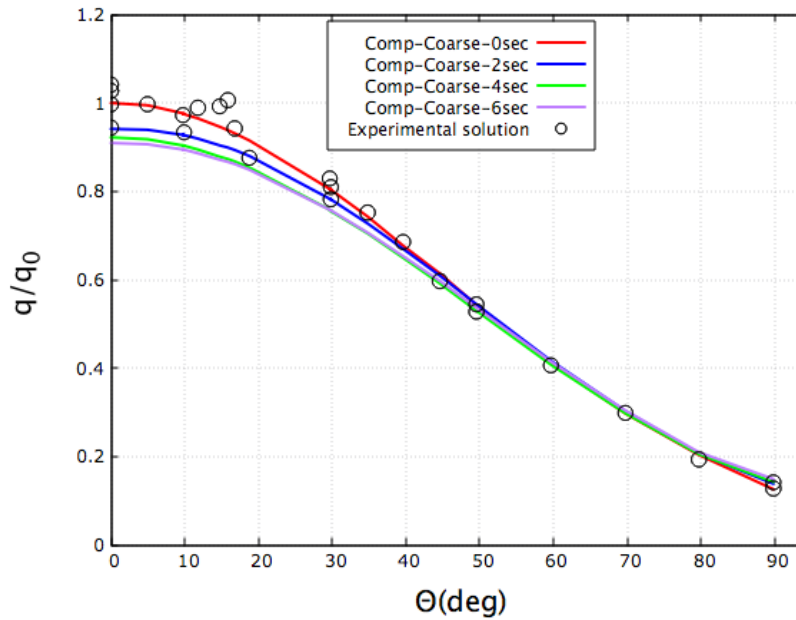
Figure 3-22 Time evolution of the surface heating rate distributions for t = 0, 2, 4, 6*s* for the cylinder subjected to Mach 6.47 from the coupled analysis for the coarse mesh.
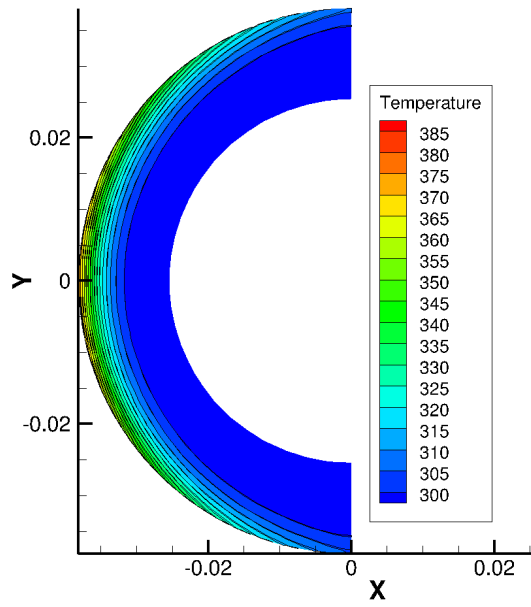
Figure 3-23 Temperature contours for the cylinder subjected to Mach 6.47 at t = 2*s* from the coupled analysis for the fine mesh.
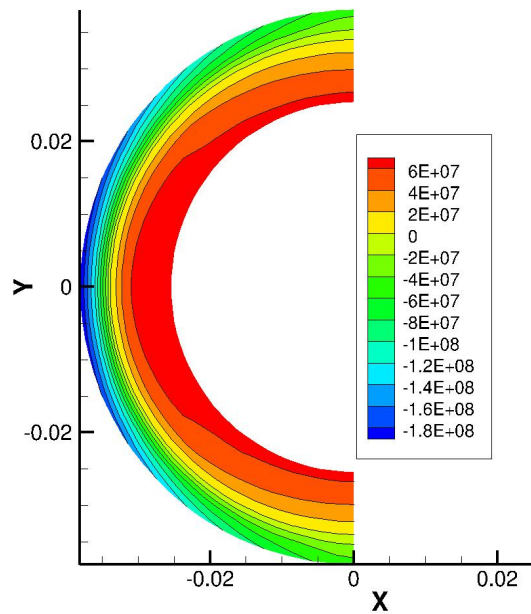
Figure 3-24 Circumferential stress contours for the cylinder subjected to Mach 6.47 at t = 2*s* from the coupled analysis for the fine mesh.

3.2.2 Aerodynamically Heated Panel

As mentioned previously, the fluid/thermal/structural interactions play an important role in many design problems. One such problem is the thermal protection systems on hypersonic flight vehicles. The study of aerodynamically heated panels is a preliminary but important step towards the objectives of analyzing more realistic material and structures for such vehicles [25]. With this in mind, the second application we will study with the developed aero-thermo-elastic analysis capability is the heated panel case discussed previously. Earlier, we used this example to validate the thermo-elastic capability of AStrO by applying an approximate heat flux on the upper part of the panel. However, in this section we use the aero-thermo-elastic platform to simulate the aerodynamic heating of the panel. Unlike the previous cylinder application, the panel deformations in this case has a significant effect on the flow field.

3.2.2.1 *An Overview of Wind Tunnel Experiment for the Aerodynamically Heated Panel*

A schematic of a proposed experiment that could be used to validate the flow/thermal/structural analysis as presented in reference [26] is shown in Figure 3-25. Two cases for this problem are considered. In the first case, the panel is supported by immovable supports on the bottom corners, and the panel deforms into a convex shape as shown in Figure 3-25. In the second case, the panel is supported by immovable supports at the top corners, and the panel deforms into a concave shape as shown in Figure 3-25. The computed results for this case are compared against the numerical and analytical solutions from reference [26].
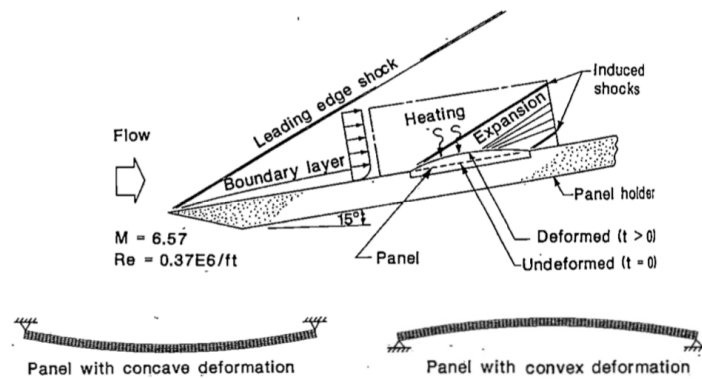
Figure 3-25 Schematic diagram of the experiment that can be used to validate the flow/thermal/structural analysis of the aerodynamically heated panel reproduced from reference [26].

3.2.2.2 Summary of the Applied Numerical Boundary Conditions for the Aerodynamically Heated Panel

The boundary conditions applied to the coupled problem are summarized in Figure 3-26. The top surface of the panel, which is the fluid/structure interface, has a surface heat flux applied on the structure side, and an applied temperature enforced from the structure side on to the fluid side. The sides of the panel are considered isothermal, with an applied temperature of 530*R*. The bottom surface of the panel is insulated. The panel case is run with two types of structural boundary conditions. In the first case, the panel is fixed on the left and right edges of the bottom surface, and in the second case the panel is fixed on the left and right edges of the top surface [25-27]. Numerical results for both cases are presented in this work.

The fluid mesh used for this study has 2,474,940 nodes, with 4,725,000 prism elements. The fluid mesh has a wall spacing of 6×10^{-6}, which gives a y^+ of less than one along the panel surface. The structure mesh used in this coupled simulation has 3,216 nodes, with 1,995 hexahedral elements.
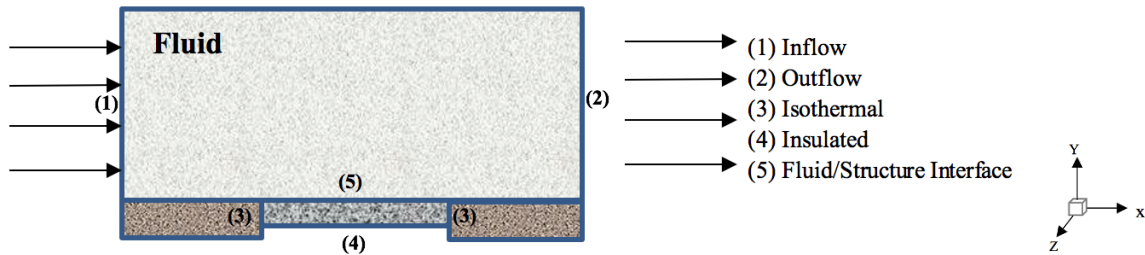
Figure 3-26 Applied boundary conditions for the aero-thermo-elastic problem of heated panel.

The initial free-stream flow parameters for this case are described in Table 3-14. It should be mentioned here that based on the information available in the literature there are two possible flow boundary conditions that can be applied: either we apply the before-shock Mach number 6.57, or the after-shock Mach number of 4.24 with associated post shock conditions. We decided to apply the before-shock Mach number as can be seen in Table 3-14. Hence, we simulated the flow through the oblique shock in order to obtain the desired boundary layer profile. However, reference [26] does not include any information about the exact length of the front panel holder required to create the precise boundary layer profile. We assumed it to be 5 inches, which later from the results was found to be too small of a value. Due to these reasons the solutions presented in this work are only compared qualitatively with reference [26].

Table 3-14 Initial free-stream conditions for the coupled flow over an aerodynamically heated panel.

Free-stream conditions	Value
Free-stream Mach number (Ma_∞)	6.57 (dimensionless)
Wall temperature (T_w)	530 R
Free-stream Reynolds number (Re_∞)	0.37×10^6 1/ft
Free-stream temperature (T_∞)	530 K
Free-stream velocity (U_∞)	6612.3 ft/s
Free-stream pressure (P_∞)	0.0971 psi

Since the flow field reaches equilibrium much faster than the thermal response of the panel structure, the coupled problem is again solved as a steady-state problem on the fluid side and as a transient problem on the structural side. The time step for the thermal solver is taken as 5*s*. Thus, it takes six coupled cycles between the fluid and structure solvers to reach the transient solution at thirty seconds.

The simulations were performed on the Cheyenne supercomputer at NCAR-Wyoming Supercomputing Center (NWSC). The computational cost of the coupled analysis problem for the panel cases presented in this work is approximately 18 minutes of wall-clock time on 320 cores. For the panel problems the flow is converged up to more than four orders of magnitude, and the structure problem up to machine precision (since it uses a direct method).

3.2.2.3 *Results for the Aerodynamically Heated Panel with Convex Deformation*

In this section, numerical results from the aero-thermo-elastic analysis of the panel with the convex deformation are presented. The interaction between the panel deformation and the flow density distributions at t = 30*s* for the convex panel is shown in Figure 3-27, which plots computed values of density non-dimensionalized by the freestream density. Although, the test cases are 2D in nature, the calculations are done fully in 3D. Hence, we have plotted the solution with a slight perspective to show the full computational domain. The figure clearly shows the development of a shock originating from the left support on the windward side. The density of the fluid increases through this shock at first but then decreases as the flow expands over the convex panel. A recompression shock is developed as the flow is turned by the deformed panel near the right side. The boundary layer thickness also changes because of the panel deformation. These results agree well qualitatively with the computational solutions presented in reference [26].
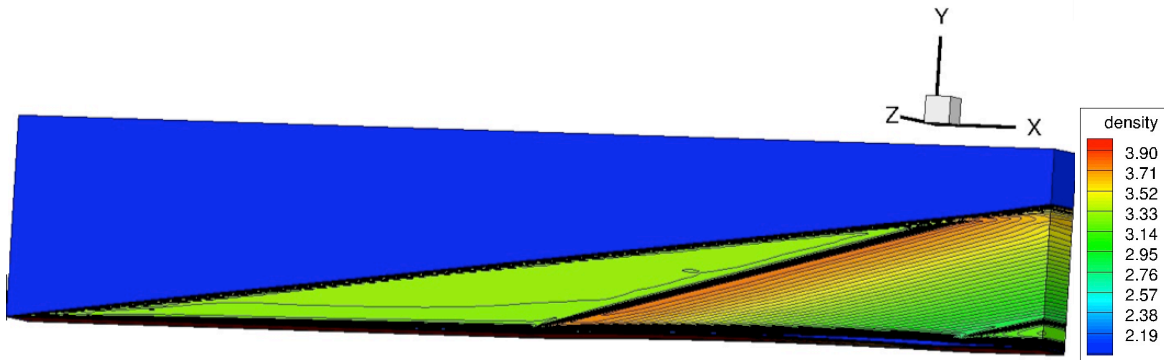
Figure 3-27 Flow density distributions at t = 30s, for the panel with convex deformation.

The evolution of the temperature at the fluid/structure interface at t = 0, 10, 20, 30s is presented in Figure 3-28 for the panel with the convex deformation. The evolution of the heating rate distribution for the panel with convex deformation is presented in Figure 3-29. from t = 0s, to t = 30s. The overall decrease of the heating rate is due to the rise in the panel temperature shown in Figure 3-28. As the temperature of the panel rises, temperature gradient at the fluid/structure interface decreases, which in turn produces a lower heating rate
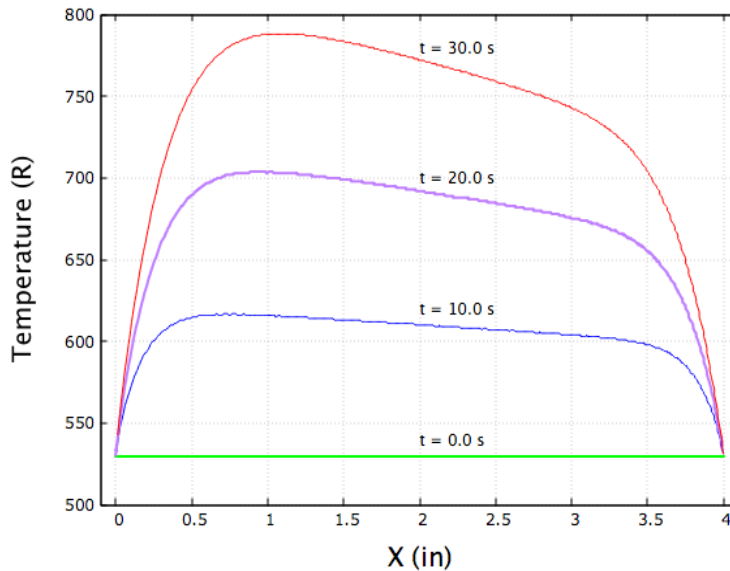
Figure 3-28 Evolution of the temperature distribution at the fluid/structure interface for the panel with convex deformation at t = 0, 10, 20, 30s.
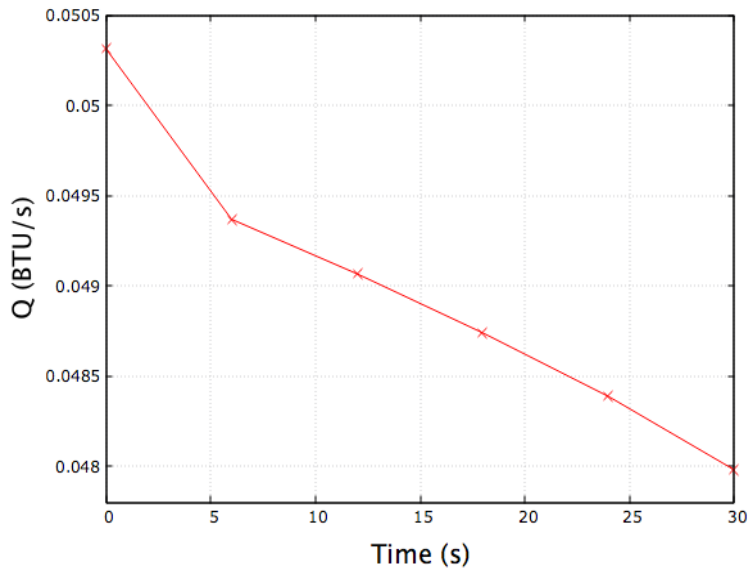
Figure 3-29 Evolution of heating rate distribution for panel with convex deformation from t = 0*s* to t = 30*s*.

The results for the temperature and maximum deformations for the convex panel case from the structural solver are shown in Table 3-15 and Table 3-16, respectively. The analytical solutions for the temperature and deformation are calculated from Eq. (3-14) and Eq. (3-15) presented earlier. The computed results are very close to the analytical solutions. As explained previously, the computed results differ from the analytical solutions since the analytical equations used are approximate solutions. The computed results from reference [26] also have small variation with respect to the analytical solutions as shown in Table 3-15 and Table 3-16.

It can be seen from Table 3-15 that the computed temperature values are slightly higher than the results from reference [26]. This is due to the shorter length of the upstream panel holder where the boundary layer develops, which was not specified in reference [26]. This in turn results in higher heat transfer rates. The short length of the front panel holder is also the reason for the corresponding higher deflections we have obtained compared to reference [26].

Table 3-15 Convex panel temperature solution *T (l/2, t)* in Rankine.

Time(s)	Coupled computational solution	Analytical solution	Computational solutions from reference [26]
10	615.58	606.22	595
20	691.47	685.31	650
30	772.859	767.28	705

Table 3-16   Convex panel deformation *v (l/2, t)* in inches.

Time(s)	Coupled computational solution	Analytical solution	Computational solutions from reference [26]
10	0.0126	0.0127	0.0133
20	0.0252	0.0234	0.0239
30	0.0369	0.0336	0.0327

3.2.2.4   *Results for the Aerodynamically Heated Panel with Concave Deformation*

In this section, numerical results from the aero-thermo-elastic analysis of a heated panel case with concave deformation is presented. The flow density distribution at $t = 30s$ for the panel with concave deformation is shown in Figure 3-30 which compares well qualitatively with the solutions in reference [26]. Hence, we have plotted the solution with a slight perspective to show the full computational domain. Figure 3-30 plots computed values of density non-dimensionalized by the free stream density. For this case an expansion occurs as the flow encounters the left support. This time the flow density decreases through the expansion but starts to increase as the flow is being turned by the concave panel. A second expansion fan emanates from the downwind panel support as the flow is turned back to the horizontal direction.
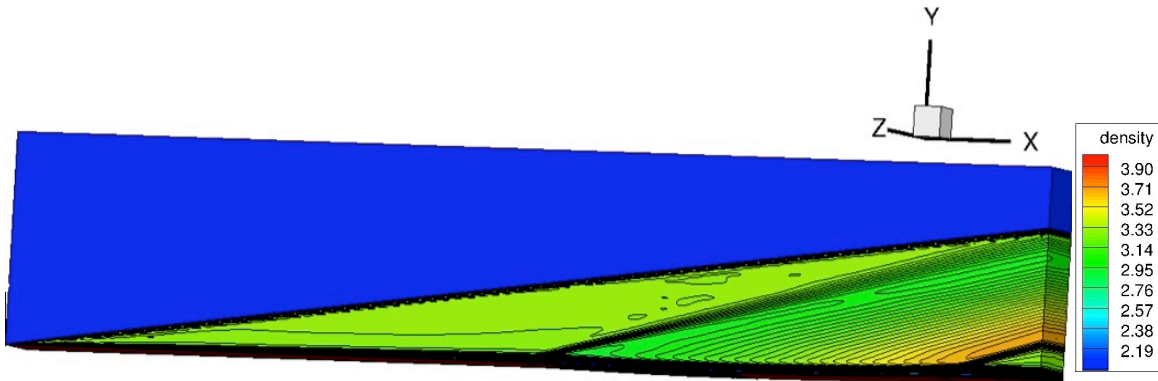
Figure 3-30 Flow density distributions at $t = 30s$, for the panel with concave deformation.

The evolution of temperature at the fluid/structure interface at $t = 0s$ to $t = 30s$ is presented in Figure 3-31 for the panel with the concave deformation. The evolution of the heating rate distribution from $t = 0s$ to $t = 30s$ for the concave case is shown in Figure 3-32. For the concave case, we again have an overall drop in the heating rate due to the rise of the panel temperature as time passes.
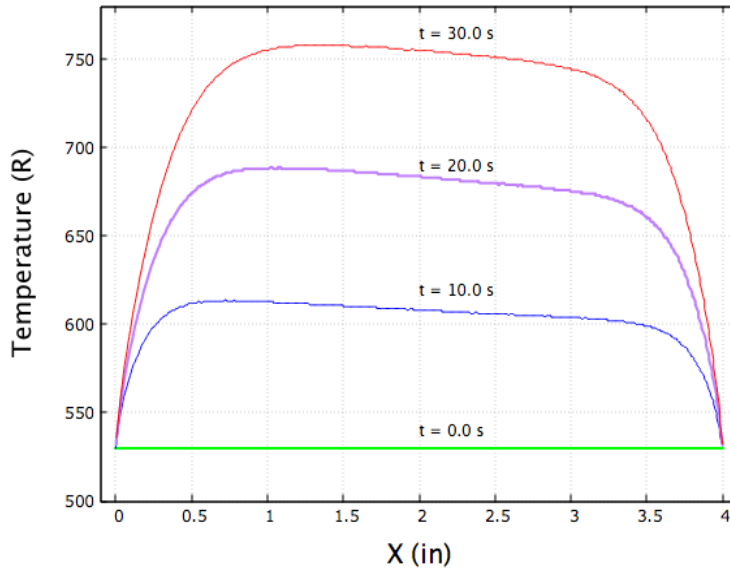
Figure 3-31 Evolution of the temperature distribution at the fluid/structure interface for the panel with concave deformation at t = 0, 10, 20, 30*s*.
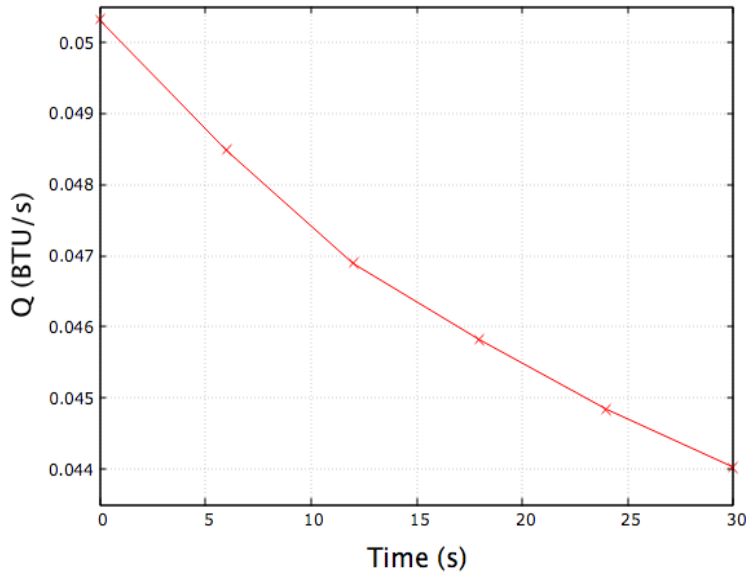
Figure 3-32 Evolution of heating rate distribution for panel with concave deformation from t = 0*s* to t = 30*s*.

The results for the temperature and maximum deformations for the concave panel case from the structural solver are shown in Table 3-17 and Table 3-18 respectively. The analytical solutions for the temperature and deformation are calculated from Eq. (3-14), Eq. (3-15) presented earlier. Again, the computed results are very close to the analytical solutions but not identical to the approximations and assumptions made in deriving the analytical solutions. The

computed value for the panel deformation at t = 30*s* from reference [26] also has small variation with respect to the analytical solutions as shown in Table 3-18. The discrepancies in the values of the heating rate and deflection between our results and reference [26] are due to the shorter length of the front panel holder we have used in our simulations and which was not specified reference [26].

Table 3-17   Concave panel temperature solution *T (l/2, t)* in Rankine.

Time(s)	Coupled computational solution	Analytical solution
10	608.51	606.22
20	687.22	685.31
30	758.14	767.28

Table 3-18 Concave panel deformation *v (l/2, t)* in inches.

Time(s)	Coupled computational solution	Analytical solution	Computational solutions From reference [26]
10	- 0.0121	- 0.0127	
20	- 0.0238	- 0.0234	
30	- 0.0345	- 0.0336	- 0.031

These two heated panel cases demonstrate the importance of aero-thermo-elastic coupling. Even though very small deformations occurred in the panel, the flow solution is altered significantly. The developed aero-thermo-elastic analysis capability is able to capture the effects of the deformation on the flow quite well.

3.3 Summary

This chapter has been dedicated to showing results for the computational framework used in this work. First, the thermal and thermo-elastic analysis capabilities of the structural solver were validated. Next, results were presented for the coupled aero-thermal and aero-thermo-elastic analysis capabilities of the platform. The developed aero-thermo-elastic analysis capability was able to capture the physics accurately when applied to example cases.

4 COUPLED AERO-THERMO-ELASTIC DESIGN OPTIMIZATION

This chapter starts by looking at the available numerical optimization methods, focusing on what is used in the aeronautical field. This is followed by presenting the multi-disciplinary sensitivity analysis formulations used and implemented in this work. First, the tangent and adjoint formulations for thermo-elastic sensitivity analysis as used in AStrO will be presented. Next, a description of the coupled tangent and adjoint sensitivities for the aero-thermo-elastic platform is provided.

4.1 Numerical Optimization

Numerical optimization algorithms can be put in two general categories: global or evolutionary methods, and local or gradient-based methods. The global- based algorithms use a set of agents within the search space. These agents will coordinate themselves in order to find the global optimum. The biggest problem with using global search algorithms is the cost, which can be as much as two orders of magnitude more expensive in comparison to gradient-based systems. This makes them impractical for high-fidelity and computationally-intensive models. Attempts have been made to reduce the cost of evolutionary algorithms by using them in combination with metamodeling techniques. However, as more disciplines are included in the design process, the number of design variables increases, making evolutionary methods not suitable for large-scale multi-disciplinary design problems. Another disadvantage of global-based methods is that handling constraints on a solution is also more difficult in an agent-based algorithm [100, 101].

On the other hand, gradient-based algorithms use some function of the gradient to construct a search procedure. The optimization process terminates when gradients of the objectives become zero, which means some optimum is reached. The downfall with this is that the termination could occur at any local optimum, and not necessarily at the global optimum. However, one advantage of the gradient-based methods is that constraints on the solution can be easily applied. Also, these types of methods require significantly fewer function evaluations, provided that the gradient of the objective function is computed with an efficient method. This makes gradient-based optimization methods the better choice when dealing with large-scale, high-fidelity, multi-disciplinary design problems [100, 101]. Most optimization problems in the field of aerodynamics are solved using gradient-based methods. Therefore, in the following pages, we take a closer look at gradient-based optimization and the different methods available.

4.1.1 Gradient-Based Optimization

The extremum of a function can be found by using the gradient/slope. This is done by moving in the direction of the negative or positive gradient/slope depending on whether we are looking for a minimum or a maximum. The gradient can also be seen as the sensitivity of the function output to the independent parameters. Hence, these gradients are referred to as sensitivity derivatives [102].

Gradient-based optimizations require the gradients of the objective function and constraints with respect to the design variables. The gradient or sensitivity derivative allow us to change the design variable in order to improve the objective function without violating the constraints. In aerodynamic design, the objective function is usually a value such as lift, drag, momentum, or surface temperature. Design parameters are usually variables that can control the shape of the geometry, or material properties of the structure [46].

In the following section, we will take a closer look at various methods used for sensitivity analysis or gradient calculation.

4.1.1.1 *Finite-Difference Method*

The finite-difference method is one of the simplest methods for computing the sensitivity derivatives. For this approach, an approximate expression for the derivative is obtained by expanding the flux using a Taylor series. For the purpose of this discussion a forward difference is used as given below:

$$F(Q_0+\epsilon) = F(Q_0)+\epsilon \left(\frac{\partial F}{\partial Q}\right)_{Q_0} + \frac{\epsilon^2}{2}\left(\frac{\partial^2 F}{\partial Q^2}\right)_{Q_0} + \frac{\epsilon^3}{6}\left(\frac{\partial^3 F}{\partial Q^3}\right)_{Q_0} + \frac{\epsilon^4}{24}\left(\frac{\partial^4 F}{\partial Q^4}\right)_{Q_0} + \cdots \ldots .. \quad (4\text{-}1)$$

where ϵ, is the step size. Using the above expansion of the Taylor series, an expression for the derivative can be obtained as follows:

$$\left(\frac{\partial F}{\partial Q}\right)_{Q_0} = \frac{F(Q_0+\epsilon)-F(Q_0)}{\epsilon} + O(\epsilon) \quad (4\text{-}2)$$

$O(\epsilon)$ is the truncation error and it consists of the terms in the Taylor series that have an order higher than ϵ which will be ignored in the calculations. Although the finite-difference method is very simple, it is prone to errors associated with choice of step size [102]. Another problem with this approach is that it is computationally expensive, since we need to run two analysis cycles to calculate the sensitivity with respect to each design variable. Therefore, this method is unsuitable for complex cases with many design variables [52].

4.1.1.2 *Complex-Step Method*

This method is very similar to the finite-difference method. However, in this case the perturbation is introduced to the imaginary part of the input. This is demonstrated more clearly in the Taylor series expansion below [103, 104]:

$$f(x + ih) = f(x) + ihf'(x) - \frac{h^2}{2}f''(x) + \cdots \tag{4-3}$$

from which the derivative $f'(x)$ can be easily determined as:

$$f'(x) = \frac{Im[f(x+ih)]}{h} \tag{4-4}$$

As seen above, similar to the finite-difference method, the complex-step method also requires a step size. However, the complex-step method results in derivatives with higher numerical accuracy. This is due to the fact that we can choose the step size quite small while still being able to avoid round-off errors. The main disadvantage of the complex-step method is the large increase in runtime required when using complex arguments [103, 104].

4.1.1.3 *Analytical Methods*

In analytical differentiation methods, the sensitivity derivatives are found by differentiating the governing equations directly. Calculating the sensitivities analytically provides us with much better accuracy than the finite-difference. In the following sub-sections, we will look at some of the most commonly used analytical methods: automatic differentiation, direct/tangent, and adjoint methods.

4.1.1.3.1 Automatic Differentiation Method

This method provides an automatic tool to calculate an accurate derivative of the cost function based on the chain rule differentiation principle [102, 104]. This method requires the operator overloading of elementary derivative rules for addition, subtraction, multiplication, division, and etc. By applying the chain rule repeatedly to these operations, derivatives of arbitrary order can be computed automatically and accurately [105]. This procedure will result in a new code that provides the function value as well as the derivative of any function in the code with respect to the defined design variables. Although the derivatives are accurate, this method also suffers from high computational cost.

4.1.1.3.2 Tangent and Adjoint Methods

When calculating the sensitivity derivatives with the tangent or the adjoint methods an additional level of simulation referred to as the sensitivity analysis, is required [102]. The selection of the appropriate sensitivity analysis formulation (tangent or adjoint) depends on the

design problem. For the tangent method the computational work scales with the number of design variables. On the other hand, the adjoint method, enables the calculation of sensitivity derivates at a cost independent of the number of design variables. For this reason, the adjoint method is a very powerful tool when dealing with optimization problems with large number of design variables. It should be mentioned that the adjoint method scales with the number of objective functions and constraints. Therefore, if dealing with large number of objectives/constraints and small number of design variables, the tangent method would be the better choice. Using either the tangent or adjoint method results in highly accurate derivatives. In addition, these methods of calculating sensitivities require less computational cost than any of the previously mentioned methods.

The first application of adjoint equations to fluid dynamics design was by Pironneau [106]. However, it was Jameson who pioneered the use of adjoint equations in the field of aeronautical computational fluid dynamics. Jameson applied the adjoint method to potential flow, Euler and Navier-stokes equations [7, 8, 107]. In recent years, adjoint equations have become very popular in the field of aerodynamic design. The adjoint problem can be solved by either the continuous or the discrete approach. In the continuous adjoint approach, the governing equations are first linearized and then discretized, while in the discrete adjoint approach the same steps are performed in reverse order.

Both the desecrate and continuous adjoint approaches have their advantages. Although the continuous approach provides more flexibility in the discretization stage, it makes the determination of boundary conditions challenging. The discrete adjoint follows the discretization of the governing equations, which makes this approach very straight-forward. This is easily applied to the boundaries as well. In addition, the discrete approach provides exact sensitivities for the discretized governing problem. This is advantageous, since in CFD optimization the goal is to discretely evaluate the objective function. Newman et al. [102] has a comprehensive review of the research on both continuous and discrete adjoint methods. In this work, we have used the discrete approach to calculate the sensitivities due to the aforementioned advantages.

4.1.1.3.2.1 Tangent and Adjoint Sensitivity Analysis Formulation
In this section, a formal derivation of the tangent and the adjoint methods for a generic problem will be presented. In the following it can be seen that the derivation of the discrete adjoint equations can be done using both the chain-rule differentiation as well as using Lagrange multipliers.

Let us consider a simulation which takes a set of input parameters D and produces a set of output quantities of interest L based on a computed state U, where U is a field vector. The functional dependence can be written as:

$$L = L(U(D), D) \tag{4-5}$$

where U depends implicitly on the inputs D, since it is obtained as the solution of the residual equation:

$$R(U(D), D) = 0 \tag{4-6}$$

In order to compute the derivate of L with respect to D, the chain rule is used as follows:

$$\frac{dL}{dD} = \frac{\partial L}{\partial D} + \frac{\partial L}{\partial U}\frac{\partial U}{\partial D} \tag{4-7}$$

where $\frac{\partial U}{\partial D}$ represents the flow field sensitivity to the input parameter D. This sensitivity can be obtained by differentiating the residual equation or the constraint $R(U(D), D) = 0$ as follows:

$$\frac{\partial R}{\partial U}\frac{\partial U}{\partial D} = -\frac{\partial R}{\partial D} \tag{4-8}$$

By substituting this into Eq. (4-7) we obtain:

$$\frac{dL}{dD} = \frac{\partial L}{\partial D} - \frac{\partial L}{\partial U}\left[\frac{\partial R}{\partial U}\right]^{-1}\frac{\partial R}{\partial D} \tag{4-9}$$

Therefore, the tangent linearization can be written as:

$$\begin{cases} \dfrac{\partial R}{\partial U}\dfrac{\partial U}{\partial D} = -\dfrac{\partial R}{\partial D} \\[2ex] \dfrac{dL}{dD} = \dfrac{\partial L}{\partial D} + \dfrac{\partial L}{\partial U}\dfrac{\partial U}{\partial D} \end{cases} \tag{4-10}$$

The corresponding adjoint procedure can be summarized as:

$$\begin{cases} \left[\dfrac{\partial R}{\partial U}\right]^{T}\Lambda = -\dfrac{\partial L}{\partial U}^{T} \\[2ex] \dfrac{dL}{dD} = \dfrac{\partial L}{\partial D} + \Lambda^{T}\dfrac{\partial R}{\partial D} \end{cases} \tag{4-11}$$

Looking at Eq. (4-10) and Eq.(4-11), we can see that most of the computational expense for both methods occurs in the solution of the first equation. For the tangent method, a new sensitivity solution is required for each input parameter D. The adjoint method requires a new adjoint solution for each objective function L. Hence, it can be concluded that the tangent approach is more advantageous for cases with a single input and multiple objectives, while the adjoint approach is best for cases with a single objective and multiple input parameters [108].

As mentioned previously, the adjoint formulation can also be derived using Lagrange multipliers. In this approach, the residual equation $R(U(D), D) = 0$ is treated as a constraint, and an augmented functional J is formed as:

$$J(U(D), D) = L(U(D), D) + \Lambda^T R(U(D), D) \tag{4-12}$$

In the above equation, Λ is introduced as the Lagrange multiplier. The Lagrange multiplier can be chosen arbitrarily, since it multiplies with the vanishing residual constraint. Then, taking the derivatives of J with respect to D, we obtain:

$$\frac{dJ}{dD} = \frac{dL}{dD} + \frac{\partial L}{\partial U}\frac{\partial U}{\partial D} + \Lambda^T(\frac{\partial R}{\partial D} + \frac{\partial R}{\partial U}\frac{\partial U}{\partial D}) \tag{4-13}$$

By factoring out the flow sensitivity $\frac{\partial U}{\partial D}$, the above equation becomes:

$$\frac{dJ}{dD} = \frac{dL}{dD} + \Lambda^T\frac{\partial R}{\partial D} + (\frac{\partial L}{\partial U} + \Lambda^T\frac{\partial R}{\partial U})\frac{\partial U}{\partial D} \tag{4-14}$$

Λ is chosen such that the last term in the above equation vanishes:

$$\frac{\partial L}{\partial U} + \Lambda^T\frac{\partial R}{\partial U} = 0 \tag{4-15}$$

Hence, we recover the same expression as before for the final sensitivity:

$$\frac{dJ}{dD} = \frac{dL}{dD} + \Lambda^T\frac{\partial R}{\partial D} \tag{4-16}$$

4.1.1.3.2.2 Verification of Tangent and Adjoint Sensitivities

One of the advantages of discrete versus continuous adjoint implementations is that the sensitivities produced by the discrete adjoint technique can be verified exactly for correctness. This is due to the fact that the sensitivities produced by the discrete adjoint approach correspond to the exact sensitivities of the simulation code. Therefore, tangent and adjoint sensitivities can be checked against sensitivities obtained from the finite-difference or complex-step methods. In theory, it is possible to verify tangent and adjoint-based gradients using the complex-step method to machine precision. However, since the finite-difference method introduces roundoff errors, often only an agreement of up to several significant figures can be achieved between the sensitivities obtained from the finite-difference method and the tangent/adjoint method.

A common practice is to first validate the tangent method against the complex-step or finite-difference method. This is because the tangent method is more intuitive to construct since it follows the analysis code very closely. This means that we can track down any issues in the linearization faster as well. Once the tangent sensitivities have been verified, the adjoint

sensitivities can be validated using the duality relation [109] against the tangent method. For complex multi-disciplinary simulations, verification can be carried out one discipline at a time, building up to ultimately include all disciplines.

Here, we will try to briefly present the principle of duality. Let us consider a primal operation of a matrix operating on a vector and the transposed dual of the same operation as shown below:

$$\begin{cases} [A]\xi = f \\ [A]^T \eta = g \end{cases} \tag{4-17}$$

Where the vectors f and g are arbitrary inputs. The principle of duality establishes the following equivalence between the primal and dual operations :

$$\xi^T g = f^T \eta \tag{4-18}$$

Hence, by using the arbitrary input vectors f and g in Eq. (4-17), we can determine their corresponding outputs ξ and η. From there we determine if the solutions satisfy Eq.(4-18). If the operations are transposed correctly, a match to machine precision is observed in Eq.(4-18). Although duality using a particular set of input vectors is a necessary test to ensure accuracy of the transpose operation, it is by no means sufficient. As a consequence, the duality test needs to be performed using several random input vectors in order to validate the operation.

4.2 Thermo-Elastic Sensitivity Analysis Formulation

In this section, we look at both the static and transient thermo-elastic sensitivity analysis formulation. First, general formulations are presented and later these formulations are updated considering the specifics of AStrO.

4.2.1.1 *Static Thermo-Elastic Sensitivity Analysis Formulation*

Again, we start by looking at the sensitivities of the objective with respect to the design parameters. Consider an objective function such as L:

$$L = L(D, u_T(D), u_S(D)) \tag{4-19}$$

As shown in Eq. (4-19) above, in addition to an explicit dependence on the design inputs D, there exists an implicit dependence through the state variables u_T, u_S, coming from the thermal and structural disciplines, respectively. In all the following equations the subscripts T, and S refer to the thermal and structural disciplines, respectively. Using the chain rule, the sensitivity of the objective function with respect to the design variables D can be expressed as:

$$\frac{dL}{dD} = \frac{\partial L}{\partial D} + \frac{\partial L}{\partial u_T}\frac{\partial u_T}{\partial D} + \frac{\partial L}{\partial u_S}\frac{\partial u_S}{\partial D} \tag{4-20}$$

The above equation can also be written in matrix from as follows:

$$\frac{dL}{dD} = \frac{\partial L}{\partial D} + \begin{bmatrix} \frac{\partial L}{\partial u_T} & \frac{\partial L}{\partial u_S} \end{bmatrix} \begin{bmatrix} \frac{\partial u_T}{\partial D} \\ \frac{\partial u_S}{\partial D} \end{bmatrix} \tag{4-21}$$

The linearization of the objective function with respect to the disciplinary state variables can easily be computed. However, the linearization of the disciplinary state variables with respect to the design variables are unknown quantities at this point, and an expression for their evaluation must be determined. The governing nonlinear equations of each discipline in residual form are:

$$R_T(D, u_T, u_S) = 0 \tag{4-22}$$

$$R_S(D, u_T, u_S) = 0 \tag{4-23}$$

As can be seen from Eq. (4-22) and Eq. (4-23) above, the residual equation from each discipline not only depends on its own state variables but also on the state variables of the other discipline. This is because of the assumption of coupling between the disciplines. Since we are assuming a general case here, the residual equation will also have dependence on the design variables D. Differentiating the disciplinary residual equations with respect to the set of design variables D yields:

$$\frac{\partial R_T}{\partial D} + \frac{\partial R_T}{\partial u_T}\frac{\partial u_T}{\partial D} + \frac{\partial R_T}{\partial u_S}\frac{\partial u_S}{\partial D} = 0 \tag{4-24}$$

$$\frac{\partial R_S}{\partial D} + \frac{\partial R_S}{\partial u_T}\frac{\partial u_T}{\partial D} + \frac{\partial R_S}{\partial u_S}\frac{\partial u_S}{\partial D} = 0 \tag{4-25}$$

As mentioned previously, AStrO assumes a one-way dependence of elastic displacement on temperature distribution for thermo-elastic analysis. This means that Eq. (4-24) can be further simplified as follows:

$$\frac{\partial R_T}{\partial u_S} = 0 => \frac{\partial R_T}{\partial D} + \frac{\partial R_T}{\partial u_T}\frac{\partial u_T}{\partial D} = 0 \tag{4-26}$$

Equations (4-24), and (4-26) can be combined into matrix form as shown in Eq. (4-27).

$$\begin{bmatrix} \frac{\partial R_T}{\partial u_T} & 0 \\ \frac{\partial R_S}{\partial u_T} & \frac{\partial R_S}{\partial u_S} \end{bmatrix} \begin{bmatrix} \frac{\partial u_T}{\partial D} \\ \frac{\partial u_S}{\partial D} \end{bmatrix} = \begin{bmatrix} -\frac{\partial R_T}{\partial D} \\ -\frac{\partial R_S}{\partial D} \end{bmatrix} \tag{4-27}$$

Solving the above set of equations provides us with the state variable sensitivities with respect to the design variables. Now we can substitute this into Eq. (4-20) and solve for the complete sensitivity vector $\frac{dL}{dD}$.

When calculating sensitivities with the above (tangent) method, the linearization scales directly with the number of design variables. Since the number of design variables is usually large, the adjoint procedure is used as a more efficient way of calculating these sensitivities. The adjoint method is the more efficient method, since the cost of this method is independent of the number of design parameters [50] as shown below.

For the adjoint formulation we require the transpose of the forward linearization as shown below:

$$\frac{dL}{dD}^T = \frac{\partial L}{\partial D}^T + \begin{bmatrix} \frac{\partial u_T}{\partial D}^T & \frac{\partial u_S}{\partial D}^T \end{bmatrix} \begin{bmatrix} \frac{\partial L}{\partial u_T}^T \\ \frac{\partial L}{\partial u_S}^T \end{bmatrix} \tag{4-28}$$

In the adjoint method the computation of the state variable sensitivities is avoided. The following expression is obtained for the state variable sensitivities by transposing and rearranging Eq. (4-27):

$$\begin{bmatrix} \frac{\partial u_T}{\partial D}^T & \frac{\partial u_S}{\partial D}^T \end{bmatrix} = \begin{bmatrix} -\frac{\partial R_T}{\partial D}^T & -\frac{\partial R_S}{\partial D}^T \end{bmatrix} \begin{bmatrix} \frac{\partial R_T}{\partial u_T}^T & \frac{\partial R_S}{\partial u_T}^T \\ 0 & \frac{\partial R_S}{\partial u_S}^T \end{bmatrix}^{-1} \tag{4-29}$$

Substituting the above into Eq. (4-28), yields:

$$\frac{dL}{dD}^T = \frac{\partial L}{\partial D}^T + \begin{bmatrix} -\frac{\partial R_T}{\partial D}^T & -\frac{\partial R_S}{\partial D}^T \end{bmatrix} \begin{bmatrix} \frac{\partial R_T}{\partial u_T}^T & \frac{\partial R_S}{\partial u_T}^T \\ 0 & \frac{\partial R_S}{\partial u_S}^T \end{bmatrix}^{-1} \begin{bmatrix} \frac{\partial L}{\partial u_T}^T \\ \frac{\partial L}{\partial u_S}^T \end{bmatrix} \tag{4-30}$$

The adjoint variable for each discipline is defined as:

$$\begin{bmatrix} \Lambda_T \\ \Lambda_S \end{bmatrix} = \begin{bmatrix} \frac{\partial R_T}{\partial u_T}^T & \frac{\partial R_S}{\partial u_T}^T \\ 0 & \frac{\partial R_S}{\partial u_S}^T \end{bmatrix}^{-1} \begin{bmatrix} \frac{\partial L}{\partial u_T}^T \\ \frac{\partial L}{\partial u_S}^T \end{bmatrix} \tag{4-31}$$

The coupled linear adjoint system of equations in AStrO becomes:

$$\begin{bmatrix} \dfrac{\partial R_T}{\partial u_T}^T & \dfrac{\partial R_S}{\partial u_T}^T \\ 0 & \dfrac{\partial R_S}{\partial u_S}^T \end{bmatrix} \begin{bmatrix} \Lambda_T \\ \Lambda_S \end{bmatrix} = \begin{bmatrix} \dfrac{\partial L}{\partial u_T}^T \\ \dfrac{\partial L}{\partial u_S}^T \end{bmatrix} \tag{4-32}$$

Once the vector of adjoint variables for each discipline is available, it may be substituted into the total sensitivity equation as:

$$\frac{dL^T}{dD} = \frac{\partial L^T}{\partial D} + \begin{bmatrix} -\dfrac{\partial R_T}{\partial D}^T & -\dfrac{\partial R_S}{\partial D}^T \end{bmatrix} \begin{bmatrix} \Lambda_T \\ \Lambda_S \end{bmatrix} \tag{4-33}$$

It is clear from the above equations that the number of design variables only affects the matrix-vector products at the end of the computation process [46]. This is why the adjoint method is more efficient in calculating sensitivities than the tangent method. In this work, both the tangent and the adjoint methods are implemented and compared.

When dealing with thermo-elastic sensitivity analysis, we also need to transfer sensitivities between the thermal and structural solvers. The transfer of information performed by AStrO during a sensitivity analysis is summarized in in Figure 4-1. The one-way dependence between the elastic displacement on temperature distribution is clear in this figure. More details regarding the sensitivity analysis formulations and implementations in AStrO are given in reference [42].
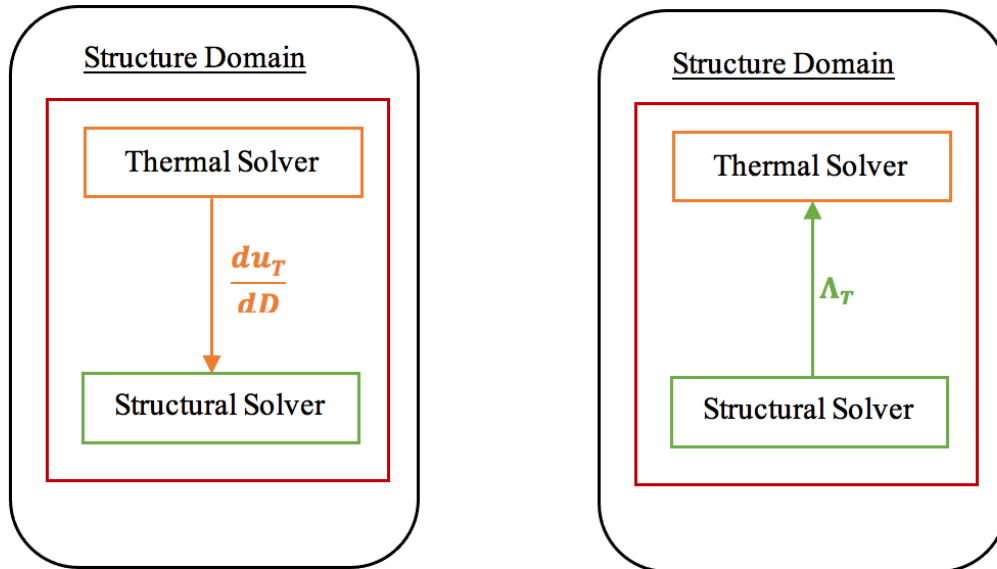
Figure 4-1 Flow of information for the thermo-elastic tangent (on the left) and adjoint (on the right) sensitivity analysis process in AStrO.

4.2.1.2 *Transient Thermo-Elastic Sensitivity Analysis Formulation*

For the transient simulation, the Jacobian matrices $\frac{\partial R}{\partial u}$, span in both the spatial and temporal domains. Since time is purely hyperbolic in nature, the discrete residual R at any arbitrary time step n can only depend on quantities at time indices $\leq n$. Therefore, the discrete time expansion of any Jacobian matrix for a temporal domain consisting of n time steps results in a block lower triangular matrix as shown in Eq. (4-34) below. In this form, each of the blocks is a matrix spanning the spatial domain. The matrix is lower triangular with one non-zero block off-diagonal resulting from the dependence of the Newmark-Beta time stepping scheme on only the previous time level.

$$\frac{\partial R}{\partial u} = \begin{bmatrix} \left[\frac{\partial R^0}{\partial u^0}\right] & 0 & 0 & 0 & \cdots \\ \left[\frac{\partial R^1}{\partial u^0}\right] & \left[\frac{\partial R^1}{\partial u^1}\right] & 0 & 0 & \cdots \\ 0 & \left[\frac{\partial R^2}{\partial u^1}\right] & \left[\frac{\partial R^2}{\partial u^2}\right] & 0 & \cdots \\ 0 & 0 & \left[\frac{\partial R^3}{\partial u^2}\right] & \left[\frac{\partial R^3}{\partial u^3}\right] & \cdots \\ \vdots & \vdots & \vdots & \vdots & \ddots \end{bmatrix} \tag{4-34}$$

Now, for the thermo-elastic problem, let us assume a temporal domain consisting of two time steps n and $n-1$. Hence, Eq. (4-27) can be rewritten using the discrete temporal expansion of the Jacobian matrices as:

$$\left[\begin{array}{cc|cc} \left[\frac{\partial R_T^{n-1}}{\partial u_T^{n-1}}\right] & 0 & \left[\frac{\partial R_T^{n-1}}{\partial u_S^{n-1}}\right] & 0 \\ \left[\frac{\partial R_T^n}{\partial u_T^{n-1}}\right] & \left[\frac{\partial R_T^n}{\partial u_T^n}\right] & \left[\frac{\partial R_T^n}{\partial u_S^{n-1}}\right] & \left[\frac{\partial R_T^n}{\partial u_S^n}\right] \\ \hline \left[\frac{\partial R_S^{n-1}}{\partial u_T^{n-1}}\right] & 0 & \left[\frac{\partial R_S^{n-1}}{\partial u_S^{n-1}}\right] & 0 \\ \left[\frac{\partial R_S^n}{\partial u_T^{n-1}}\right] & \left[\frac{\partial R_S^n}{\partial u_T^n}\right] & \left[\frac{\partial R_S^n}{\partial u_S^{n-1}}\right] & \left[\frac{\partial R_S^n}{\partial u_S^n}\right] \end{array}\right] \begin{bmatrix} \frac{\partial u_T^{n-1}}{\partial D} \\ \frac{\partial u_T^n}{\partial D} \\ \hline \frac{\partial u_S^{n-1}}{\partial D} \\ \frac{\partial u_S^n}{\partial D} \end{bmatrix} = \begin{bmatrix} -\frac{\partial R_T^{n-1}}{\partial D} \\ -\frac{\partial R_T^n}{\partial D} \\ \hline -\frac{\partial R_S^{n-1}}{\partial D} \\ -\frac{\partial R_S^n}{\partial D} \end{bmatrix} \tag{4-35}$$

The overall system can be represented as a block lower triangular matrix by swapping the rows and columns as shown in Eq. (4-36). The one-way dependence of elastic displacement on temperature distribution for thermo-elastic analysis in AStrO has been taken into account in Eq. (4-35). In this form, each diagonal block represents a single time step.

$$
\begin{bmatrix}
\left[\dfrac{\partial R_T^{n-1}}{\partial u_T^{n-1}}\right] & 0 & 0 & 0 \\[2ex]
\left[\dfrac{\partial R_S^{n-1}}{\partial u_T^{n-1}}\right] & \left[\dfrac{\partial R_S^{n-1}}{\partial u_S^{n-1}}\right] & 0 & 0 \\[3ex]
\hline
\left[\dfrac{\partial R_T^{n}}{\partial u_T^{n-1}}\right] & 0 & \left[\dfrac{\partial R_T^{n}}{\partial u_T^{n}}\right] & 0 \\[2ex]
\left[\dfrac{\partial R_S^{n}}{\partial u_T^{n-1}}\right] & \left[\dfrac{\partial R_S^{n}}{\partial u_S^{n-1}}\right] & \left[\dfrac{\partial R_S^{n}}{\partial u_T^{n}}\right] & \left[\dfrac{\partial R_S^{n}}{\partial u_S^{n}}\right]
\end{bmatrix}
\begin{bmatrix}
\dfrac{\partial u_T^{n-1}}{\partial D} \\[2ex]
\dfrac{\partial u_S^{n-1}}{\partial D} \\[2ex]
\hline
\dfrac{\partial u_T^{n}}{\partial D} \\[2ex]
\dfrac{\partial u_S^{n}}{\partial D}
\end{bmatrix}
=
\begin{bmatrix}
-\dfrac{\partial R_T^{n-1}}{\partial D} \\[2ex]
-\dfrac{\partial R_S^{n-1}}{\partial D} \\[2ex]
\hline
-\dfrac{\partial R_T^{n}}{\partial D} \\[2ex]
-\dfrac{\partial R_S^{n}}{\partial D}
\end{bmatrix}
\tag{4-36}
$$

For the simple case of a single design parameter D, this forms a block lower triangular linear system where the unknown state variable sensitivities and the right-hand-side form vectors rather than matrices. Thus, the system can be solved using forward substitution, i.e. a forward sweep in time beginning at time step $n - 1$, and progressing to time step n. At each time step, a fully coupled linear system is solved iteratively to obtain the sensitivity of the state variables at that time step to the single design parameter. For the case of multiple design inputs D, the forward sweep in time along with the coupled linear solution at each time step has to be performed for each parameter in order to construct the state variable sensitivity matrix for each discipline one column at a time. Once the state variable sensitivity matrices are available, they can be substituted into Eq. (4-21), where the inner product can be evaluated and the complete gradient vector $\dfrac{dL}{dD}$ becomes available [42, 46, 100, 110].

Following the same derivation as given above for the tangent linearization, again we assume a problem with two disciplines, and two time steps, n and $n - 1$. The adjoint system can be discretely expanded in time as:

$$
\begin{bmatrix}
\left[\dfrac{\partial R_T^{n-1}}{\partial u_T^{n-1}}\right]^T & \left[\dfrac{\partial R_T^{n}}{\partial u_T^{n-1}}\right]^T & \left[\dfrac{\partial R_S^{n-1}}{\partial u_T^{n-1}}\right]^T & \left[\dfrac{\partial R_S^{n}}{\partial u_T^{n-1}}\right]^T \\[2ex]
0 & \left[\dfrac{\partial R_T^{n}}{\partial u_T^{n}}\right]^T & 0 & \left[\dfrac{\partial R_S^{n}}{\partial u_T^{n}}\right]^T \\[3ex]
\hline
\left[\dfrac{\partial R_T^{n-1}}{\partial u_S^{n-1}}\right]^T & \left[\dfrac{\partial R_T^{n}}{\partial u_S^{n-1}}\right]^T & \left[\dfrac{\partial R_S^{n-1}}{\partial u_S^{n-1}}\right]^T & \left[\dfrac{\partial R_S^{n}}{\partial u_S^{n-1}}\right]^T \\[2ex]
0 & \left[\dfrac{\partial R_T^{n}}{\partial u_S^{n}}\right]^T & 0 & \left[\dfrac{\partial R_S^{n}}{\partial u_S^{n}}\right]^T
\end{bmatrix}
\begin{bmatrix}
\Lambda_T^{n-1} \\[2ex]
\Lambda_T^{n} \\[2ex]
\hline
\Lambda_S^{n-1} \\[2ex]
\Lambda_S^{n}
\end{bmatrix}
=
\begin{bmatrix}
\dfrac{\partial L}{\partial u_T^{n-1}}^T \\[2ex]
\dfrac{\partial L}{\partial u_T^{n}}^T \\[2ex]
\hline
\dfrac{\partial L}{\partial u_S^{n-1}}^T \\[2ex]
\dfrac{\partial L}{\partial u_S^{n}}^T
\end{bmatrix}
\tag{4-37}
$$

Eq. (4-37), can be rearranged into a block upper triangular form by swapping the rows and columns as shown below:

$$
\begin{bmatrix}
\left[\dfrac{\partial R_T^{n-1}}{\partial u_T^{n-1}}\right]^T & \left[\dfrac{\partial R_S^{n-1}}{\partial u_T^{n-1}}\right]^T & \left[\dfrac{\partial R_T^{n}}{\partial u_T^{n-1}}\right]^T & \left[\dfrac{\partial R_S^{n}}{\partial u_T^{n-1}}\right]^T \\[2ex]
0 & \left[\dfrac{\partial R_S^{n-1}}{\partial u_S^{n-1}}\right]^T & 0 & \left[\dfrac{\partial R_S^{n}}{\partial u_S^{n-1}}\right]^T \\[2ex]
\hline
0 & 0 & \left[\dfrac{\partial R_T^{n}}{\partial u_T^{n}}\right]^T & \left[\dfrac{\partial R_S^{n}}{\partial u_T^{n}}\right]^T \\[2ex]
0 & 0 & 0 & \left[\dfrac{\partial R_S^{n}}{\partial u_S^{n}}\right]^T
\end{bmatrix}
\begin{bmatrix}
\Lambda_T^{n-1} \\[1ex]
\Lambda_S^{n-1} \\[1ex]
\hline
\Lambda_T^{n} \\[1ex]
\Lambda_S^{n}
\end{bmatrix}
=
\begin{bmatrix}
\dfrac{\partial L}{\partial u_T^{n-1}}^T \\[2ex]
\dfrac{\partial L}{\partial u_S^{n-1}}^T \\[2ex]
\hline
\dfrac{\partial L}{\partial u_T^{n}}^T \\[2ex]
\dfrac{\partial L}{\partial u_S^{n}}^T
\end{bmatrix}
\tag{4-38}
$$

This system can be solved through back substitution, i.e. a backward sweep in time, where a coupled linear system is solved at time step n before progressing backward to time step $n-1$. At each time step, a coupled iterative linear solution is required in order to determine the vector of unknown disciplinary adjoint variables at that time step. Once the vector of disciplinary adjoint variables spanning the spatial and temporal domains is available, it may be substituted into the total sensitivity equation shown in Eq. (4-33). Again, the effect of the number of design inputs D has been confined to a series of matrix-vector products at the end of the computation. The elegance of the method lies in the fact that only a single backward sweep in time with coupled linear solutions at each time step is required in order to compute the total gradient, contrary to tangent linearization. In summary, the determination of the gradient vector involves a single forward integration in time to obtain the solution to the coupled unsteady analysis problem, and a single backward sweep in time to obtain the necessary adjoint variables [42, 46, 100, 110]. In AStrO, the transient thermo-elastic analysis is performed first and the solution at every time step is written to disk. Later, in the adjoint calculation, the solution at each time step is read back in during the backward sweep in time.

4.3 Aero-Thermo-Elastic Sensitivity Analysis Implementation

In this section, we describe the implementation of the coupled aero-thermo-elastic sensitivities as done in this work. For the implementation, it is desirable to follow the solution strategies and data structure used for the analysis problem, as closely as possible. This would allow the use of the same disciplinary solvers for the respective sensitivity problem. Furthermore, it would mean that the data transferred between the disciplines would consist of vectors of the same dimensions for the analysis, the tangent and adjoint formulations [103, 111].

4.3.1 Aero-Thermo-Elastic Tangent Sensitivity Analysis

Starting with the forward sensitivity problem, consider an objective function such as L:

$$L = L(D, u_x(D), u_F(D), u_T(D), u_s(D)) \tag{4-39}$$

As shown in Eq. (4-39) above, in addition to an explicit dependence on the design inputs D, there exists an implicit dependence through the state variables u_x, u_F, u_T, u_S, coming from the mesh motion, fluid, thermal, and structure disciplines, respectively. In all the following equations the subscripts x, F, T, and S refer to the mesh motion, fluid, thermal, and structure disciplines respectively. Using the chain rule, the sensitivity of the objective function with respect to the design variables D can be expressed as:

$$\frac{dL}{dD} = \frac{\partial L}{\partial D} + \frac{\partial L}{\partial u_x}\frac{\partial u_x}{\partial D} + \frac{\partial L}{\partial u_F}\frac{\partial u_F}{\partial D} + \frac{\partial L}{\partial u_T}\frac{\partial u_T}{\partial D} + \frac{\partial L}{\partial u_S}\frac{\partial u_S}{\partial D} \tag{4-40}$$

The above equation can also be expressed in matrix from:

$$\frac{dL}{dD} = \frac{\partial L}{\partial D} + \begin{bmatrix} \frac{\partial L}{\partial u_x} & \frac{\partial L}{\partial u_F} & \frac{\partial L}{\partial u_T} & \frac{\partial L}{\partial u_S} \end{bmatrix} \begin{bmatrix} \frac{\partial u_x}{\partial D} \\ \frac{\partial u_F}{\partial D} \\ \frac{\partial u_T}{\partial D} \\ \frac{\partial u_S}{\partial D} \end{bmatrix} \tag{4-41}$$

The governing nonlinear equations of each discipline in residual form are:

$$R_x\big(D, u_x(D), x_{surf}(D)\big) = 0 \tag{4-42}$$

$$R_F\big(D, u_F(D), T_{surf}(D), u_x(D),\big) = 0 \tag{4-43}$$

$$G_S\big(F_B(u_F(D), u_x(D))\big) = 0 \tag{4-44}$$

$$G_T\big(H_B(u_F(D), u_x(D))\big) = 0 \tag{4-45}$$

$$R_S\big(D, u_S(D), F_B(u_F(D), u_x(D))\big) = 0 \tag{4-46}$$

$$R_T\big(D, u_T(D), H_B(u_F(D), u_x(D))\big) = 0 \tag{4-47}$$

$$G_S'\big(x_{surf}(D), u_S(D)\big) = 0 \tag{4-48}$$

$$G_T'\big(T_{surf}(D), u_T(D)\big) = 0 \tag{4-49}$$

where R_x, R_F, R_S, R_T, represent the residuals of the mesh deformation, fluid, elastic, and thermal analysis problem, respectively. In the above equations, variables G_S, G_S', G_T, G_T' represent the residuals of the FSI equations for aero-elastic and aero-thermal data transfer, respectively. $F_B(u_F, u_x)$ represents pointwise surface forces, and $H_B(u_F, u_x)$ represents pointwise surface heat fluxes. In order to make this a general case, we are assuming that the residual from each domain, also depends on the design variable D.

Taking into account the governing nonlinear equations of each discipline in residual form as given previously in Eq.(4-42) - Eq.(4-49), the individual disciplinary sensitivities at one single time step are found to be the solution of the following coupled system of equations:

$$
\begin{bmatrix}
\frac{\partial R_x}{\partial u_x} & 0 & 0 & 0 & 0 & 0 & 0 & 0 & \frac{\partial R_x}{\partial x_{surf}} & 0 \\[6pt]
\frac{\partial R_F}{\partial u_x} & \frac{\partial R_F}{\partial u_F} & 0 & 0 & 0 & 0 & 0 & 0 & 0 & \frac{\partial R_F}{\partial T_{surf}} \\[6pt]
-\frac{\partial F_B}{\partial u_x} & -\frac{\partial F_B}{\partial u_f} & I & 0 & 0 & 0 & 0 & 0 & 0 & 0 \\[6pt]
-\frac{\partial H_B}{\partial u_x} & -\frac{\partial H_B}{\partial u_F} & 0 & I & 0 & 0 & 0 & 0 & 0 & 0 \\[6pt]
0 & 0 & \frac{\partial G_S}{\partial F_B} & 0 & I & 0 & 0 & 0 & 0 & 0 \\[6pt]
0 & 0 & 0 & \frac{\partial G_T}{\partial H_B} & 0 & I & 0 & 0 & 0 & 0 \\[6pt]
0 & 0 & 0 & 0 & \frac{\partial R_S}{\partial G_S} & 0 & \frac{\partial R_S}{\partial u_s} & 0 & 0 & 0 \\[6pt]
0 & 0 & 0 & 0 & 0 & \frac{\partial R_T}{\partial G_T} & 0 & \frac{\partial R_T}{\partial u_T} & 0 & 0 \\[6pt]
0 & 0 & 0 & 0 & 0 & 0 & \frac{\partial G'_S}{\partial u_s} & 0 & \frac{\partial S'}{\partial x_{surf}} & 0 \\[6pt]
0 & 0 & 0 & 0 & 0 & 0 & 0 & \frac{\partial G'_T}{\partial u_T} & 0 & \frac{\partial G'_T}{\partial T_{surf}}
\end{bmatrix}
\begin{bmatrix}
\frac{du_x}{dD} \\[6pt]
\frac{du_F}{dD} \\[6pt]
\frac{dF_B}{dD} \\[6pt]
\frac{dH_B}{dD} \\[6pt]
\frac{dS}{dD} \\[6pt]
\frac{dS_T}{dD} \\[6pt]
\frac{du_s}{dD} \\[6pt]
\frac{du_T}{dD} \\[6pt]
\frac{dx_{surf}}{dD} \\[6pt]
\frac{dT_{surf}}{dD}
\end{bmatrix}
=
\begin{bmatrix}
-\frac{\partial R_x}{\partial D} \\[6pt]
-\frac{\partial R_F}{\partial D} \\[6pt]
0 \\[6pt]
0 \\[6pt]
0 \\[6pt]
0 \\[6pt]
-\frac{\partial R_S}{\partial D} \\[6pt]
-\frac{\partial R_T}{\partial D} \\[6pt]
0 \\[6pt]
0
\end{bmatrix}
\qquad (4\text{-}50)
$$

In Eq. (4-50) above, the first and second equations correspond to equations for the mesh and flow variable sensitivities, respectively. The third and fourth equations correspond to the construction of the surface force and heat flux sensitivities, given the previous two sensitivities. The fifth and sixth equations correspond to the sensitivity of the FSI transfer from the fluid domain to the structural domain. The seventh and eight equations correspond to the sensitivity of the thermal and elastic solvers. Finally, the last two equations correspond to the sensitivity of the FSI transfer from the structural domain back to the flow solver.

Each disciplinary solution procedure requires the inversion of the same Jacobian matrix as the corresponding analysis problem, which is done using the same iterative solver. Furthermore, the fluid-structure coupling requires the transfer of the force and heat flux sensitivities from the flow domain to the structure domain. In return, we require the transfer of the surface displacement sensitivities and surface temperature sensitivities from the structure domain back to the fluid domain.

Solving the above set of equations provides us with the state variable sensitivities with respect to the design variables. Now, we can substitute this into Eq. (4-41) and solve for the complete sensitivity vector $\frac{dL}{dD}$. It can be seen from the above equation that when calculating sensitivities with the tangent method, the linearization scales directly with the number of design variables.

The flow of information in the sensitivity analysis process for the tangent method is summarized in Figure 4-2. The transfer of sensitivities in the structural domain is the same as the description given in section 4.2. When running transient aero-thermo-elastic sensitivity analysis, similar to the analysis problem, at every time step we solve a steady-state problem on the fluid domain, and a transient problem on the structure domain. Therefore, the above formulations hold for both steady-state and transient aero-thermo-elastic sensitivity analysis. The difference between the static and transient cases shows up on the structural solver, which was explained earlier on in section 4.2. In addition, in the tangent formulation, the Jacobian matrices must be linearized with respect to the solution from the fluid and structural domain at every time step.

In this dissertation, an attempt was made to couple both the aero-thermal and aero-elastic sensitivities. The implementation was made for coupling and passing all the following terms between NSU3D and AStrO: $\frac{dH_B}{dD}, \frac{dF_B}{dD}, \frac{dT_{Surf}}{dD}$, and $\frac{dx_{Surf}}{dD}$. However, the duality for the heat flux term could not be validated as of the time of writing this dissertation. Therefore, a choice was made to simplify the problem by omitting the heat flux sensitivity term from the sensitivity analysis process. Consequently, $\frac{dH_B}{dD}$ is not passed from the fluid domain to the structure domain for the aero-thermo-elastic optimization cases presented later in Chapter 5. Instead, a constant heat flux is applied as a boundary condition on the structure domain during the sensitivity analysis process.
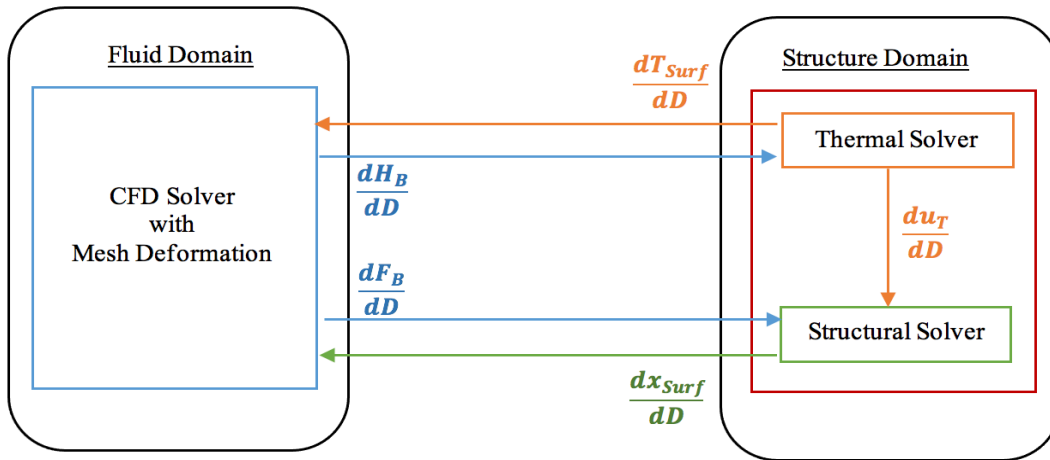
Figure 4-2 Flow of information the aero-thermo-elastic tangent sensitivity analysis.

4.3.2 Aero-Thermo-Elastic Adjoint Sensitivity Analysis

For the adjoint formulation, we require the transpose of the forward linearization as shown below:

$$\frac{dL^T}{dD} = \frac{\partial L^T}{\partial D} + \begin{bmatrix} \frac{\partial u_x}{\partial D}^T & \frac{\partial u_F}{\partial D}^T & \frac{\partial u_T}{\partial D}^T & \frac{\partial u_S}{\partial D}^T \end{bmatrix} \begin{bmatrix} \frac{\partial L}{\partial u_x}^T \\ \frac{\partial L}{\partial u_F}^T \\ \frac{\partial L}{\partial u_T}^T \\ \frac{\partial L}{\partial u_S}^T \end{bmatrix} \tag{4-51}$$

The corresponding adjoint problem can be obtained by pre-multiplying Eq.(4-50) by the inverse of the large coupling matrix, and substituting this into Eq.(4-41), transposing the entire system, and defining adjoint variables at one single time step as solutions to the following coupled system:

$$\begin{bmatrix}
\frac{\partial R_x}{\partial u_x}^T & \frac{\partial R_F}{\partial u_x}^T & -\frac{\partial F_B}{\partial u_x}^T & -\frac{\partial H_B}{\partial u_x}^T & 0 & 0 & 0 & 0 & 0 & 0 \\
0 & \frac{\partial R_F}{\partial u_F}^T & -\frac{\partial F_B}{\partial u_F}^T & -\frac{\partial H_B}{\partial u_F}^T & 0 & 0 & 0 & 0 & 0 & 0 \\
0 & 0 & I & 0 & \frac{\partial G_S}{\partial F_B}^T & 0 & 0 & 0 & 0 & 0 \\
0 & 0 & 0 & I & 0 & \frac{\partial G_T}{\partial H_B}^T & 0 & 0 & 0 & 0 \\
0 & 0 & 0 & 0 & I & 0 & \frac{\partial R_S}{\partial G_T}^T & 0 & 0 & 0 \\
0 & 0 & 0 & 0 & 0 & I & 0 & \frac{\partial R_T}{\partial G_T}^T & 0 & 0 \\
0 & 0 & 0 & 0 & 0 & 0 & \frac{\partial R_S}{\partial u_S}^T & 0 & \frac{\partial G'_S}{\partial u_S}^T & 0 \\
0 & 0 & 0 & 0 & 0 & 0 & 0 & \frac{\partial R_T}{\partial u_T}^T & 0 & \frac{\partial G'_T}{\partial u_T}^T \\
\frac{\partial R_x}{\partial x_{surf}}^T & 0 & 0 & 0 & 0 & 0 & 0 & 0 & \frac{\partial G'_S}{\partial x_{surf}}^T & 0 \\
0 & \frac{\partial R_F}{\partial T_{surf}}^T & 0 & 0 & 0 & 0 & 0 & 0 & 0 & \frac{\partial G'_T}{\partial T_{surf}}^T
\end{bmatrix} \begin{bmatrix} \Lambda_{u_x} \\ \Lambda_{u_F} \\ \Lambda_{F_B} \\ \Lambda_{H_B} \\ \Lambda_S \\ \Lambda_{S_T} \\ \Lambda_{u_S} \\ \Lambda_{u_T} \\ \Lambda_{x_{surf}} \\ \Lambda_{T_{surf}} \end{bmatrix} = \begin{bmatrix} \frac{\partial L}{\partial u_x}^T \\ \frac{\partial L}{\partial u_F}^T \\ 0 \\ 0 \\ 0 \\ \frac{\partial L}{\partial u_S}^T \\ \frac{\partial L}{\partial u_T}^T \\ 0 \\ 0 \\ 0 \end{bmatrix}$$

$$(4-52)$$

Once again, the solution of the various disciplinary adjoint equations requires the inversion of the corresponding disciplinary Jacobians (transposed in this case) which can be accomplished using the same iterative solvers as for the analysis and forward sensitivity problems. Additionally, the input to the structural adjoint problem consists of the variables $\Lambda_{x_{surf}}$ and

$\Lambda_{T_{surf}}$, which have the same dimensions as the surface displacements and temperatures output from the structural analysis solver. On the other hand, the output of the structural adjoint solver consists of the variables Λ_{F_B} and Λ_{H_B}, which are of the same dimension as the force and heat flux inputs to the structural solver in the analysis problem, respectively. Once the vector of adjoint variables for each discipline is available, it may be substituted into the total sensitivity equation as:

$$\frac{dL}{dD}^T = \frac{\partial L}{\partial D}^T + \begin{bmatrix} -\frac{\partial R_x}{\partial D}^T & -\frac{\partial R_F}{\partial D}^T & -\frac{\partial R_T}{\partial D}^T & -\frac{\partial R_S}{\partial D}^T \end{bmatrix} \begin{bmatrix} \Lambda_{u_x} \\ \Lambda_{u_f} \\ \Lambda_{u_T} \\ \Lambda_{u_S} \end{bmatrix} \qquad (4\text{-}53)$$

Again, it is clear from the above equations that the number of design variables only affects the matrix-vector products at the end of the computation process [46].

The flow of information for the sensitivity analysis process using the adjoint method is summarized in Figure 4-3. The description of transfer of sensitivities in the solid domain was presented earlier in section 4.2. When running transient aero-thermo-elastic sensitivity analysis, similar to the analysis problem, we solve a steady-state problem on the fluid domain and a transient problem on the structure domain. Additionally, we require the solution history for both the fluid and structure domain at each time step. Therefore, first the analysis is run and the structural and flow solution at each time step is written to file and then during the adjoint reverse time integration, these solutions are read back from disk.
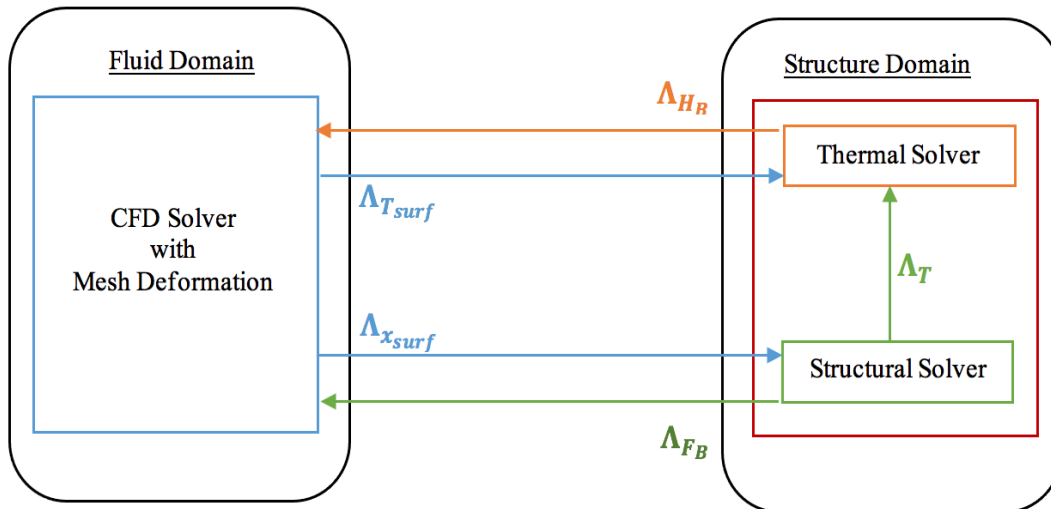
Figure 4-3 Flow of information for aero-thermo-elastic adjoint sensitivity analysis.

In this dissertation, an attempt was made to couple both the aero-thermal and aero-elastic adjoint sensitivities. The implementation was made for coupling and passing all the following terms between NSU3D and AStrO: $\Lambda_{F_B}, \Lambda_{H_B}, \Lambda_{x_{surf}}$, and $\Lambda_{T_{surf}}$. However, as mentioned previously the duality for the heat flux terms could not be validated. Therefore, similar to the tangent sensitivity calculations, certain simplifications were made for all the aero-thermo-elastic optimization cases presented later in Chapter 5. The heat flux adjoint is not considered in the sensitivity analysis process for these cases. Λ_{H_B} is not passed from the structure domain to the fluid domain. Instead, a fixed heat flux is applied as a boundary condition on the structure domain .

4.4 Summary

In this chapter, we looked at the history of multi-disciplinary optimization and the incentive for using such simulations. First, a review of the literature was done on gradient based optimization, which is the most popular numerical optimization method used in the field of aeronautics. Next, it was concluded that the adjoint method is the most efficient method for high-fidelity multi-disciplinary optimization. In addition, it was established that the adjoint method can be verified against the tangent method using the duality property. Finally, a description of the formulation and implementation of the thermo-elastic and aero-thermo-elastic sensitivity analysis used in this study was presented for both the tangent and adjoint methods.

5 SENSITIVITY ANALYSIS AND OPTIMIZATION RESULTS

This chapter presents validation results for the coupled adjoint sensitivities. The adjoint sensitivities are verified against the tangent, the complex-step, and the finite-difference methods. As mentioned earlier, AStrO has the capability of calculating exact sensitivities using the adjoint method [50]. In this dissertation, a verification of the static and transient thermal and thermo-elastic adjoint sensitivities of AStrO has been carried out. This is followed by the coupled aero-thermo-elastic sensitivity verification. These sensitivities are then applied to optimization problems.

5.1 Thermo-Elastic Sensitivity Analysis and Optimization Results

In this section, validation results for the thermal and thermo-elastic sensitivity analysis and optimization capabilities of AStrO are presented. These results were first reported in reference [30]. For each case, the adjoint linearization is verified using the duality relation [85] to the tangent approach, while the tangent sensitivities are verified with the complex-step method [50, 104]. For all the optimization problems presented in this section the on-board optimizer in AStrO is used. This onboard optimizer uses the steepest-descent line search algorithm with backtracking.

5.1.1 Static Thermal Sensitivity Analysis and Optimization of a Heated Panel

As mentioned previously, the fluid/thermal/structural interactions play an important role in many design problems. One such problem is the thermal protection systems on hypersonic flight vehicles. The study of aerodynamically heated panels is a preliminary but important step towards the objectives of analyzing more realistic materials and structures for such vehicles [25]. For this reason, the sensitivity analysis and optimization of heated panels is studied throughout this chapter. Starting with a static heated panel case in this section.

As shown in Figure 5-1, the panel used for this first case is made of multiple layers of material. The test panel is 4*in* long, has a thickness of 0.1*in*, and a width of 0.5*in.* The panel mesh has 5,628 nodes and 3,990 hexahedral elements. The description of the material properties of the panel is summarized in Table 5-1. There are three layers of material in the panel, the top layer, which acts as the thermal protection layer on the panel and is made of Inconel 718, the middle layer, which is the insulation layer and is made of Saffil, and the bottom layer, which is

made of AL 2024. The thickness of each layer of material is identical and is equal to 0.33333 *in*.

The panel is supported by immovable supports on the left and right edges of the bottom surface. The bottom surface of the panel is insulated, while the faces on the right and left side of the panel have a constant temperature equal to the initial temperature of 530*R*. A uniform heat flux of $0.02 \frac{BTU}{in^2.s}$ is applied to the top surface of the panel. This thermal boundary condition is applied in order to mimic the aerodynamic heating of the panel for the thermo-elastic optimization. Under these thermal and structural boundary conditions, the panel deforms into a convex shape as shown in Figure 5-2.

Table 5-1 Description of material properties for each layer of the static heated panel [112].

Property	Thermal Protection layer (Top layer)	Insulation layer (Middle layer)	Bottom layer
Material	Inconel 718	Saffil	Al 2024
Density (ρ)	0.29443743 *lbm/in³*	0.001806365 *lbm/in³*	0.09284714 *lbm/in³*
Thermal Conductivity (k)	0.140442×10⁻³ *BTU/(s.in.R)*	0.00104329 ×10⁻³ *BTU/(s.in.R)*	1.070037 ×10⁻³ *BTU/(s.in.R)*
Specific heat capacity (C)	0.097926818 *BTU/(lbm.R)*	0.224992835 *BTU/(lbm.R)*	0.225470526 *BTU/(lbm.R)*
Thermal expansion (α)	5.83333×10⁻⁶ *1/R*	1×10⁻¹⁰ *1/R*	8.88889×10⁻⁶ *1/R*
Modulus of elasticity (E)	2.8282183 ×10⁷ *lbf/in²*	4.351105181 ×10⁴ *lbf/in²*	9.862505076 ×10⁶ *lbf/in²*
Poisson's ration (v)	0.28 (dimensionless)	0.26 (dimensionless)	0.32 (dimensionless)
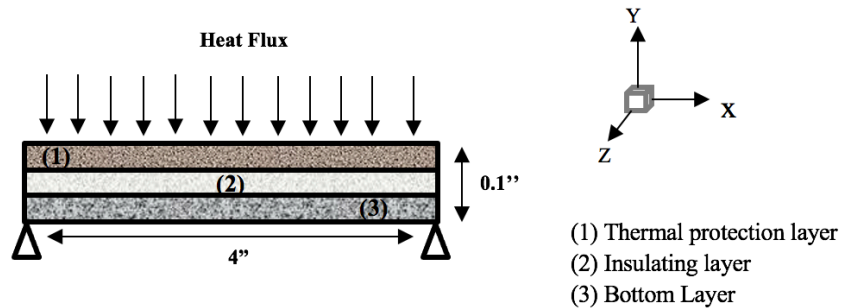
Figure 5-1 Coupled thermal/structural model and boundary conditions for the static heated panel made of multiple materials.

Figure 5-2 Panel with convex deformation.

5.1.1.1 *Thermal Sensitivity Analysis Validation for the Static Heated Panel*

For this case, the objective function is defined to keep the average temperature of the bottom layer of the panel as close as possible to $T_{limit} = 930R$, which is much lower than the value obtained from the baseline panel design, as can be seen later from the results. This objective function is chosen since the convex deformation of the panel is a direct result of the rise in the temperature of the panel. Hence, the objective function for this case is defined as:

$$L = \left(\sum_{i=1}^{n} \frac{(Temperature(i) - T_{limit})^2}{n^2} \right) +$$
$$10^5 \times (Mass_{top\ layer} - 2.5 \times Mass_{inital\ top\ layer})^2 \quad (5\text{-}1)$$

where 'i' is the node number and 'n' is the total number of nodes that make up the mesh for the bottom layer of the panel. It should be noted that a mass penalty is used in Eq. (5-1). This is because the thickness of the top layer is chosen as a design variable in this problem.

In order to test the adjoint-based sensitivities, the elastic modulus, the thermal conductivity, the coefficient of thermal expansion of the thermal protection layer (top layer), and the thickness of the top layer of the panel are defined as the design variables. This is because the top layer is considered to be the thermal protection layer. The sensitivity of each property was scaled to the original value, resulting in the following design-dependent definitions:

$$\begin{cases} E_{Top\ layer} = E_0 + 2 \times 10^6 D_1 \\ k_{Top\ layer} = k_0 + 10^{-3} D_2 \\ \alpha_{Top\ layer} = \alpha_0 + 5 \times 10^{-5} D_3 \\ Thickness_{Top\ layer} = Thickness_{intial-top\ layer} \times D_4 \end{cases} \quad (5\text{-}2)$$

The adjoint based sensitivities were verified against the sensitivities calculated by the tangent and complex-step methods. The results are shown in Table 5-2. As can be seen the sensitivity of the objective function with respect to the modulus of elasticity and thermal expansion is zero. Since the objective function is based on temperature, this is to be expected because of the one-way dependence of deformation on temperature in AStrO. The sensitivity of the objective function with respect to the thermal conductivity and thickness match for the adjoint, tangent and complex differentiation methods, down to machine precision.

Table 5-2 Comparison of the objective function sensitivities for the static heated panel for the adjoint, tangent and complex-step methods.

	Adjoint	*Tangent*	*Complex*
D_1 −Modulus of elasticity (E)	0.000000000000	0.000000000000	0.000000000000
D_2 −Thermal Conductivity *(k)*	-215.2563863794**097**	-215.25638637940**875**	-215.2563863794**592**
D_3 −Thermal expansion (α)	0.000000000000	0.000000000000	0.000000000000
D_4 − *Thickness*	-145.8261895007**903**	-145.8261895007**905**	-145.8261895008**018**

5.1.1.2 *Thermal Optimization of the Static Heated Panel Case*

We used the verified sensitivities calculated from the adjoint-based method to run a thermo-elastic optimization for this static multi-layered panel case using AStrO. The goal in this optimization problem is to minimize the objective function presented in Eq. (5-1) with respect to the thermal conductivity and the thickness of the thermal protection layer, which forms the top layer of the panel. Table 5-3 shows the change in the objective function from the baseline panel to the thermo-elastically optimized panel. Temperature contours for the baseline and thermo-elastically optimized panels are shown in Figure 5-3 and Figure 5-4, respectively. These results clearly show that the average temperature of the lower part of the panel has decreased as desired.

Table 5-3   Comparison of the baseline and thermo-elastically optimized objective function for the static panel case.

	Baseline	*Thermo-elastic optimization*
Objective function (Eq. (5-1))	137.10305736304662	12.496144040068716
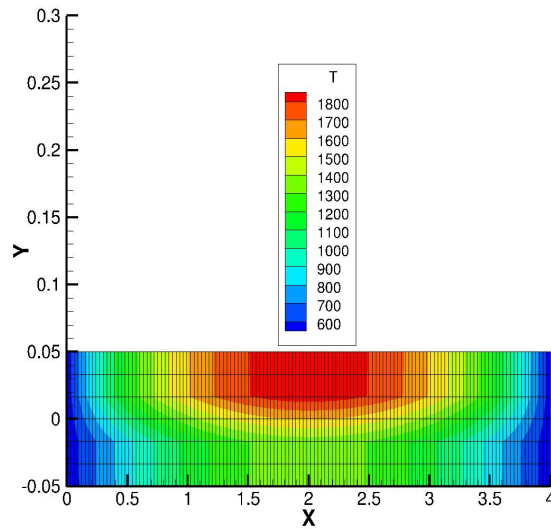
Figure 5-3   Temperature contour of the baseline static heated panel.
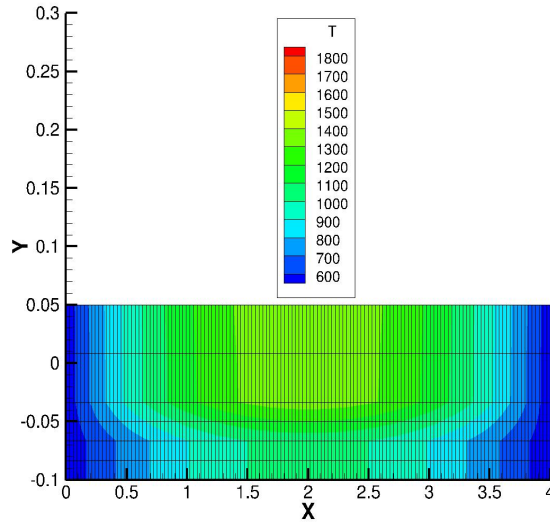
Figure 5-4   Temperature contour of the thermo-elastically optimized static heated panel.

The initial and optimized material properties of the panel are summarized in Table 5-4 below. The thickness of the top layer has increased in a constrained manner due to the penalty put on the mass in the objective function. The increase in the thermal conductivity of the top layer is due to the low temperature applied at the two sides of the panel, which act as a cooling mechanism for the panel. The convergence of the optimization process for the static heated panel case is shown in Figure 5-5, where the objective is reduced by a factor of 11 over 13 design steps.

Table 5-4   Changes in design variables and optimized material properties of the static heated panel.

Material Properties of the top layer	Initial Material Properties	Optimized Material Properties
Thermal Conductivity (k)	0.140442×10^{-3} BTU/(s.in.R)	0.3133×10^{-3} BTU/(s.in.R)
Thickness	0.0333333 in	0.08325182 in
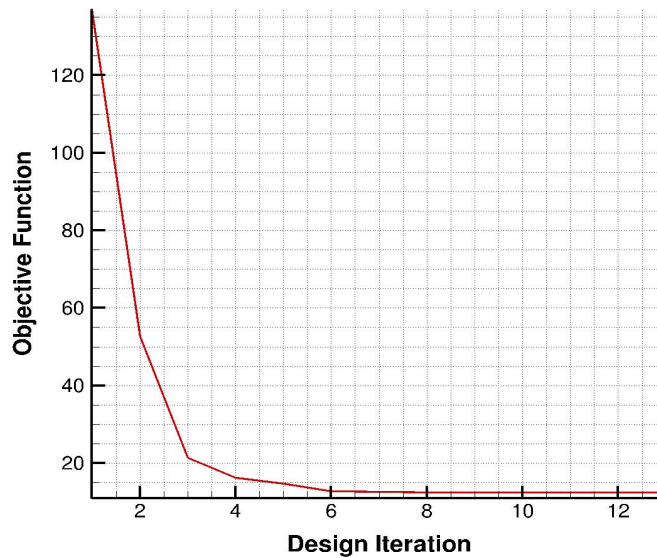
Figure 5-5   Convergence of the thermo-elastic optimization process for the static heated panel.

5.1.2 Static Thermo-Elastic Sensitivity Analysis and Optimization of a Rectangular Bar with Applied Mechanical and Thermal Loads

For this case, we study the thermo-elastic sensitivity analysis and optimization in a rectangular bar with both thermal and mechanical loads applied. The bar has a length of $10m$ in the z-direction, and $1m$ in both the x- and y-directions. The mesh used for this study has 44 nodes and 10 hexahedral elements.

The applied boundary conditions are illustrated in Figure 5-6. The corners of the lower x-face are fixed to zero displacement and a temperature of zero degrees Celsius is applied at these corners. A constant heat flux of 7 W/m^2 is applied to the upper x-face of the bar. Also, a force of $1N$ is applied to the points at the center of the bar on the top x-face in the negative x-direction. The material properties of the rectangular bar are presented in Table 5-5.
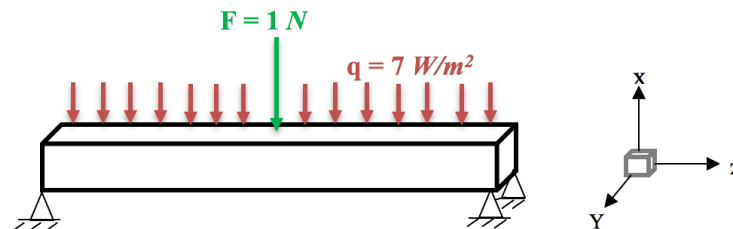
Figure 5-6 Applied boundary conditions for the thermo-elastic sensitivity calculation and optimization of the static rectangular bar.

83

Table 5-5   Rectangular bar material properties.

Property	Value
Thermal Conductivity (k)	1.0 W/(m.K)
Thermal expansion (α)	10^{-4} 1/K
Modulus of elasticity (E)	10^6 N/m²
Poisson's ration (v)	0.3 (dimensionless)

5.1.2.1   *Thermo-Elastic Sensitivity Analysis Validation for the Static Rectangular Bar*

For this case, we define the objective function to be the square of the displacement at the center of the bar in the *x*-direction. The objective function for this case is defined as:

$$L = (Displacement\_X(i))^2 \qquad (5\text{-}3)$$

where 'i' is the index of the center node on the bottom x-face of the bar.

In order to test the adjoint-based sensitivities, the elastic modulus, the thermal conductivity and the coefficient of thermal expansion of the rectangular bar are defined as design variables. The sensitivity of each property was scaled to the original value, resulting in the following design-dependent definitions:

$$\begin{cases} E = E_0 + 10^6 D_1 \\ k = k_0 + D_2 \\ \alpha = \alpha_0 + 10^{-4} D_3 \end{cases} \qquad (5\text{-}4)$$

The adjoint and tangent formulations are mathematically equivalent, using exact differentiation of the governing equations, and they agree nearly to machine precision. Complex differentiation does not use the linearization of the governing equations but works much like a high-precision finite-difference method and is also numerically equal to the other two results. The sensitivities given in Table 5-6 indicate that the adjoint implementation correctly differentiates the finite-element solution in this case.

Table 5-6   Comparison of the objective function sensitivities for the static rectangular bar with applied thermal and structural loads (objective is a function of the displacement in the *x*-direction at the center of the bar).

	Adjoint	Tangent	Complex
D_1 −Modulus of elasticity (E)	- 0.0002479963569	- 0.0002479963569	- 0.0002479963569
D_2 −Thermal Conductivity (k)	- 0.2890102246446	- 0.2890102246446	- 0.2890102246446
D_3 −Thermal expansion (α)	0.5857706751382	0.5857706751382	0.5857706751382

5.1.2.2 *Thermo-Elastic Optimization for the Static Rectangular Bar*

After the sensitivities calculated using the adjoint-based method were verified, we used these sensitivities for a thermo-elastic optimization study on the rectangular bar. The goal in this optimization problem is to minimize the objective function presented in Eq. (5-3) with respect to the design variables defined in Eq. (5-4). The vector of design variables contains both elastic and thermal material properties. The objective function, which is based on the deformation of the rectangular bar in the *x*-direction, is a function of both thermal and elastic material properties.

Table 5-7 shows the change in the objective function from the baseline rectangular bar to the thermo-elastically optimized case. The initial and optimized material properties are summarized in Table 5-8. These changes in the material properties allow the thermal deflection to balance the applied force. Contours of displacement in the *x*-direction for the baseline and thermo-elastically optimized rectangular bar are shown in Figure 5-7 and Figure 5-8 respectively. It can be seen from the results in Table 5-7, Figure 5-7, and Figure 5-8 that the displacement in the *x*-direction at the bottom center of the bar is now zero. The convergence of the optimization process for the rectangular bar case is shown in Figure 5-9. The optimizer was able to fine the optimum solution after 11 optimization cycles.

Table 5-7   Comparison of the change in the objective function for the baseline and thermo-elastically optimized static rectangular bar.

	Baseline	*Thermo-elastic optimization*
Objective Function (Eq. (5-3))	0.14439066575919221	$1.0132638884907125 \times 10^{-10}$

Table 5-8   Initial and thermo-elastically optimized material properties of the static rectangular bar.

Material Properties	*Initial Material Properties*	*Optimized Material Properties*
Modulus of elasticity (E)	10^6 N/m^2	1.000042931×10^6 N/m^2
Thermal Conductivity (k)	1.0 W/(m.K)	1.13765820913759477W/(m.K)
Thermal expansion (α)	10^{-4} 1/K	0.50708×10^{-6} 1/C
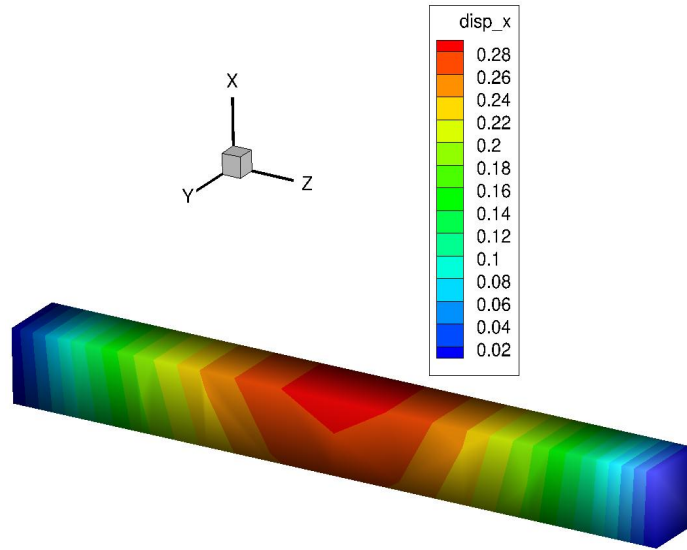
Figure 5-7 Displacement contour for the baseline rectangular bar in the *x*-direction.
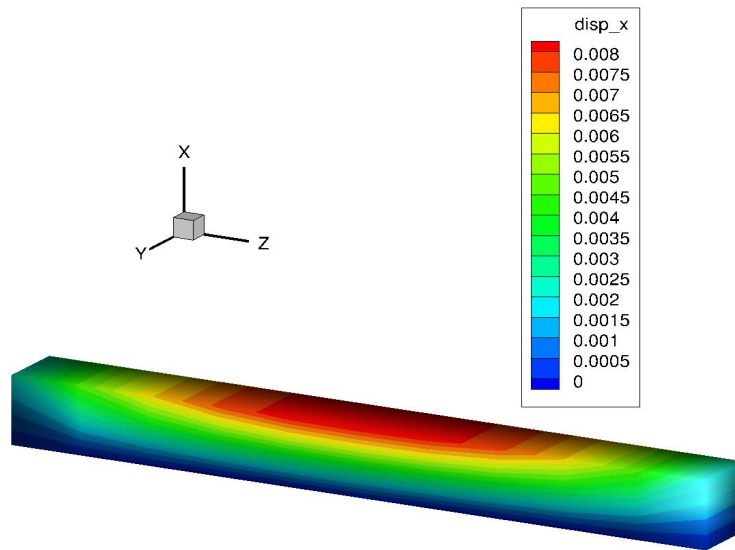
Figure 5-8 Displacement contour for the thermo-elastically optimized rectangular bar in the *x*-direction.
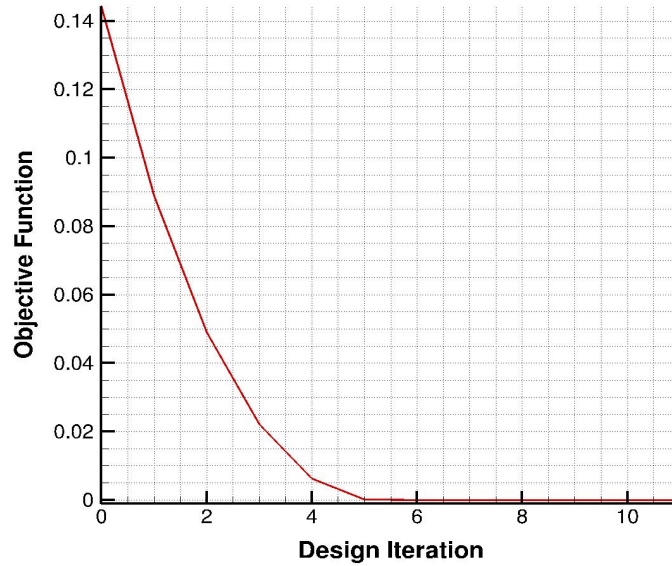
Figure 5-9 Thermo-elastic optimization convergence for the rectangular bar under thermal and mechanical load.

5.1.3 Static Thermo-Elastic Optimization with Large Number of Design Variables

AStrO is capable of performing optimization with large number of design variables. In this section we look at an optimization problem to showcase this capability. We take into account another heated panel case. This problem has similar boundary condition as to the panel shown in Figure 5-10. The panel is supported by immovable supports on the left and right edges of the bottom surface. The bottom surface of the panel is insulated, while the faces on the right and left side of the panel have a constant temperature equal to the initial temperature of $530R$. A uniform heat flux of $0.00002 \frac{BTU}{in^2.s}$ is applied to the top surface of the panel. Under these thermal and structural boundary conditions, the panel deforms into a convex shape.

The test panel is $4in$ long, has a thickness of $0.1in$, and a width of $0.5in$. The panel is made of one layer from AM-350 stainless steel. The material properties of AM-350 have been previously provided in Table 5-9
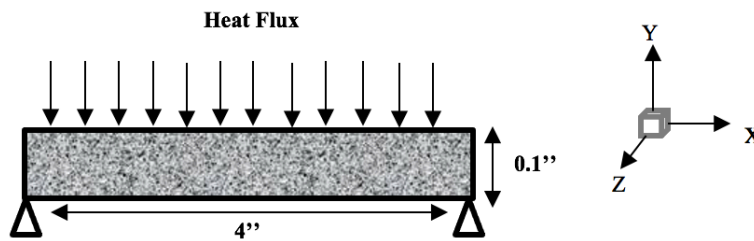
Figure 5-10 Coupled thermal/structural model and boundary conditions for the static heated panel case with large number of design variables.

87

Table 5-9　Static heated panel material properties [26].

Property	Value
Density (ρ)	0.282 lbm/in^3
Thermal Conductivity (k)	0.12864 $\times 10^{-3}$ $BTU/(s.in.R)$
Specific heat capacity (C)	0.11162 $BTU/(lbm.R)$
Thermal expansion (α)	0.62643 $\times 10^{-5}$ $1/R$
Modulus of elasticity (E)	0.35346 $\times 10^8$ lbf/in^2
Poisson's ration (v)	0.25 (dimensionless)

For this case, the objective function is derived using the deformation of the panel in the *y*-directions, as shown below:

$$L = \sum_{i=1}^{n}(Disp\_y(i))^2 \qquad (5\text{-}5)$$

where '*i*' is the node number and '*n*' is the total number of nodes in the panel. The mesh used in this study has 3,216 nodes, and 1,995 hexahedral elements.

The design variables are chosen to be the mechanical load applied to the nodes located on the top surface of the panel. The top surface of the panel has 804 nodes. Hence, we will have 804 design variables. The goal here is to counterbalance the thermal load with the mechanical loads.

Table 5-10 shows the change in the objective function from the baseline panel to the thermo-elastically optimized panel case. The final values of the design variables are plotted in Figure 5-11. In this figure we can see the computed values for the mechanical loads applied to the top surface of the panel. The results correspond well to the original deformation of the panel which is plotted in Figure 5-12. We can see that the mechanical load is applied to the negative *y*-direction in order to counterbalance the deformation of the panel in the positive *y*-direction. Also, the maximum mechanical load is at the center of the panel, which is where the maximum deformation occurs.

Table 5-10 Comparison of the baseline and thermo-elastically optimized objective function for a static heated panel with large number of design variables.

	Baseline	Thermo-elastic optimization
Objective function (Eq. (5-5))	39.952981948270583	4.8801936780745416
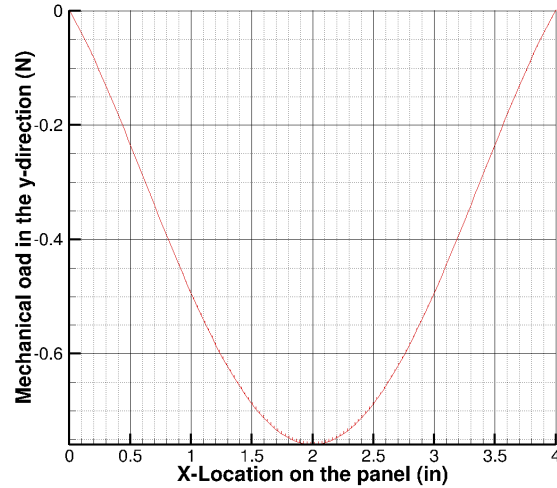
Figure 5-11 Mechanical loads applied in the *y*-direction at each node on the surface of the panel as computed by AStrO after thermo-elastic optimization, for the static heated panel case with large number of design variables.
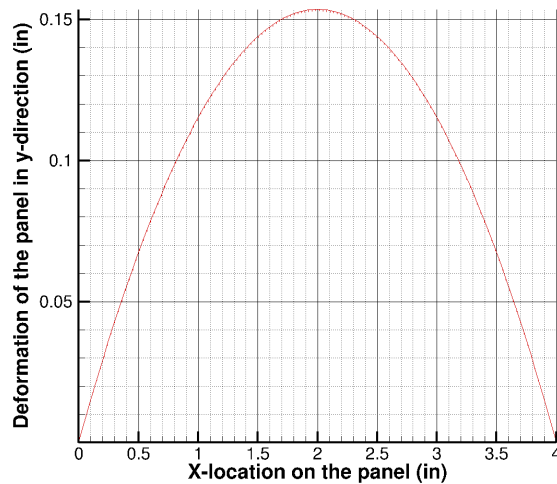
Figure 5-12 Displacement in the *y*-directions for the baseline as computed by AStrO, for the static heated panel case with large number of design variables.

Contours of the displacement in the *y*-directions for the baseline and thermo-elastically optimized panel are shown in Figure 5-13. From these results, it is clear that the convex deformation of the panel is drastically reduced due to the optimization process.
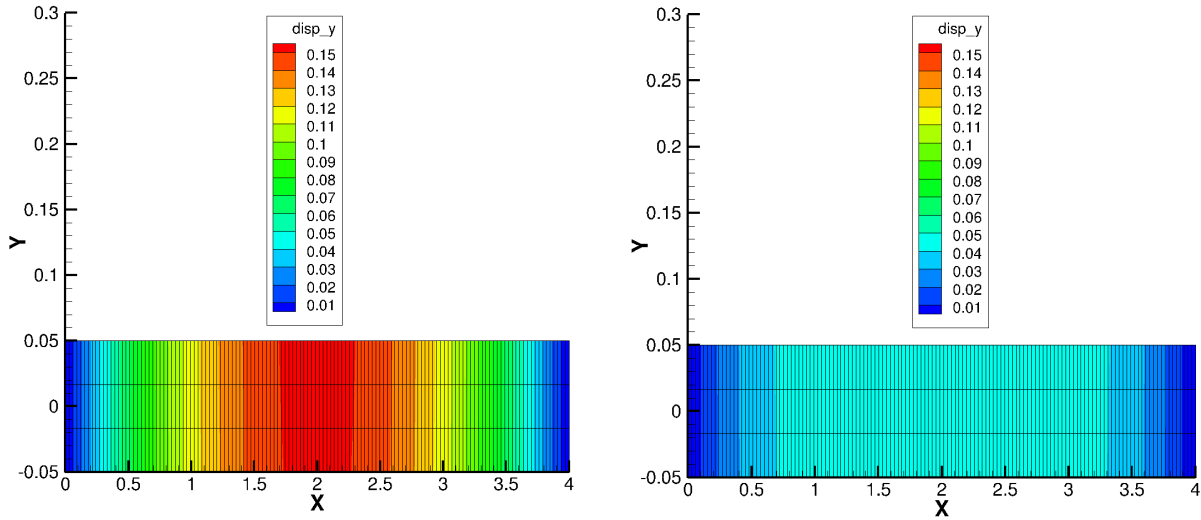
Figure 5-13 Contours of displacement in the *y*-directions for the baseline(right) and thermo-elastically optimized (left), static heated panel case with large number of design variables as calculated by AStrO.

The convergence of the optimization process for the static heated panel with large number of design variables is shown in Figure 5-14. After 145 optimization cycles the process is terminated once the objective function has reached a tenth of its original value.
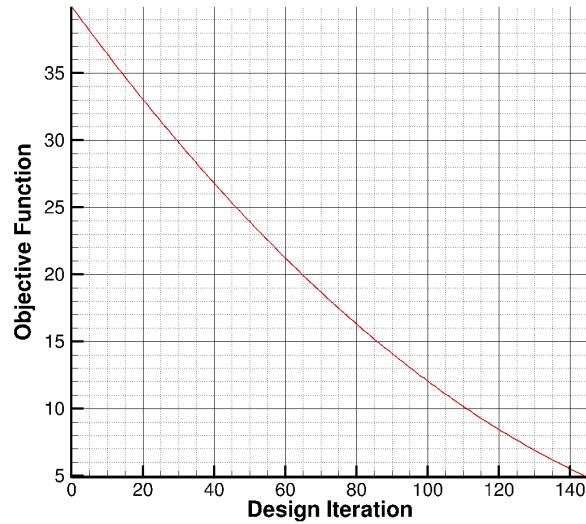
Figure 5-14 Convergence of the thermo-elastic optimization process for the static heated panel case with large number of design variables.

5.1.4 Transient Thermo-Elastic Sensitivity Analysis and Optimization of a Heated Panel

In this section, the sensitivities calculated using the discrete adjoint method are validated for a transient thermo-elastic heated panel problem. This test case was first studied in reference [27]. In Chapter 3, the same problem was used to validate AStrO's thermo-elastic analysis capabilities. Since this problem was described in detail in Chapter 3, only a brief overview of the problem is provided for the reader's convenience in this section.

A schematic of the computational model and boundary conditions is shown in Figure 5-10 presented in the previous section. The panel is supported by immovable supports on the left and right edges of the bottom surface. The bottom surface of the panel is insulated, while the faces on the right and left side of the panel have a constant temperature equal to the initial temperature of $530R$. A uniform heat flux is applied to the top surface of the panel. Under these thermal and structural boundary conditions, the panel deforms into a convex shape [25-27].

The test panel is $4in$ long, has a thickness of $0.1in$, and a width of $0.5in$. The panel is made from AM-350 stainless steel. The material properties of the panel are given in Table 5-9 [26] presented in the previous section.

For the corresponding aero-thermo-elastic case, at these early times, the heating rate across the panel is nearly uniform, and can be approximated by the following equation [26]:

$$\dot{q}(t) = 0.026 - 0.0001t \ \left(\frac{BTU}{in^2.s}\right) \qquad (5\text{-}6)$$

Equation (5-5) is used as a thermal boundary condition in order to mimic the aerodynamic heating for the thermo-elastic problem. The time step used for the coupled thermo-elastic analysis is $1s$. Hence 30 time steps were required to heat the panel for $30s$.

5.1.4.1 *Thermo-Elastic Sensitivity Analysis Validation for the Transient Heated Panel*

For this case, the objective function is derived using the deformation of the panel in the x- and y-directions, as shown below:

$$L = \sum_{i=1}^{n}(Disp\_x(i))^2 + (Disp\_y(i))^2 \qquad (5\text{-}7)$$

where 'i' is the node number and 'n' is the total number of nodes in the panel. The mesh used in this study has 3,216 nodes, and 1,995 hexahedral elements.

In order to test the adjoint-based sensitivities, the elastic modulus, the thermal conductivity, the coefficient of thermal expansion, and the specific heat capacity of the panel material were defined as the design variables. The sensitivity of each property was scaled to the original value, resulting in the following design-dependent definitions:

$$\begin{cases} E = E_0 + 10^7 D_1 \\ k = k_0 + 10^{-4} D_2 \\ \alpha = \alpha_0 + 10^{-6} D_3 \\ C = C_0 + 10^{-1} D_4 \end{cases} \qquad (5\text{-}8)$$

The adjoint-based sensitivities were verified against the sensitivities calculated by the tangent and complex-step methods. Table 5-11 - Table 5-14 show a comparison of coupled thermo-elastic sensitivities obtained from the complex analysis run with those of the tangent and adjoint linearization for 6 different time steps. Each table presents results for one of the design variables defined in Eq. (5-7). As shown in these tables, the sensitivity values from the tangent and adjoint linearization matches with the complex-step method to machine precision.

Table 5-11   Comparison of objective sensitivities for the transient heated panel for the adjoint, tangent and complex-step methods for design variable D_1 as defined in Eq. (5-7).

Time step	Adjoint	Tangent	Complex
5	-0.0005658745**509**	-0.0005658745**509**	-0.0005658745**510**
10	-0.0041847191**992**	-0.0041847191**992**	-0.0041847191**996**
15	-0.0132425156**473**	-0.0132425156**472**	-0.0132425156**484**
20	-0.0297337370**432**	-0.0297337370**432**	-0.0297337370**458**
25	-0.0553518559**203**	-0.0553518559**203**	-0.0553518559**249**
30	-0.0915353372**070**	-0.0915353372**071**	-0.0915353372**147**

Table 5-12   Comparison of objective sensitivities for the transient heated panel for the adjoint, tangent and complex-step methods for design variable D_2 as defined in Eq. (5-7).

Time step	Adjoint	Tangent	Complex
5	-0.0270281059525	-0.0270281059525	-0.0270281059525
10	-0.1424427208577	-0.1424427208577	-0.1424427208578
15	-0.4235076821464	-0.4235076821462	-0.4235076821465
20	-0.9637033879671	-0.9637033879673	-0.9637033879675
25	-1.8656308994337	-1.8656308994336	-1.8656308994339
30	-3.2372661777168	-3.2372661777178	-3.2372661777184

Table 5-13 Comparison of the objective sensitivities for the transient heated panel for the adjoint, tangent and complex-step methods for design variable D_3 as defined in Eq. (5-7).

Time step	Adjoint	Tangent	Complex
5	0.0644539160860	0.0644539160860	0.0644539160860
10	0.4214617163555	0.4214617163556	0.4214617163557
15	1.2889374961929	1.2889374961924	1.2889374961929
20	2.8522092885360	2.8522092885354	2.8522092885367
25	5.2696838576481	5.2696838576459	5.2696838576481
30	8.6764603110799	8.6764603110797	8.6764603110834

Table 5-14 Comparison of objective sensitivities for the transient heated panel for the adjoint, tangent and complex-step methods for design variable D_4 as defined in Eq. (5-7).

Time step	Adjoint	Tangent	Complex
5	-0.3298385175240	-0.3298385175243	-0.3298385175244
10	-2.1963367650602	-2.1963367650602	-2.1963367650615
15	-6.7320990871707	-6.7320990871682	-6.7320990871707
20	-14.8687791829420	-14.8687791829394	-14.8687791829461
25	-27.3767070817806	-27.3767070817733	-27.3767070817816
30	-44.8893798636163	-44.8893798636146	-44.8893798636355

5.1.4.2 *Thermo-Elastic Optimization for a Transient Aerodynamically Heated Panel*

The panel used for this optimization study has the same material properties as the transient heated panel case presented in the previous section. These material properties are summarized in Table 5-9. A schematic of the computational model and the boundary conditions for this problem is shown in

Figure 5-15. The panel is supported by immovable supports on the left and right edges of the bottom surface. The bottom surface of the panel is insulated, while the faces on the right and left sides of the panel have a constant temperature equal to the initial temperature of 530R. A uniform heat flux and a uniform aerodynamic force are applied to the top surface of the panel.

The applied uniform heat flux and aerodynamic boundary conditions are invoked to mimic the aerodynamic heating and forces for the thermo-elastic problem. The aerodynamic force across the panel is nearly uniform and has a value of 0.002N. The heating rate across the panel is nearly uniform, and can again be approximated by Eq. (5-5) presented in the previous section [26].
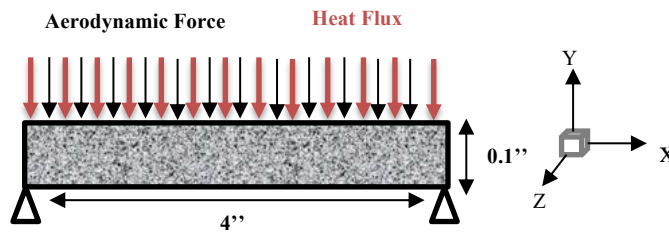
Figure 5-15 Coupled thermal/structural model and boundary conditions for the transient aerodynamically heated panel.

The goal of this optimization problem is to minimize the objective function presented in Eq. (5-6) with respect to the design variables defined by Eq. (5-7). The vector of design variables contains both elastic and thermal material properties. The objective function, which is created from the deformation of the panel in the *x*- and *y*-directions, is a function of both thermal and elastic material properties. The design variables are bounded to make sure that realistic material properties are obtained after the optimization process.

$$\begin{cases} -0.188 \leq D_1 \leq 0.188 \\ -0.72 \leq D_2 \leq 0.72 \\ -2.0 \leq D_3 \leq 2.0 \\ -0.1 \leq D_4 \leq 0.1 \end{cases} \tag{5-9}$$

The time step used for the coupled thermo-elastic analysis is 1*s*. Hence, 30 time steps were required to heat the panel for 30*s*. Table 5-15 shows the change in the objective function from the baseline panel to the thermo-elastically optimized panel case. Contours of the displacement in the *x*- and *y*-directions for the baseline and thermo-elastically optimized panel are shown in Figure 5-16 and Figure 5-17. From these results, it is clear that the convex deformation of the panel is drastically reduced due to the optimization process.

Table 5-15 Comparison of the baseline and thermo-elastically optimized objective function for the transient aerodynamically heated panel.

	Baseline	*Thermo-elastic optimization*
Objective function (Eq. (5-6))	25.78179928166821	9.37336380561037
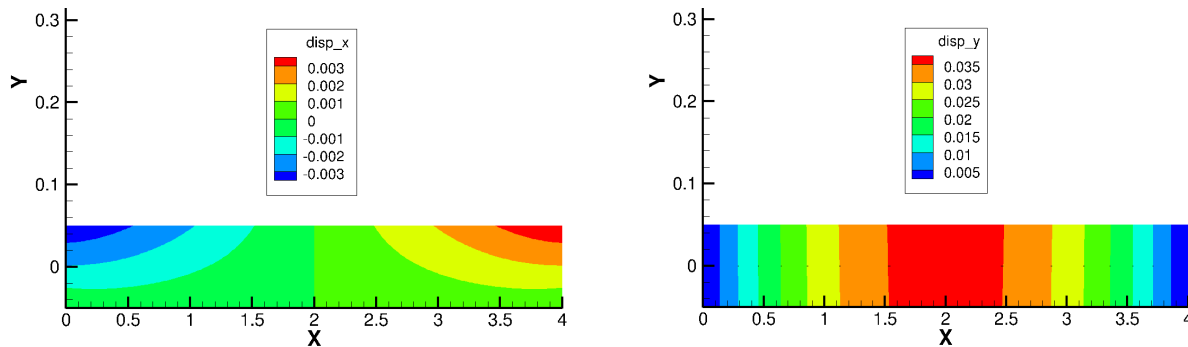
Figure 5-16 Contours of displacement in the x- and y- directions at 30*s,* for the baseline transient aerodynamically heated panel case as calculated by AStrO**.**
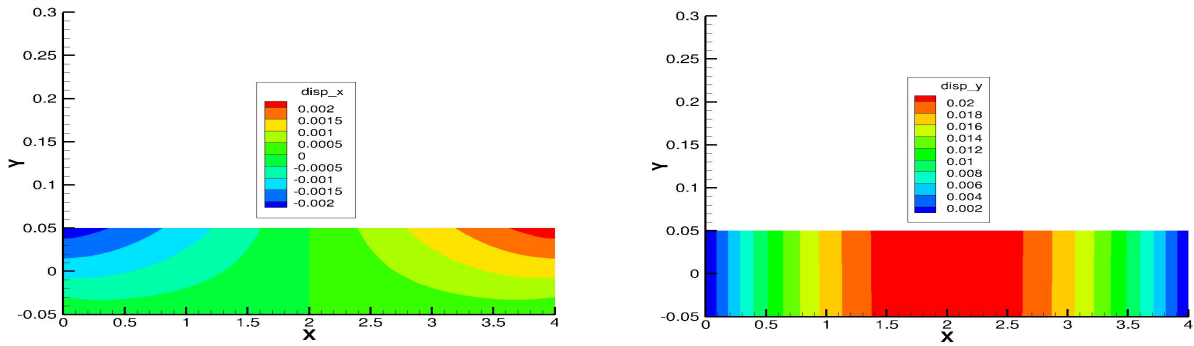
Figure 5-17 Contours of displacement in the x- and y- directions at 30*s,* for the thermo-elastically optimized transient aerodynamically heated panel case as calculated by AStrO.

In order to achieve the minimum displacement in the *x*- and *y*-directions for this panel under the specified boundary conditions, the material properties of the panel are modified by the optimization process. The changes in the design variables, which reflect the changes in the material properties of the panel, are summarized in Table 5-16.

Table 5-16 Changes in the design variables and optimized material properties of the transient aerodynamically heated panel after the thermo-elastic optimization process.

Changes in Design Variable		Optimized Material Properties	
D_1	-0.0187990804614502	Modulus of elasticity (E)	0.35180092×10^8 *lbf/in²*
D_2	0.71999921174524073	Thermal Conductivity (k)	0.200639×10^{-3} *BTU/(s.in.R)*
D_3	-1.9999603748447023	Thermal expansion (α)	4.26433×10^{-6} *1/R*
D_4	0.09991144164202264	Specific heat capacity (C)	$0.1216111 BTU/(lbm.R)$

The convergence of the optimization process for the panel case is shown in Figure 5-18. After 159 optimization cycles the process is terminated due to the bounds put on the design variables.
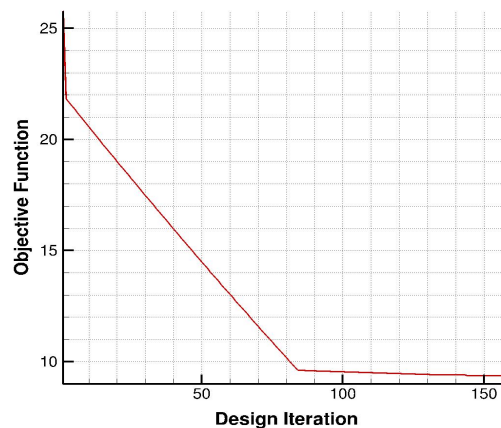
Figure 5-18 Convergence of the thermo-elastic optimization process for the transient aerodynamically heated panel case.

5.2 Aero-Thermo-Elastic Sensitivity Analysis and Optimization Results

In the following section, first the aero-thermo-elastic sensitivities are verified for the tangent and adjoint methods. Next, the verified adjoint sensitivities are used to perform optimizations on a panel in hypersonic flow. The panel problem used for these aero-thermo-elastic sensitivity analysis and optimizations is the same problem that was used in section 5.2.1.2 of the current chapter and in Chapter 3 for validating the aero-thermo-elastic analysis capabilities. For all the optimization cases presented in the coming pages, the SNOPT [113] sequential quadratic programming algorithm is used to drive the constrained optimization.

5.2.1 Aero-Thermo-Elastic Sensitivity Analysis Validation for an Aerodynamically Heated Panel

To verify the aero-thermo-elastic adjoint-based sensitivities, the case of flow with Mach = 0.8 over a panel is considered. The adjoint linearization is verified using the duality relation [85] to the tangent approach, while the tangent sensitivities are verified with the finite-difference method [50, 104]. As mentioned in Chapter 4, simplifications were made for the aero-thermo-elastic sensitivity analysis process since the duality could not be verified for the heat flux sensitivity term. The heat flux sensitivities are not taken into account in the aero-thermo-elastic cases presented in this chapter. Instead, a fixed heat flux is applied on the structure side as a boundary condition which approximates the heat flux from the flow field.

In the thermo-elastic heated panel optimization cases, a function of either the deformation or the temperature of the panel was used as the objective function. For the aero-thermo-elastic problem, aerodynamic based objective functions are considered. Looking through the convergence history of the aero-thermo-elastic analysis problem of the hypersonic heated panel case, it became obvious that the drag coefficient increases as the panel temperature and deformation are increasing. Therefore, we decided to use a function of drag for the aerodynamic objective function.

For this validation, the objective function is based on the drag coefficient. Since the flow has an angle of attack of $15°$, a function of the force coefficient in the x-direction is used as the design variable rather than C_D itself. This is shown in Eq.(5-10).

$$L = (C_x)^2 \tag{5-10}$$

In order to test the adjoint-based sensitivities, the thermal conductivity and thickness of the panel are defined as the design variables as presented in Eq.(5-11).

$$\begin{cases} k = k_0 + 10^{-4}D_1 \\ \\ Thickness = Thickness_{intial} \times D_2 \end{cases} \tag{5-11}$$

The adjoint based sensitivities were verified against the sensitivities calculated by the tangent and finite-difference methods. Table 5-17 and Table 5-18 show a comparison of coupled aero-thermo-elastic sensitivities for flow over the panel obtained from the finite-difference analysis run with those of the tangent and adjoint linearization. Table 5-17 and Table 5-18 show results for the case of using thermal conductivity and thickness of the panel as design variables, respectively. Each table has results for different number of time steps. The sensitivities of the objective function match down to machine precision between the tangent and the adjoint. These sensitivities match reasonably well with the sensitivities calculated through the finite-difference method. As can be seen in both Table 5-17 and Table 5-18, the sensitivity values are increasing with the number of time steps. This is to be expected, since as time passes the panel deforms more and the drag increases.

Table 5-17   Comparison of the sensitivity of the objective function defined in Eq.(5-10) with respect to the design variable D_1 defined in Eq.(5-11), for the aerodynamically heated panel with Mach = 0.8, at different coupling time steps.

Time Step	Adjoint	Tangent	Finite-Difference
1	-3.47763135461256$\times 10^{-6}$	-3.47763135461282$\times 10^{-6}$	-3.6066387221$\times 10^{-6}$
2	-5.31123417602813$\times 10^{-6}$	-5.31123417602895$\times 10^{-6}$	-5.6107710055$\times 10^{-6}$
3	-6.04453180932982$\times 10^{-6}$	-6.04453180933126$\times 10^{-6}$	-7.3720293562$\times 10^{-6}$
5	-6.92850553411629$\times 10^{-6}$	-6.92850553411926$\times 10^{-6}$	-7.6129645635$\times 10^{-6}$

Table 5-18   Comparison of the sensitivity of the objective function defined in Eq.(5-10) with respect to the design variable D_2 defined in Eq.(5-11), for the aerodynamically heated panel with Mach = 0.8 at different coupling time steps.

Time Step	Adjoint	Tangent	Finite-Difference
1	-6.96927382827343$\times 10^{-6}$	-6.96927382827098$\times 10^{-6}$	-7.3292648685$\times 10^{-6}$
2	-2.09733547485967$\times 10^{-5}$	-2.09733547486444$\times 10^{-5}$	-2.2907747595$\times 10^{-5}$
3	-4.19421030208063$\times 10^{-5}$	-4.19421030209051$\times 10^{-5}$	-4.6948589964$\times 10^{-5}$
5	-8.98882633197205$\times 10^{-5}$	-8.98882633195547$\times 10^{-5}$	-10.648608982$\times 10^{-5}$

5.2.2 Aero-Thermo-Elastic Design Optimization for an Aerodynamically Heated Panel with Hypersonic Flow

In this section, the verified sensitivities calculated from the adjoint-based method are applied to an aero-thermo-elastic optimization of the aerodynamically heated panel case with Mach 6.57. The optimization is first performed for one coupled time step. Later, the optimization is repeated taking into account five coupled time steps.

The objective function defined for this problem is shown below:

$$L(t) = (C_x(t_{final}))^2 + n_{element} \times (k_{t_{final}} - (k_{t_{initial}} + 0.000072))^2$$
$$10^{-4} \times (Mass_{t_{final}} - 2.5 \times Mass_{t_{intial}})^2 \quad (5\text{-}12)$$

In Eq.(5-12), a penalty is put on the mass and the thermal conductivity of the panel. The goal in this optimization problem is to minimize the objective function presented in Eq. (5-12) with respect to the thermal conductivity and the thickness of the panel as shown below:

$$\begin{cases} k = k_0 + 10^{-4}D_1 \\ \\ Thickness = Thickness_{intial} \times D_2 \end{cases} \quad (5\text{-}13)$$

5.2.2.1 *Aero-Thermo-Elastic Design Optimization for an Aerodynamically Heated Panel with Mach 6.57, for One Coupled Time Step*

For this optimization problem NSU3D and AStrO are run for only one time step during the optimization process. The optimization was performed using SNOPT. The optimum value of the design variables, which reflect the changes in the material properties of the panel, are summarized in Table 5-19. Table 5-20 shows the change in the objective function from the baseline panel to the aero-thermo-elastically optimized panel case.

Table 5-19 Optimum design variables, initial and optimized material properties of the aerodynamically heated panel with Mach 6.57, with one coupled time step.

Design Variable		Material Properties	Initial Material Properties	Optimized Material Properties
D_1	0.7645006	Thermal Conductivity	0.00012864 *BTU/(s.in.R)*	0.0002059 *BTU/(s.in.R)*
D_2	2.504113	Thickness	1 *in*	2.504113 *in*

Table 5-20 Comparison of the baseline and aero-thermo-elastically optimized objective function for the aerodynamically heated panel with Mach 6.57 with one coupled time step.

	Baseline	Aero-Thermo-elastic optimization
Objective function (Eq. (5-12))	1.6722326×10^{-4}	7.8904212×10^{-5}

The convergence of the optimization process for the panel case is shown in Figure 5-19. The optimization is run for 10 design steps during which the value of the objective function is reduced approximately by a factor of two. The simulations were performed on the Teton supercomputer at University of Wyoming Advanced Research Computing Center (ARCC).
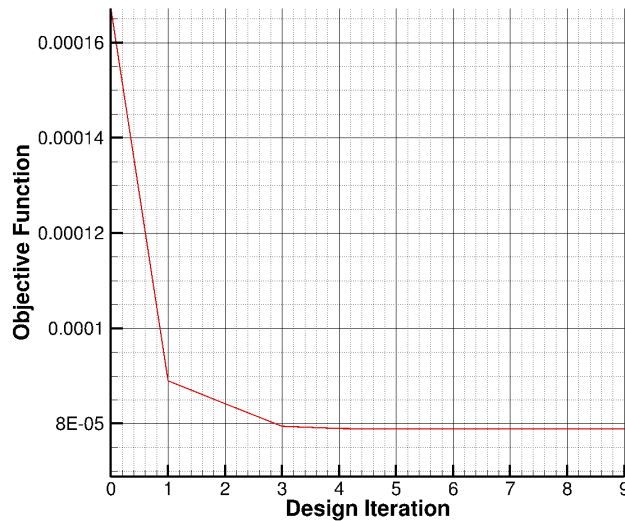
Figure 5-19 Convergence of the aero-thermo-elastic optimization process for the aerodynamically heated panel case with Mach 6.57 with one coupled time step.

5.2.2.2 *Aero-Thermo-Elastic Design Optimization for an Aerodynamically Heated Panel with Mach 6.57, for Five Coupled Time Steps*

For this optimization problem NSU3D and AStrO are run for five time steps during the optimization process. The objective function and design variables are similar to the case with a single time step but correspond to the values at the final time step. Therefore, Eq.(5-12) is used as the objective function and Eq.(5-13) defines the design variables used for this case.

The optimum value of the design variables, which reflect the changes in the material properties of the panel, are summarized in Table 5-21. In addition, Table 5-22 shows the change in the objective function from the baseline panel to the aero-thermo-elastically optimized panel case. Comparing the optimized material properties from Table 5-21 with Table 5-19, it can be observed that the value for the optimized material properties is slightly higher for the optimization using five coupled time steps compared to the optimization using a single time step. This behavior is expected since the aerodynamic term in the objective function is initially large for the case with five time steps. This is similar to the increase in the sensitivities with the number of time steps seen in Table 5-17 and Table 5-18.

99

Table 5-21 Optimum design variables, initial and optimized material properties of the aerodynamically heated panel with Mach 6.57, with five coupled time steps.

Design Variable		Material Properties	Initial Material Properties	Optimized Material Properties
D_1	0.8556365	Thermal Conductivity	0.00012864 BTU/(s.in.R)	0.000214203 BTU/(s.in.R)
D_2	2.5134456	Thickness	1 in	2.5134456 in

Table 5-22 Comparison of the baseline and aero-thermo-elastically optimized objective function for the aerodynamically heated panel with Mach 6.57 with five coupled time steps.

	Baseline	Aero-Thermo-elastic optimization
Objective function (Eq. (5-12))	2.2976563×10^{-4}	1.1060668×10^{-4}

The convergence of the optimization process for the panel case is shown in Figure 5-20. Overall, the convergence of the optimization process is similar for this case compared to the previous case using a single time step. The simulations were performed on the Teton supercomputer at University of Wyoming Advanced Research Computing Center (ARCC).
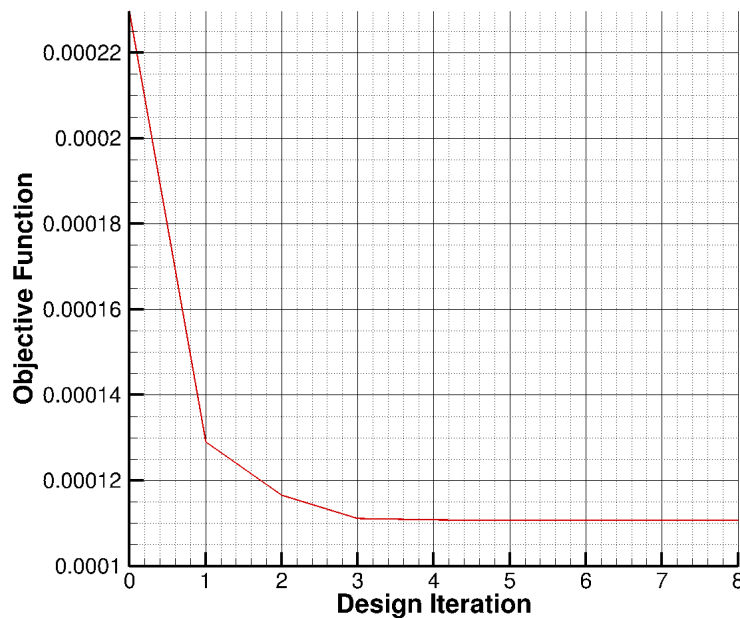
Figure 5-20 Convergence of the aero-thermo-elastic optimization process for the aerodynamically heated panel case with Mach 6.57 with five coupled time steps.

The interaction between the panel deformation and the flow density distributions at $t = 30s$ for the baseline panel design, and the aero-thermo-elastically optimized panel design using five time steps is shown in Figure 5-21 and Figure 5-22, respectively. In these figures, the computed values of density are non-dimensionalized by the free-stream density. The strength of the shocks

and flow disturbances are clearly reduced in the flow over the optimized panel in comparison to the flow over the baseline panel.
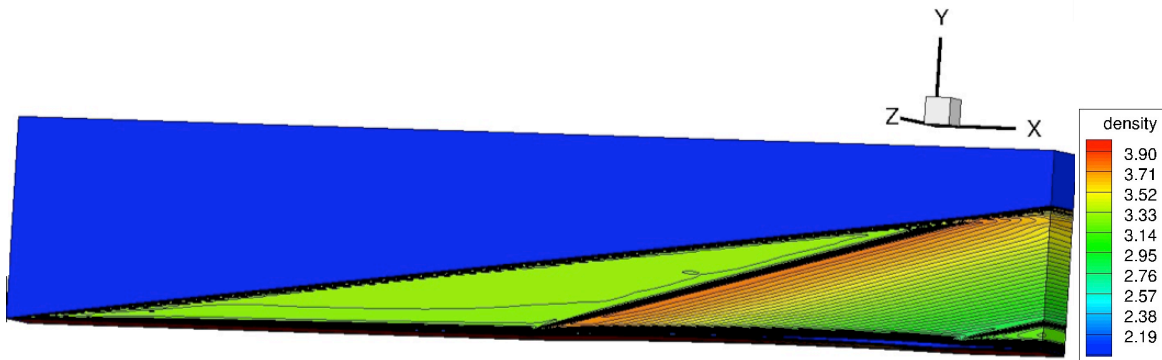
Figure 5-21 Flow density distributions at t = 30*s,* for the baseline panel design.
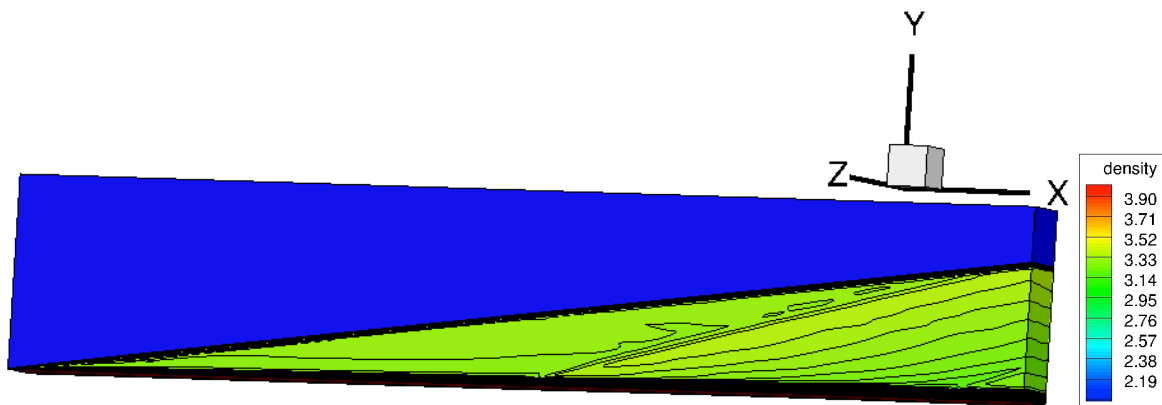
Figure 5-22 Flow density distributions at t = 30*s,* for the aero-thermo-elastically optimized panel design.

5.3 Summary

This chapter outlines a validation of the multi-disciplinary adjoint-based sensitivity analysis capability developed in this dissertation. First, thermo-elastic sensitivities obtained from AStrO are validated. This is followed by a similar effort for the coupled aero-thermo-elastic sensitivities. In each case, the adjoint sensitivities were verified against the tangent sensitivities through the duality property. The sensitivities calculated by the tangent method were verified either against the complex-step method or the finite-difference method. The developed thermo-elastic and aero-thermo-elastic sensitivities were applied to optimization case studies.

6 CONCLUSIONS AND FUTURE WORK

In this chapter a summary of the work done in this dissertation is given. In addition, a discussion of future research possibilities is presented.

6.1 Conclusions

In this dissertation, a high-fidelity, open-source platform for aero-thermo-elastic modeling and adjoint based sensitivity analysis has been developed and validated. Results show the analysis capability to be reliable, and the adjoint-based sensitivities to be consistent with direct differentiation. Also, preliminary adjoint-based optimization results are very promising.

The first half of this research focused on creating a platform for aero-thermo-elastic analysis. This platform was created using the following modules developed previously in-house: the flow solver NSU3D, the thermo-elastic capability from the structural solver AStrO, the FSI module, and the mesh deformation capability. A weak coupling approach was used to take advantage of these in-house solvers. For this purpose, the fluid structure interaction module developed in-house for aero-elastic analysis, was further extended for use in the aero-thermal data transfer. The heat transfer solver and the thermo-elastic capabilities of AStrO were thoroughly validated before moving on to implementing the aero-thermo-elastic platform. Finally, the transient aero-thermo-elastic analysis capability was verified through two applications: hypersonic flow over a cylindrical leading edge, and an aerodynamically heated panel. In these test cases, the analysis results from the developed framework were compared with available experimental results, analytical solutions, and previous computational results. A good agreement was seen overall.

In the second part of this work, the loosely coupled, three-dimensional, aero-thermo-elastic analysis platform, which consists of high-fidelity solvers for each discipline, was further developed for design optimization. The sensitivity derivatives were calculated using the discrete adjoint approach. This method was chosen since it is the most efficient method for calculating sensitivities for a large number of design variables in multi-disciplinary optimization problems. The main challenge here centered around the development of the corresponding disciplinary sensitivities and their coupling. NSU3D's aerodynamic sensitivities have been implemented and validated in previous work. Hence, the first step in this study was to thoroughly validate AStrO's thermo-elastic adjoint sensitivities. The next step was to formulate, implement, and verify the coupled aero-thermo-elastic sensitivities. The aero-elastic sensitivities have been coupled successfully. However, for the aero-thermal sensitivities, duality could not be verified for the heat flux term. Therefore, in order to conduct aero-thermo-elastic optimization the heat flux term was omitted from the sensitivity analysis. Even with this simplification, reasonable optimization results were produced using the developed platform.

The developed aero-thermo-elastic analysis and design platform should enable many opportunities for future research in understanding the physics in high-speed flows and hypersonic vehicle design. This was demonstrated through multiple high-speed validation test cases throughout this research. Hypersonic platforms are important for both military and civilian applications. However, despite over six decades of research activity, many of the initial goals such as sustainable hypersonic flight has still not been reached. The availability of reliable and high-fidelity aero-thermo-elastic analysis and design codes will help advance this field of research. These codes are needed due to the absence of experimental facilities that would help characterize the behavior of aero-thermo-elastic systems in hypersonic speeds.

Moreover, this work highlights the benefits of open-source tools, mainly enabling users to interface different codes for performing efficient multi-disciplinary analysis, including calculating adjoint sensitivities for multi-physics problems with significant coupling. In addition, the flexibility of open-source tools allows for any objective function or design variable to be defined and differentiated using the adjoint-based sensitivity method.

6.2 Future Work

This work provides multiple avenues for future research and development. These include stand-alone solver development as well as future research related to the betterment of the coupled framework. A non-exhaustive list for advancing this work is provided hereafter.

1. Coupled aero-thermo-elastic sensitivity development - In this work, simplifications were made in the coupled aero-thermo-elastic sensitivity analysis and optimization process. In the analysis problem, the heat flux is passed from the fluid domain to the structure domain. However, in the tangent problem the heat flux sensitivity coupling is omitted. Similarly, for the adjoint problem, the heat flux adjoint is not passed from the structure domain to the fluid domain. Instead, a fixed heat flux is applied on the structure domain. This was done since duality could not be verified for the implemented heat flux terms. This simplification has provided the means to conduct aero-thermo-elastic optimization with the current platform. However, for a fully coupled aero-thermo-elastic sensitivity analysis, the platform needs to take the heat flux sensitivities into account. Therefore, the most important next step will be to verify the duality for the heat flux term in order to include that term in the sensitivity analysis and optimization process.

2. Fluid solver development- Despite advancements in numerical analysis, a current shortcoming in computational fluid dynamics is the lack of robust and efficient implementation of real gas effects. Currently, NSU3D considers the flow medium as a perfect gas in the numerical simulation. This is the case in many of the aero-thermal and aero-thermo-elastic simulation platforms in the literature. This is because accounting for non-equilibrium real gas

effects is a computationally challenging task. Adding real gas effects in NSU3D would allow it to produce more accurate and reliable results.

3. Structural solver development- There are a couple of changes that could be made to AStrO in order to increase its accuracy and efficiency. Currently, AStrO has no parallel implementation. Although parallelizing AStrO has been a long-term goal from the beginning, the priority to date has been on development of the fundamental tools. In this work, the main goal was coupling AStrO with NSU3D for aero-thermo-elastic simulations. However, looking forward to the future, parallelizing AStrO would add to the efficiency of the code. In addition, including radiation effects and material variations with temperature in the code would expand its capability.

4. Fluid Structure Interaction (FSI) module development- In this research, a node-projection scheme is used for the transfer of data between the fluid and structure domains. The node-projection scheme was used because it is a conservative scheme, which helps with the stability of the simulation. In addition, we already had a previously validated FSI module for aero-elastic simulations that had been used in earlier works. This module was extended to also transfer heat fluxes and temperatures for aero-thermal simulations. Although, the aero-thermo-elastic platform has been validated through multiple examples, it would be of great benefit if in the future the FSI module could be further developed with the goal of increased accuracy. One option could be to use the common-refinement scheme presented briefly in Chapter 2. The common refinement method is quite complex to implement in three-dimensional and to parallelize. That is why we decided to expand on the already implemented node-projection FSI module for this work.

5. Adaptive coupling time step size- In this dissertation, a fixed coupling time step size has been used. So far, this step size has been the structural solver's step size which is controlled by the thermal problem. However, there usually is a rapid change at the start of the simulation between the aerodynamic heating and structural heat transfer, suggesting that a small coupling time step size is only required initially, and then the coupling time step size could be gradually increased according to the real physical evolution. Therefore, an adaptive coupling time step size approach will most probably achieve a further reduction in computational costs. This would add to the computational efficiency of the aero-thermo-elastic simulation platform.

6. Uncertainty Quantification (UQ) and Reduced-Order Modeling (ROM)- The verified aero-thermo-elastic sensitivities have the potential to be used for uncertainty quantification. In addition, these sensitivities can be used to build better reduced order models. An aero-thermo-elastic simulation using coupled high-fidelity fluid and structural solvers presents a substantial computational burden. This computational burden comes from the presence of different time

scales, different mesh resolutions, a large number of degrees of freedom, and the necessity of performing a large number of repeated analysis cycles. These issues have motivated research in ROM. This type of modeling aims to reduce the computational cost of the system, while maintaining acceptable accuracy. For hypersonic aero-thermo-elastic analysis, a ROM model could cost a fraction of the full-order model. Therefore, using the aero-thermo-elastic sensitivities verified in this work for building better ROM models, will be beneficial.

These are only a few possibilities for future advancement. The hope is that as time passes with future development this platform will become a versatile toolset for high-fidelity multi-disciplinary modeling and optimization which will contribute to the future of engineering simulation and design.

REFERENCES

[1]   Pironkov, P."Numerical Simulation of Thermal Fluid-Structure Interaction," Master of Science thesis, university, Darmstadt, 2010.

[2]   ESA."European Aeronautics: A vision for 2020," ESA, 2001.

[3]   Strategic Implementation Plan," Aeronautics, N., NASA, 2017.

[4]   Slotnich, J., Alonso, J., Darmofal, D., Gropp, W., Lurie, E., and Mavriplis, D. J."CFD Vision 2030 Study: A path to Revolutionary Computational Aerosciences," Center, L. R., NASA, Langley Research Center, Hampton, Virginia, 2014.

[5]   Kamali, S., Mavriplis, D. J., and Anderson, E. "Development and Validation of a High-Fidelity Aero-Thermo-Elastic Analysis Capability," AIAA SCITECH 2020 Forum, Conference, Location, 2020. doi: 10.2514/6.2020-1449

[6]   Polle, D., Allen, C., and Rendall, T. "A Constrained Global Optimization FrameWork," 14th AIAA Aviation Technology , Integraiton, and operations conference, Conference, Location, 2014,

[7]   Jameson, A. "Aerodynamic Design via Control Theory," *Journal of Scientific Computing* Vol. 3, No. 3, 1988, pp. 233-260.

[8]   Jameson, A., Martinelli, L., and Pierce, N. A. "Optimum aerodynamic design using the Navier-Stokes equations," *Theoretical and Computational Fluid Dynamics* Vol. 10, No. 1-4, 1998, pp. 213-237. doi: 10.1007/s001620050060

[9]   Witherden, F., D.;Jameson,A. "Future Directions of Computational Fluid Dynamics," 23rd AIA Computational Fluid Dynamics Conference, Conference, Location, 2017,

[10]   Fife, M., E.;Davis,R,L. "A Conjugate Heat Transfer RANS/DES Simulation Procedure," 47th AIAA Aerospace Sciences meeting including the new horizons forume and erospace exposition, Conference, Location, 2009,

[11]   Nordstrom, J., and Berg, J. "Conjugate heat transfer for the unsteady compressible Navier-Stokes equations using a multi-block coupling," *Computers & Fluids* Vol. 72, 2013, pp. 20-29. doi: 10.1016/j.compfluid.2012.11.018

[12]   Errera, M. P., and Baque, B. "A quasi-dynamic procedure for coupled thermal simulations," *International Journal for Numerical Methods in Fluids* Vol. 72, No. 11, 2013, pp. 1183-1206. doi: 10.1002/fld.3782

[13]   Reinert, J. D., Dwivedi, A., and Candler, G. V. "Verification of a conjugate heat transfer tool with US3D," AIAA Scitech 2019, Conference, Location, 2019. doi: 10.2514/6.2019-1892

[14]   Seager, C., and Agarwal, R. K. "Hypersonic Blunt-Body Shape Optimization for Reducing Drag and Heat Transfer," *Journal of Thermophysics and Heat Transfer* Vol. 31, No. 1, 2017, pp. 48-55. doi: 10.2514/1.t4650

[15]   Dechaumphai, P., Thornton, E. A., and Wieting , A. R."Fluid-Thermal-structural Study of Aerodynamically Heated Leading Edges," NASA Technical Memorandum, NASA, Langley Research Center , Hampton, Virginia, 1988.

[16]   Zhao, X., Sun, Z., Tang, L., and Zheng, G. "Coupled Flow-Thermal-Structural Analysis of Hypersonic Aerodynamically Heated Cylindrical Leading Edge,"

Engineering Applications of Computational Fluid Mechanics Vol. 5, No. 2, 2011, pp. 170-179. doi: 10.1080/19942060.2011.11015361

[17]   Maute, K., Nikbay, M., and Farhat, C. "Coupled analytical sensitivity analysis and optimization of three-dimensional nonlinear aeroelastic systems," *AIAA Journal* Vol. 39, No. 11, 2001, pp. 2051-2061. doi: 10.2514/2.1227

[18]   Jaiman, R. K., Jiao, X., Geubelle, P. H., and Loth, E. "Assessment of conservative load transfer for fluid-solid interface with non-matching meshes," *International Journal for Numerical Methods in Engineering* Vol. 64, No. 15, 2005, pp. 2014-2038. doi: 10.1002/nme.1434

[19]   Jiao, X. M., and Heath, M. T. "Common-refinement-based data transfer between non-matching meshes in multiphysics simulations," *International Journal for Numerical Methods in Engineering* Vol. 61, No. 14, 2004, pp. 2402-2427. doi: 10.1002/nme.1147

[20]   Cebral, J., and Loehner, R. "Conservative load projection and tracking for fluid-structure problems," 34th Aerospace Science meething and exhibit, Conference, Location, 1996. doi: 10.2514/6.1996-797

[21]   Cebral, J., and Lohner, R. "conservative load projection and tracking for fluid-structure problems," *AIAA Journal* Vol. 35, No. 4, 1997, pp. 687-692. doi: 10.2514/2.158

[22]   Wieting, A. R., Dechaumphai , P., Bey, K. S., Thornton, E., A, and Morgan , K. "Application of integrated Fluid-Thermal-Structural Analysis Methods," *Thin-Walled Structures* Vol. 11, No. 1-2, 1991, pp. 1-23. doi: 10.1016/0263-8231(91)90008-7

[23]   Zhang, S., Chen, F., and Liu, H. "Time-Adaptive, Loosely Coupled Strategy for Conjugate Heat Transfer Problems in Hypersonic Flows," *Journal of Thermophysics and Heat Transfer* Vol. 28, No. 4, 2014, pp. 635-646. doi: 10.2514/1.t4278

[24]   Zhao, X., Sun, Z., Tang, L., and Zheng, G. "Coupled Flow-Thermal-Structural Analysis of Hypersonic Aerodynamically Heated Cylindrical Leading Edge," *Engineering Applications of Computational Fluid Mechanics* Vol. 5, No. 2, 2014, pp. 170-179. doi: 10.1080/19942060.2011.11015361

[25]   Thornton, E., and Dechaumphai, P. "Coupled flow, thermal and structural analysis of aerodynamically heated panels," 1987. doi: 10.2514/6.1987-700

[26]   Thornton, E., A., and Dechaumphai , P. "Coupled Flow, Thermal, and Structural Analysis of Aerodynamically Heated Panels," *Journal of aircraft* Vol. 25, No. 11, 1988. doi: 10.2514/3.45702

[27]   Thornton, E., and Dechaumphai, P. "Finite element prediction of aerothermal-structural interaction of aerodynamically heated panels," 1987. doi: 10.2514/6.1987-1610

[28]   Lohner, R., Yang, C., Cerbal, J., Baum, J., Luo, H., Pelessone, D., and Charman, C. "Fluid-structure-thermal interaction using a loose coupling algorithm and adaptive unstructured grids," 1998. doi: 10.2514/6.1998-2419

[29]   McNamara, J. J., and Friedmann, P. P. "Aeroelastic and Aerothermoelastic Analysis in Hypersonic Flow: Past, Present, and Future," *AIAA Journal* Vol. 49, No. 6, 2011, pp. 1089-1122. doi: 10.2514/1.j050882

[30]   Kamali, S., Mavriplis, D. J., and Anderson, E. "Sensitivity Analysis for Aero-Thermo-Elastic Problems Using the Discrete Adjoint Approach," AIAA Aviation 2020 Forum, Conference, Location, 2020. doi: 10.2514/6.2020-3138

[31]   Reinert, J. D., Nompelis, I., and Candler, G. V. "Coupled conjugate heat transfer simulation for a scramjet inlet at Mach 8," 23rd AIAA Computatonal Fluid Dynamics Conference, Conference, Location, 2017. doi: 10.2514/6.2017-4502

[32]   Smith, L. J., Halim, L. J., Kennedy, G., and Smith, M. J. "A High-Fidelity Coupling Framework for Aerothermoelastic Analysis and Adjoint-Based Gradient Evaluation," AIAA Scitech 2021 Forum, Conference, Location, 2021. doi: 10.2514/6.2021-0407

[33]   Zope, A., D, Schemmel, A., Bhtia, M., Bhushan, S., and Collins, E. "Development and Validation of Fluid-Thermal Interaction Solver for High Fidelity Transient Simulations," AIAA Aviation, Conference, Location, 2020,

[34]   Xia, C., and Chen, W. "Gradient-based Aerothermodynamic Optimization of a Hypersonic Wing Profile," *Procedia Engineering* Vol. 126, 2015, pp. 189-193. doi: 10.1016/j.proeng.2015.11.214

[35]   Vassbert, J., C, and Jameson, A."Industrial Applications of Aerodynamic Shape Optimization," Von Karman Institute, Brussels, Belgium, 2014.

[36]   Sobieszczanski-Sobieski, J., and Haftka, R. T. "Multidisciplinary aerospace design optimization: survey of recent developments," *Structural Optimization* Vol. 14, No. 1, 1997, pp. 1-23. doi: 10.1007/bf01197554

[37]   Schmit, L., A."Structural Synthesis- Precursor and Catalyst," Recent Experiences in Multidisciplinary Analysis and Optimization Part 1, NASA Langley Research Cennter, 1984.

[38]   Haftka, R. T., and Shore, C., P."Approximation Methods for Combined Thermal/Structural Design," NASA Technical Paper 1428, NASA Langley Research Center, Hampton, Virginia, 1979.

[39]   Haftka, R. T."Automated Procedure for Design of Wing Structures to Satisfy Strenght and Flutter Requirements," NASA Langley Research Center, National Aeronautics and Space Administeration, Washington, D . C, 1973.

[40]   Haftka, R. T. "Optimization of Flexible Wing Structures Subject to Strength and Induced Drag Constraints," *AIAA Journal* Vol. 15, No. 8, 1977. doi: https://doi.org/10.2514/3.7400

[41]   Haftka, R. T. "Structural Optimization with Aeroelastic Constraints - A Survey of U.S. Applications," *International Journal of Vehicle Design* Vol. 7, No. 3-4, 1986, pp. 381-392.

[42]   Anderson, E."Development of an Open-Source Capability for High-Fidelity Thermoelastic Modeling and Adjoint-Based Sensitivity Analysis of Structures," Ph.D Dissertation, Mehcnaical Engineering, university, Laramie, Wyoming, 2019.

[43]   Martins, J., R, Alonso, J., and Reuther, J., J. "Aero-Structtural Wing Design Optimization Using High-Fidelity Sensitivity Analysis," *Proceedings of the CEAS Conference on Multidisciplinary Aircraft Design and Optimization*. Koln , Germany, 2001.

[44]   Kenway , G. K. W., and Martins, J. "Multipoint High-Fedility Aerostructural Optimization of a Transport Aircraft Configuration," *Journal of Aircraft* Vol. 51, No. 1, 2014, pp. 144-160. doi: 10.2514/1.C032150

[45]   Mani, K., and Mavriplis, D. J. "Adjoint-Based Sensitivity Formulation for Fully Coupled Unsteady Aeroelasticity Problems," *AIAA Journal* Vol. 47, No. 8, 2009, pp. 1902-1915. doi: 10.2514/1.40582

[46]   Mani, K."Application of Discrete Adjoint Method to Coupled Multidisciplinary Unsteady Flow Problems for Error Estimation and Optimization," Doctor of Philosophy, Department of Mechanical Engineering, university, Laramie, Wyoming, 2009.

[47]   Mavriplis, D. J., Anderson, E., Fertig, R., and Garnish, M. "Development of a High-Fidelity Time-Dependent Aero-Structural Capability for Analysis and design," 57th AIAA/ASCE/AHS/ASC Structures, Structural Dynamics, and Materials Conference, AIAA SciTech Forum, Conference, Location, 2016. doi: 10.2514/6.2016-1175

[48]   Mavriplis, D. J., Fabiano, E., and Anderson, E. "Recent Advances in High-Fidelity Multidisciplinary Adjoint-Based Optimization with the NSU3D Flow Solver Framework," 55th AIAA Aerospace Sciences Meeting, Conference, Location, 2017. doi: 10.2514/6.2017-1669

[49]   Zhang, Z., J, and Zingg, D. "Efficient Monolithic Solution Algorithm for High-Fidelity Aerostructural Analysis and Optimiation," *AIAA Journal* Vol. 56, No. 3, 2018.

[50]   Anderson, E., Bhuiyan, F. H., Mavriplis, D. J., and Fertig, R. "Adjoint-Based High-Fidelity Aeroelastic Optimization of Wind Turbine Blade for Load Stress Minimization," Wind Energy Symposium, AIAA SciTech Forum Conference, Location, 2018. doi: 10.2514/6.2018-1241

[51]   Padway, E."Tangent and Adjoint Problems in Partially Converged Flows," Ph.D Dissertation, Mechanical Engineering, university, Laramie, Wyoming, 2020.

[52]   Nielsen, E. J., and Anderson, W. K. "Aerodynamic design optimization on unstructured meshes using the Navier-Stokes equations," *AIAA Journal* Vol. 37, No. 11, 1999, pp. 1411-1419. doi: 10.2514/2.640

[53]   Miller, B., A."Loosely Coupled Time Integration of Fluid-Thermal-Structural Interactions in Hypersonic Flows," Ph.D Dissertation, Aeronautical and Astronautical Engineering, university, 2015.

[54]   Farhat, C., van der Zee, K. G., and Geuzaine, P. "Provably second-order time-accurate loosely-coupled solution algorithms for transient nonlinear computational aeroelasticity," *Computer Methods in Applied Mechanics and Engineering* Vol. 195, No. 17-18, 2006, pp. 1973-2001. doi: 10.1016/j.cma.2004.11.031

[55]   Roe, B., Jaiman, R., Haselbacher, A., and Geubelle, P. H. "Combined interface boundary condition method for coupled thermal simulations," *International Journal for Numerical Methods in Fluids* Vol. 57, No. 3, 2008, pp. 329-354. doi: 10.1002/fld.1637

[56]   Roe, B., Haselbacher, A., and Geubelle, P. H. "Stability of fluid-structure thermal simulations on moving grids," *International Journal for Numerical Methods in Fluids* Vol. 54, No. 9, 2007, pp. 1097-1117. doi: 10.1002/fld.1416

[57]   Duchaine, F., Corpron, A., Pons, L., Moureau, V., Nicoud, F., and Poinsot, T. "Development and assessment of a coupled strategy for conjugate heat transfer with Large Eddy Simulation: Application to a cooled turbine blade," *International Journal of Heat and Fluid Flow* Vol. 30, No. 6, 2009, pp. 1129-1141. doi: 10.1016/j.ijheatfluidflow.2009.07.004

[58]   Zhang, Q. C., S. *Multiphysics Modeling:Numerical Methods and Engineering Applications*, Joe Hayton, Oxford, UK, 2016.

[59] Lassaux, G. D., S.;Descamps,L.;Moteurs,S."Conjugate Heat Transfer Analysis of a Tri-Dimensional Turbine Blade Internal Cavity," department, T. A. a. M. D., centre de villaroche, Moissy-Cramayel , France.

[60] Montenay.A.;Pate, L. D., J.M. "Conjugate Heat Tranfer Analysis of An Engine Internal Cavity," International Gas Turbine and Aeroengine Congress and Exhibition, Conference, Location, 2000,

[61] Li, Y. L., Law, Y. Z., Joshi, V., and Jaiman, R. K. "3D common-refinement method for non-matching meshes in partitioned variational fluid-structure analysis," Conference, Location, 2017. doi: 10.1016/j.jcp.2018.05.023

[62] Verstraete, T., Alsalihi, Z., and Van den Braembussche, R. A. "Numerical Study of the Heat Transfer in Micro Gas Turbines," *Journal of Turbomachinery* Vol. 129, No. 4, 2007, p. 835. doi: 10.1115/1.2720874

[63] Verstraete, T., Alsalihi, Z., and Van den Braembussche, R. A. "A comparison of conjugate heat transfer methods applied to an axial helium turbine," *Proceedings of the Institution of Mechanical Engineers, Part A: Journal of Power and Energy* Vol. 221, No. 7, 2007, pp. 981-989. doi: 10.1243/09576509jpe385

[64] Farhat, C. L., M.;LeTallec,P. "load and motion transfer algorithms for fluid/structure interaction problems with non-matching discrete interfaces:momentum and energy conservation, optimal discretization and application to aeroelasticity," *Computational methods in applied mechanics and engineering* Vol. 157, No. 1-2, 1998.

[65] Heidmann, J., D. "Conjugate heat transfer effects on a realistic film-cooled turbine vane," *Proceedings of the ASME Turbo Expo 2003* Vol. 5, 2003, pp. 361-371.

[66] Giles, M. B. "Stability analysis of numerical interface conditions in fluid-structure thermal analysis," *International Journal for Numerical Methods in Fluids* Vol. 25, No. 4, 1997, pp. 421-436. doi: 10.1002/(Sici)1097-0363(19970830)25:4<421::Aid-Fld557>3.0.Co;2-J

[67] Godunov S, K., and Ryabenkii V, S. *The Theory of Difference Schemes- An Introduction* North-Holland, Amsterdam, 1964.

[68] Roux, F. X., and Garaud, J. D. "Domain Decomposition Methodology with Robin Interface Matching Conditions for Solving Strongly Coupled Fluid-Structure Problems," *International Journal for Multiscale Computational Engineering* Vol. 7, No. 1, 2009, pp. 29-38.

[69] Jaiman, R. K., Jiao, X., Geubelle, P. H., and Loth, E. "Conservative load transfer along curved fluid-solid interface with non-matching meshes," *Journal of Computational Physics* Vol. 218, No. 1, 2006, pp. 372-397. doi: 10.1016/j.jcp.2006.02.016

[70] Jaiman, R., Geubelle, P., Loth, E., and Jiao, X. "Transient fluid-structure interaction with non-matching spatial and temporal discretizations," *Computers & Fluids* Vol. 50, No. 1, 2011, pp. 120-135. doi: 10.1016/j.compfluid.2011.07.001

[71] Samareh, J., A. "Discrete Data Transfer Technique for Fluid-Structure Interaction," 18th AIAA Computational Fluid Dynamics Conference, Conference, Location, 2007. doi: 10.2514/6.2007-4309

[72] Jiao, X. H., T,M. "overlaying surgace meshes, part I: Algorithms," *International journal of computational geometry and applications* Vol. 14, No. 6, 2004.

[73]   Mavriplis, D. J. "Discrete Adjoint-Based Approach for Optimization Problems on Three-Dimensional Unstructured Meshes," *AIAA Journal* Vol. 45, No. 4, 2007, pp. 741-750. doi: 0.2514/1.22743

[74]   Mavriplis, D. J., and Mani, K. "Unstructured Mesh Solution Techniques using the NSU3D Solver," 52nd Aerospace Sciences Meeting, Conference, Location, 2014. doi: 10.2514/6.2014-0081

[75]   Vassberg, J. C., Tinoco, E. N., Mani, M., Zickuhr, T., Levy, D., Broderson, O. P., Eisfeld, B., Wahls, R. A., Morrison, J. H., Mavriplis, D. J., and Murayama, M. "Summary of the Fourth AIAA CFD Drag Prediction Workshop," AIAA, Conference, Location, 2010. doi: 10.2514/6.2010-4547

[76]   Vassberg, J. C., Tinoco, E. N., Mani, M., Broderson, O. P., Eisfeld, B., Wahls, R. A., Morrison, J. H., Zickuhr, T., Laflin, K. R., and Mavriplis, D. J. "Abridged Summary of the Third AIAA Computational Fluid Dynamics Drag Prediction Workshop," *Journal of Aircraft* Vol. 45, No. 3, 2008, pp. 781-798. doi: 10.2514/1.30572

[77]   Mavriplis, D. J., Yang, Z., and Long, M. "Results Using NSU3D for the First Aeroelastic Prediction Workshop," 51st AIAA Aerospace Sciences Meeting, Conference, Location, 2013. doi: 10.2514/6.2013-786

[78]   Mavriplis, D. J., Long, M., Lake, T., and Langlois, M. "NSU3D Results for the Second AIAA High-Lift Prediction Workshop," 52nd AIAA Aerospace Sciences Meeting, Conference, Location, 2014. doi: 10.2514/6.2014-0748

[79]   Mavriplis, D. J. "Solution of the Unsteady Discrete Adjoint for Three-Dimensional Problems on Dynamically Deforming Unstructured meshes," Proceedings of the 46th Aerospace Sciences Meeting and Exhibit, Conference, Location, 2008. doi: 10.2514/6.2008-727

[80]   Mani, K., and Mavriplis, D. J. "Geometry Optimization in Three-Dimensional Unsteady Flow Problems using the Discrete Adjoint," 51st AIAA Aerospace Sciences Meeting, Conference, Location, 2013. doi: 10.2514/6.2013-662

[81]   Roe, P. L. "Approximate Riemann Solvers Parameter Vectors and Difference Schemes," *Journal of Computational Physics* Vol. 43, No. 2, 1981, pp. 357-372. doi: 10.1016/0021-9991(81)90128-5

[82]   "Abaqus," Version 6.14-4 ed., product of Dassault Systems Simulia Corp, Providence,RI,USA, 2017.

[83]   Hilber, H. M., Hughes, T. J. R., and Taylor, R. L. "Improved Numerical Dissipation for Time Integratoin Algorithms in Structural Dynamics," *Earthquake Engng Struct. Dynamics* Vol. 5, 1977, pp. 283-292. doi: 10.1002/eqe.4290050306

[84]   Reddy, J. N. *Energy Principles and Variational Methods in Applied Mechanics*, John Wiley & Sons, New Jersey , USA, 2002.

[85]   Nocedal, J., and Wright, S. *Numerical Optimization*, Springer, Verlag, NY, 1999.

[86]   Joshi, O., and Leyland, P. "Stability Analysis of a Partitioned Fluid–Structure Thermal Coupling Algorithm," *Journal of Thermophysics and Heat Transfer* Vol. 28, No. 1, 2014, pp. 59-67. doi: 10.2514/1.t4032

[87]   Roget, B., and Sitaraman, J. "Wall distance search algorithm using voxelized marching spheres," *Journal of Computational Physics* Vol. 241, 2013, pp. 76-94. doi: 10.1016/j.jcp.2013.01.035

[88] Donea, J., Huerta, A., and Ponthot, J. *Encyclopedia of Computational Mechanics*, 2004.

[89] Thomas, P., D., and Lombard, C., K. "Geometric Consevation Law and its Application to Flow Computations on Moving Grids," *AIAA Journal* Vol. 17, No. 10, 1970, pp. 1030-1037. doi: 10.2514/3.61273

[90] Yang, Z., and Mavriplis, D. J. "A Mesh Deformation Strategy Optimized by the Adjoint Method on Unstructured Meshes," 45th AIAA Aerospace Sciences Meeting and Exhibit, Conference, Location, 2007. doi: 10.2514/6.2007-557

[91] Yang, Z., and Mavriplis, D. J. "Higher-Order Time Integration Schemes for Aeroelastic Applications on Unstructured Meshes," *AIAA Journal* Vol. 45, No. 1, 2007, pp. 138-150. doi: 10.2514/1.22847

[92] Bird, R. B., Stewart, W. E., and Lightfoot, E. N. *Transport Phenomena*, Wiley, 2014.

[93] Beck, V. J., Blackwell, B. F., and Clair, C. R. S. *Inverse Heat Conduction Problems*, Wiley-interscience, New York, NY, 1985.

[94] Arpaci, V. S. *Conduction Heat Transfer*, Addison-Wesley, Reading, MA, 1966.

[95] Bejan, A. *Heat Transfer*, John Wiley and Sons, 1993.

[96] Wieting., A. R."Experimental Study of Shock Wave Interference Heating on a Cylindrical Leading Edge," Ph.D. Disseration, Mechanical Engineering, university, Norfolk, Virgina, 1987.

[97] Dechaumphai , P., Thornton, E., A, and Wieting, A., R. "Flow-Thermal-Structural Study of Aerodynamically Heated Leading Edges," *Journal of Spacecraft and Rockets* Vol. 26, No. 4, 1989, pp. 201-209. doi: 10.2514/3.26055

[98] Fay, J. A., and Riddell, F. R. "Theory of Stagnation Point Heat Transfer in Dissociated Air," *Journal of the Aeronautical science* Vol. 25, No. 2, 1958. doi: 10.2514/8.7517

[99] Holcomb, J. E., Curtis, J. T., and Shope, F. L."A New Version of the CVEQ Hemisphere Viscous Shock Layer Problem for Equilibrium Air," Center, A. E. D., Arnold Air Force Station, 1985.

[100] Fabiano, E."Multidisciplinary Adjoint-based Optimization Technicques for Helicopter Rotrs " Doctor of Philosophy, Department of Mechanical Engineering, university, Laramie, Wyoming.

[101] Poole, D. J., Allen, C. B., and Rendall, T. "Comparison of Local and Global Constrained Aerodynamic Shape Optimization," 32nd AIAA Applied Aerodynamis Conference, Conference, Location, 2014. doi: 10.2514/6.2014-3223

[102] Newman, J. C., Taylor, A. C., Barnwell, R. W., Newman, P. A., and Hou, G. J. W. "Overview of sensitivity analysis and shape optimization for complex aerodynamic configurations," *Journal of Aircraft* Vol. 36, No. 1, 1999, pp. 87-96. doi: 10.2514/2.2416

[103] Mishra, A., Mani, K., Mavriplis, D. J., and Sitraman, J. "Time Dependent Adjoint-based Optimization for Coupled Aeroelastic Problems," 21st AIAA CFD Conference, Conference, Location, 2013,

[104] Newman, C., James III, Anderson, W. K., and Whitfield, D. L."Multidisciplinary Sensitivity Derivatives Using Complex Variables," Computational Fluid Dynamics Laboratory, N. E. R. C. f. C. F. S., Mississippi State University, Mississipi, USA, 1998.

[105] Mousavi, S., A."Constrained Aerodynamics and Heat Transfer Optimizaiton of Gas Turbine Blades Using an Adjoint Approach," Ph.D. Disseration, Department of Mechanical Engineering, university, Motreal, Quebec, 2012.

[106] Pironneau, O. "On Optimum Design in Fluid Mechanics," *Journal of Fluid Mechanics* Vol. 64, No. 1, 1974, pp. 97-110.

[107] Jameson, A. "Optimum Aerodynamic Design Using Control Theory," 1995.

[108] Mavriplis, D. J."Time Dependent Adjoint Methods for Single and Multi-Disciplinary Problems," Von Karman Institute for Fluid Dynamics Lecture Series, Von Karman Institute for Fluid Dynamics.

[109] Giles, M. B., Duta, M., C, and Muller, J., D. "Adjoint Code Development Using the Exact Discrete Approach," 15th Computatoinal Fluid Dynamic Conference, Conference, Location, 2001,

[110] Mavriplis, J., Dimitri."Time Dependent Adjoint Methods for Single and Multi-disciplinary Problems," Engineering, D. o. M., University of Wyoming, Laramie, Wyoming, USA, 2015.

[111] Mishra, A., Mavriplis, D. J., and Sitraman, J. "Time-depedent Aero-elastic Adjoint-based Aerodynamic Shape Optimization of Helicopter Rotors in Forward Flight," *AIAA Journal* Vol. 54, No. 12, 2016, pp. 3813-3827. doi: 10.2514/1.J054962

[112] Shi, S., Dai, C., and Wang, Y. "Design and optimization of an integrated thermal protection system for space vehicles," 20th AIAA International Space Planes and Hypersonic Systems and Technologies Conference, Conference, Location, 2015. doi: 10.2514/6.2015-3553

[113] Gill, P. E., Murray, W., and Saunders, M. A. "SNOPT: An SQP Algorithm for Large-Scale Constrained Optimization," *SIAM review* Vol. 47, No. 1, 2005, pp. 99-131.